Towards Harmonious Co-existence: Linear and Nonlinear Techniques for Interference Management in RFICs

A Thesis Presented to

The Academic Faculty

By

Mohammad Omer

In Partial Fulfillment

of the Requirements for the Degree of

Doctor of Philosophy in Electrical and Computer Engineering

School of Electrical and Computer Engineering

Georgia Institute of Technology

May 2013

Towards Harmonious Co-existence: Linear and Nonlinear Techniques for Interference Management in RFICs

Approved by:

Dr. James S. Kenney, Advisor
School of ECE
Georgia Institute of Technology

Dr. Ian F. Akyildiz
School of ECE
Georgia Institute of Technology

Dr. Gregory D. Durgin
School of ECE
Georgia Institute of Technology

Dr. Bob Baxley
Georgia Tech Research Institute

Dr. David V. Anderson
School of ECE
Georgia Institute of Technology

Dr. Adeel Khalid
School of Mechanical and Systems Engineering
Southern Polytechnic State University

Date Approved: February 6, 2013

ACKNOWLEDGEMENTS

I want to thank my advisor Professor James Kenney for his support throughout the work conducted in this thesis. I would also like to thanks my committee members Professor Gregory Durgin and Professor David Anderson for reading through my research and making suggestions for the improvement of presentation.

My thanks also go to Professor Akyildiz, Dr. Bob Baxley, and Professor Adeel Khalid for agreeing to serve on my committee. Their time and effort in doing so is much appreciated.

Contents

LIST OF FIGURES

LIST OF TABLES

Chapter 1

INTRODUCTION

1.1 Introduction and motivation for research

Cellular technology has been pervading our lives for many years. It has slowly evolved from its inception to significant maturity with the introduction of 3G and 4G cellular phones. With the advent of cellular phones, has come increasing number of technological innovations to extract the most and the best out of ever decreasing spectrum. Radio transmission has developed into a very sophisticated art which has solved many of the emerging problems of spectrum famine. However, user requirements for the data are endless. Thus, the allocated spectral bands have shrunk smaller, and the spectral efficiency of transmission, namely bits/Hz, has grown larger. This trend is expected to continue well into the future. Modern cellular radios impose a wide array of requirements on the designers, and many of the problems lie at the intersection of communication theory, analog circuit design, digital signal processing and RF and microwave engineering.

This thesis is meant to address some of the emerging problems in new wireless standards. These problems have been caused, in part, by the modern transmission standards that have successively eroded the guard-band between different frequency multiplexing schemes. An increased signal bandwidth and high dynamic range of the communication pulses has also exacerbated these problems. Such high bandwidth and large dynamic range signals require increasingly linear components to prevent signal distortion. Some of these problems have slowed down the march towards a universal and

ubiquitous radio receiver. Such a receiver should be able to transmit and receive a broad range of modulation schemes over multiple data rates and different spectrum allocations.

1.2 Necessity for co-existence

The coexistence schemes that we will discuss in this thesis are necessitated by some major trends happening in the radio transceiver design. We will concentrate on the description of two trends that are at the forefront of these sweeping changes. One is the migration of radios to higher generations which increasingly rely on frequency division multiplexing, and the other is the opening of receive path bandwidth to enable software defined radios.

The previous generation of radios, mostly 2G, used half duplex operation by transmitting and receiving in timing bursts. This allowed the radio operation to be carried on using multiplexing switches as shown in Figure 1.1. Due to radios that continuously receive, manipulate and transmit data, such time sharing is no longer possible. 3G radio standards and onwards, provide for the full-duplex operation, whereby transmitter and receiver are both operating at the same time [1]. Most of the full duplex transceiver operations happen in the frequency multiplexing mode, where the transmitter and the receiver share the adjacent regions of the spectrum. This is a radical departure from the previous standards and necessitates some basic changes in the radio architecture. Such architecture is shown in Figure 1.2.

In the first place, the scheme of Figure 1.2 increases linearity requirements for the receiver front-end [2]. The receiver would now encounter large frequency content. It also imposes tight filtering specifications on the radio front-end. The receiver, which is typically operating at very low signal levels, now lies next to the high power transmitter.

This makes it vital for the duplexer filters to have very large attenuation in the stop-band, in order to prevent the spurious signals of the transmitter from interfering with the receiver [3].

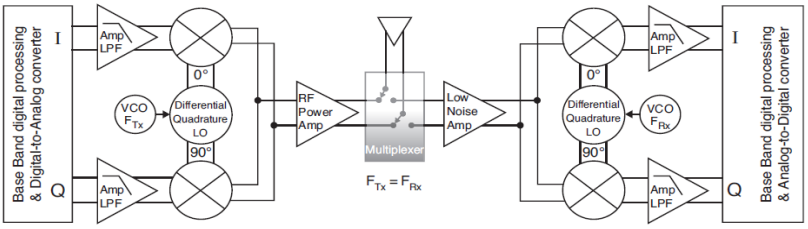

Figure 1.1: Block diagram of a TDD transciever

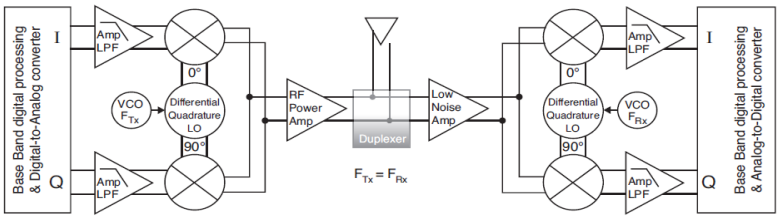

Figure 1.2 : Block diagaram of a FDD transciever

The scarcity of electromagnetic spectrum has necessitated that the frequency spacing between different bands be reduced. This shrinkage of buffer frequency space is accomplished by using even sharper frequency domain filters. Greater rejection and sharper roll-off in these filters is accomplished by the high-Q acoustic resonators [4]. Hence, the duplexer filters are bulkier and occupy much of the real estate in a radio board. The transceiver front-end can now be depicted as shown in Figure 1.3.

At the same time that the spectral spacing has shrunk, the bandwidth transmitted by radios has grown remarkably. The spectrum occupied by emerging radios is growing

wider [5]. The wide spectrum radiated by the SDRs makes it increasingly difficult to control the transmitter linearity and the out-of-band spectral expansion.

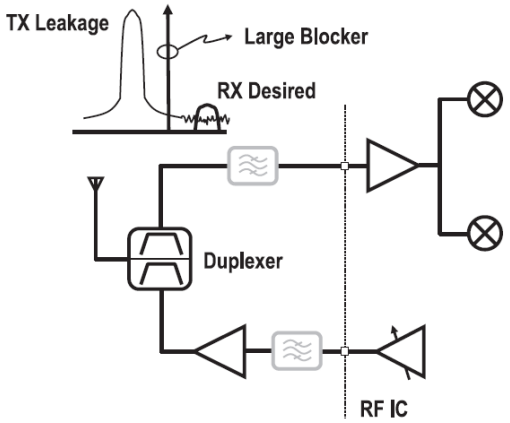

Figure 1.3 : RFIC front-end and the effect of duplexers

Therefore, while the frequency content of transmission has increased significantly, the band spacing between the channels is on the decline. The large frequency content results in a greater dynamic range of signal amplitude leading to increased nonlinear operation of the front-end. The reduced spacing between bands reduces the transition region of the filters. The front-end filters are now constrained to have a much larger pass-band along with much narrower transition region as well as much greater attenuation in the stop-band (to cater for the increased spurious emissions). These problems have prompted investigation into novel methods of receiver front-end filtering [6]. All these constraints lead to larger and heavier filters with greater delay and sharper phase responses. The sharp frequency filter at the radio front-end also constrains the radio operation in another way, which reduces the flexibility of the radio operation.

The paradigm of software defined radio has been in vogue for several years now [7]. A comprehensive survey of the state of the art and pointers to the future has been given in [8]. The envisaged software defined radio is a platform that is immensely more flexible and dynamic than today's radios. A diagram of such a radio is shown is Figure 1.4. It requires enabling by several components, most notably, the sampling device, the radio channel extraction and the signal reconstruction algorithms. But the most important requirement for these modern radios, is the need to sample as much bandwidth as possible, which could be selected and processed later in the signal processing chain. What prevents a significantly huge bandwidth from being sampled is the front-end filtering. The front end filtering however eases the linearity requirements for all components down the chain.

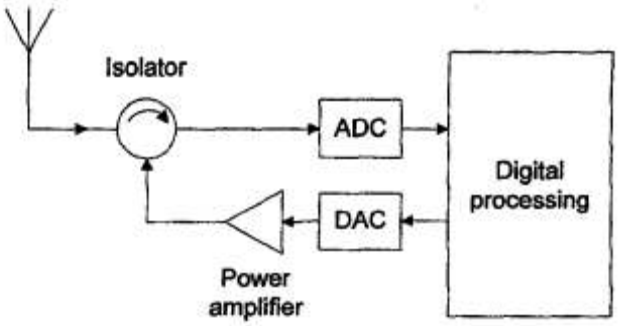

Figure 1.4 : Mitola's vision of a software defined radio

Modern transmission standards are characterized by their very wide bandwidths. Linear operation and higher bandwidth are conflicting requirements. A higher signal bandwidth has a high peak to average power ratio. This signal type increases the linearity requirement of the signal path. If sufficiently linear path is not provided, the signal will undergo spectral expansion which will distort the in-band signal and lower the signal to interference ratio for the receiver [9]. Efforts have long been made to reduce the PAPR of

the wideband signals with some success [10]. However, the problem is expanding in scope as more bandwidth is procured for transmission standards and greater efficiency is demanded of RF power amplifiers.

In order for the radio to be flexible, we want to perform most of the filtering in the digital domain. The receiver should be able to take a large chunk of bandwidth and achieve the required selectivity by digital filtering [11]. The digital channel filtering allows the radio front end to be flexible while affording the possibility of receiving multiple radio bands over different standards. The most drastic frequency domain filtering happens through the duplexer which has to attenuate a high powered adjacent transmitter signal [12]. If the duplexer attenuation requirements are relaxed, more of the filtering can be relegated to digital signal processing.

Sampling at RF frequency (large sampling rate to bandwidth ratio), will also require an extremely linear signal path. This requirement has to be satisfied or else the spectral components will become distorted and overlapping. A solution to an extremely linear receive path must be found to enable this radio flexibility.

1.3 Radio co-existence

The future computing platforms will be studded with multiple radios. A typical radio platform might contain a WiFi, WiMax, 3G, 4G, Blutooth or other legacy radios. An example of such a receiver is shown in Figure 1.5. As the number of radios per platform continues to increase, there would be a lot of spurious emission in the adjacent bands by the transmitters. The adjacent channel power ratio specifications have been developed for non co-located radios and would need to be tightened further. Similarly many blockers will fall into the receive band because of inter-modulation effects in the

receiver front-ends. At the receiver end, this implies a lower signal to interference ratio. This lowered signal to noise ratio will affect nearly all the radios on the platform, but it can be particularly disastrous for broad-band and low transmission power radios as they can be completely swamped by the emission levels. These scenarios can place huge constraints on the receiver design [13].

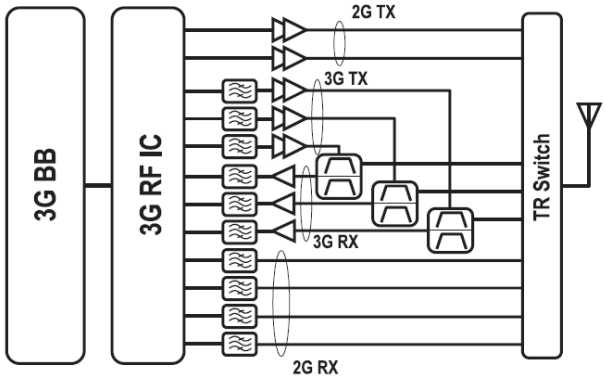

Figure 1.5 : A front-end of a typical modern receiver

The interference to radios present in a single platform can stem from multiple scenarios. But we can identify two basic phenomena which will be behind any possible scenario of interference. These phenomena could act independently, or in concurrence with each other. The first is the transmitter nonlinearity, whereby a nonlinear signal path in the transmitter leads to out of band spectral components causing interference. The second is the receive path nonlinearity, where apparently innocuous blocker channels, separated from the desired receive channel can experience receiver nonlinearity and create in-band interference components due to cross-modulation [14].

A peaceful coexistence of radios can be enabled by attention to the details of transmitter and receiver specifications and casting a look at the specifications of all the radios operating in the vicinity. This along with a tighter control on transmitter and

receiver linearity specifications will enable two things. For one, it will reduce the spurious emission from the transmitter [15], as well as reduce receive intermodulation distortion. In this way, different radios will be able to operate on a single platform without undergoing a substantial hit in the signal to interference ratios.

1.4 Organization of the thesis

In this thesis we will begin by looking at the fundamental tools required to address the co-existence issues facing modern receivers. This discussion in chapter two will consider the case of pre-distortion systems and use their example to highlight the techniques of nonlinear modeling and nonlinear system identification. These techniques will become the underlying thread for the rest of material introduced in the thesis.

Chapter 3 on Tx/Rx co-existence introduces the coexistence technique developed by the author to aid the joint transmitter/ receiver operation in the full duplex mode, without resorting to bulky and expensive duplexers. It is achieved by cancelling the transmitter interference which finds its way into the receiver through inadequate attenuation provided by the duplexer filters. The development of this technique borrows ideas from nonlinear sytems theory, multi-rate signal processing and adaptive filters to come up with a robust solution to Tx/Rx co-existence problem. The proposed solution is implemented on a prototyping platforms and measurements are conducted in the lab. The measurements validate the simulations results and demonstrate the effectiveness of the presented techniques.

Chapter 4 changes gears and delves into one of the pressing problems facing the joint operation of receivers in an integrated radio platform. The problem is caused by the presence of different synthesizers which have the potential to couple with one another

and cause unwanted interference to find its way into the receivers. This can be a disastrous situation for co-existence. A solution proposed by the author is shown to mitigate this effect, and simulation studies are conducted as part of its validation. Equipped with simulation studies, an actual test-bench is setup using commercial grade RFIC chipsets. The radio settings on these chipsets are designed to replicate the receiver co-existence problem. RF measurements are conducted and a prototype digital system is setup to process the measurements. The measurements show that the proposed technique can be validated in a real RF environment on commercial grade RF chipsets.

Chapter 5 looks at one of the most pressing issue facing radios of today. The problem of receive-band noise which plagues many radios, and causes problems in the design of better, more capable receivers of the next generation. The receive band noise problem has been the topic of discussion in several recent journals. The author proposes a digital solution to the problem which has proved effective in combating this issue. If the receive band noise can be successfully cancelled, the co-existence of transmitter, receivers, and all the sophisticated carrier aggregation techniques proposed by modern standards can become a reality. The solution proposed for receive band noise is prototyped on an RFIC platform, and tested and measured for its effectiveness in combating the problem. We were able to show that with some hardware overhead, addressing of receiver band noise is a possibility in future RF chipsets.

Lastly Chapter 6 introduces us to the challenges facing modern, highly efficient transmitters. These transmitters are able to produce spectral emission at far off harmonic frequencies. Such emission can be extremely disruptive to co-existence scenarios. We extend the nonlinear kernel theory to provide estimators for predicting the interference

caused by such transmitters and subsequently cancelling them. A lab prototype of an envelope tracking transmitter is built and then used in generating and measuring the interference caused by such transmitter. We demonstrate successful interference cancellation performance on this platform to validate our nonlinear kernels and adaptive system identification for such transmitters.

We conclude the thesis by saying a few words on the evolution of radios into the future. The previous generation of radio engineers and designers have been spurred by the quality of communications, the scarcity of spectrum, and the optimization of data rate as of late. The next generation of radio development will be spurred by the interference problems facing modern radios. The work presented in this thesis, has great room for further expansion and experimentation. Some of the pointers to future work are presented in this chapter.

Chapter 2

Conventional RF Coexistence Methods and Tools

In this chapter we began to look at some of the earlier work in co-existence. Most of the earlier work on co-existence has relied heavily on linearization of radio transmitter. The authors work has shifted the focus of the co-existence methods to include receivers as enablers of RF coexistence as well. We detail out those ideas in Chapter 3. But for the present we look at work in transmitter linearization, which will familiarize us with the tools of radio coexistence and lay groundwork to understand later chapters in the thesis.

2.1 Radio front ends and nonlinear distortion

Fundamentally, the radio front end is a nonlinear system. It has amplifiers, mixers and narrowband filters. The filter induces the least nonlinearity whereas something like a power amplifier is the most nonlinear [16]. In a very simple scenario, a nonlinear device can be modeled with a Taylors series. If the devices employed are differential, such nonlinearities can be reduced to odd order nonlinearities. Odd order non-linearities result in in-band distortion as well as adjacent channel power leakage [17] which results in the violation of spectral masks imposed by a particular transmission standard. The spectral expansion of transmit signal due to PA circuit is shown is Figure 2.1. The figure shows the response of the PA to different narrow and broadband signals. We see that the PA affects these signals by creating additional spectral components. Nonlinear systems do not obey the ‘frequency content preserving’ property exhibited by all linear systems.

In addressing concerns about the radio frontend nonlinearity, one fundamentally encounters the notion of nonlinear modeling and compensation [18]. If the nonlinear

radio front end can be modeled, we can design a compensator (read equalizer) to mitigate the effect of such nonlinearity. This is the fundamental idea behind digital pre-distortion.

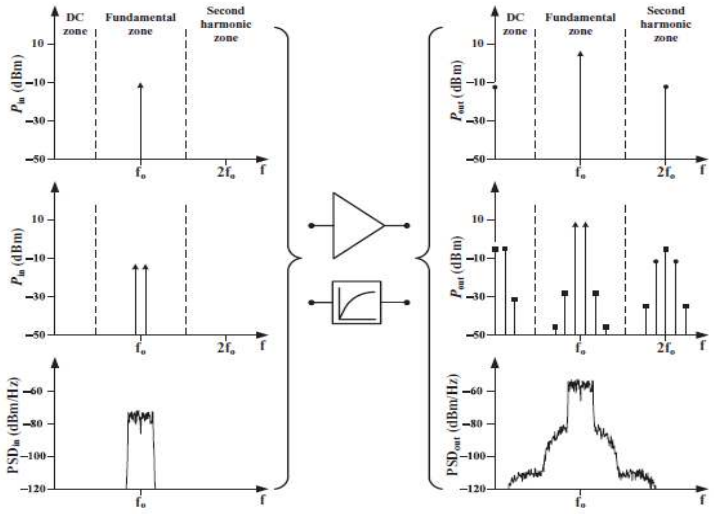

Figure 2.1 Impact of operating PA on spectral expansion

Nonlinear modeling can also predict the signal coming out of a radio frontend or getting inadvertently injected into the receiver. Such modeling can then be used to enable radio coexistence. This modeling also has to be adaptive in order for the system to adapt to the changing nonlinear response of the radio components. The radio components drift in their characteristics due to temperature and bandwidth fluctuations [19]. We will discuss architectures based on nonlinear modeling which make use of these techniques to make radio co-existence possible.

2.2 Modeling nonlinear components

Radio power amplifiers are the dominant cause of nonlinearity in radio front-ends. Unlike mixers, power amplifiers are designed as linear components, but the high swing outputs of these amplifiers necessarily involve nonlinear behavior [20]. The nonlinear operation of the amplifier also improves its efficiency [21]. Therefore, one of the potent

reasons for allowing nonlinear, near saturating behavior in power amplifiers is to get significant gains in efficiency. The nonlinear behavior however needs to be controlled and compensated in order to satisfy the emission requirements. Since power amplifiers are so crucial to determining the overall linearity of the system, huge amount of effort has gone into explaining their nonlinear behavior [22].

There has been large number of attempts to explain and characterize the power amplifiers by building models of the nonlinearity. Some of the earliest models have taken after the fitting or regression approach, coming up with the simplest functions that can explain the input output characteristics. Famous examples of these are the tangent hyperbolic nonlinearity, the Salehi model, the Ghorbani model and the Rapp amplifier model [23] [24] [25]. The distorting characteristics of the Salehi model are shown in Figure 2.2.

Generally the nonlinear distorting characteristics are broken into amplitude/amplitude (called AM/AM) and amplitude/phase (called AM/PM) parts.We now go into the details of inverse nonlinear modeling, and show how it can be used to advantage in linearizing the transmitter.

2.3 Pre-distortion for transmitter linearization:

The basic idea of predistortion system is to use an inverse nonlinearity in cascade with a power amplifier nonlinearity to yield an overall linear system. The idea is shown in Figure 2.2.

The first curve of relevance is the dot-dash one, called ‘Power gain curve’. This curve refers to the amplitude characteristics of an uncompensated power amplifier. The slope of this curve is the power gain of the amplifier in dBs. A curve used to compensate

the nonlinear distortion is shown as the 'Inverse curve' in the figure (dotted line). When the two systems are operated in cascade the resulting overall curve is shown as a solid line in the figure referred to as 'Linearized gain curve'. As we observe that with this particular inverse curve, the gain of the amplifier has been lowered. The regions A and B within the inverse curve represent regions of high and low linearity respectively. In region A the power amplifier was significantly linear, whereas in region B it was very compressed before reaching its maximum power at Pout.

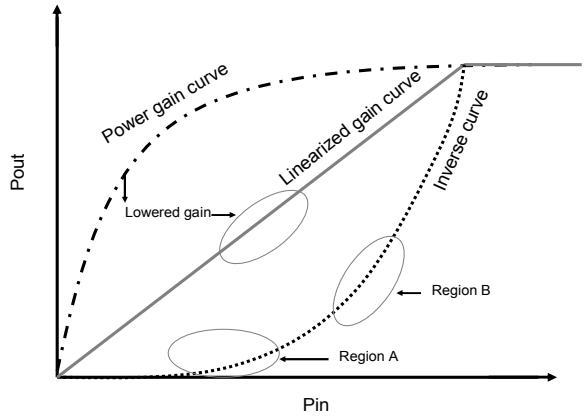

Figure 2.2 Relevant curves for showing the predistortion effect

2.3.1 LUT based predistortion

A nonlinear system can be cascaded with another nonlinear system to linearize the characteristics of the cascade. Before showing how to derive the characteristics of the system, lets look at the arrangement of blocks used to accomplish this end. The architecture of a simple LUT based predistorter is shown in Figure 2.3. In conventional lookup table based pre-distorters, the objective is to obtain a predistortion function $f(.)$ which when cascaded with a power amplifier transfer function $g(.)$ results in a linear transfer function.

In the equivalent model for predistortion shown in the figure, signal *s* is the raw input from the baseband transmitter. A baseband model of PA can be given by

$$y = g(|x|).e^{j(\angle x)} = g_r(|x|).e^{j(\angle x + g_\phi(|x|))} \tag{2.1}$$

where the amplifier gain characteristics have been decomposed into an AM/AM component represent by the subscript *r* and an AM/PM component represent by the subscript ϕ appended to the composite gain characteristic of *g*.

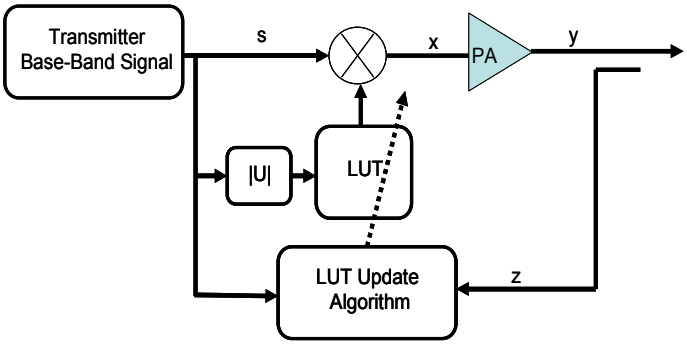

Figure 2.3 LUT based predistortion model

Let $f_r(.)$ and $f_\phi(.)$ signify the operator function of the predistorter on input amplitude and phase respectively. The objective of predistorter is to linearize the amplifier up to a certain maximum amplitude of s_{max}.

$$y = \begin{cases} c.s & for \quad |s| \le |s|_{\max} \\ s_{\max} & for \quad |s| \ge |s|_{\max} \end{cases} \tag{2.2}$$

where *c* is of the form $c = c_r e^{jc_\varphi}$ which breaks the desired gain into amplitude and phase components. The overall objective of the pre-distorter is achieved if the following relations are fulfilled.

$$f_\varphi(|s|) + g_\varphi(|x|) = c_\varphi \tag{2.3}$$

$$g_r(|s|.h_r) = c_r.|s| \tag{2.4}$$

where h_r represents the envelope component of the LUT output with which the incoming data is being multiplied. The form of the predistorter function can be given by

$$f_\varphi(|s|) = c_\varphi - \hat{g}_\varphi(|x|) \tag{2.5}$$

where

$$|x| = |s|.h_r \tag{2.6}$$

and

$$f_r(|s|) = \frac{\hat{g}_r^{-1}(c_r.|s|)}{|s|} \tag{2.7}$$

where $\hat{g}_r^{-1}$ is the estimated inverse function of the power amplifier.

Predistortion function *f(.)* is organized as a set of discrete predistortion coefficients for the entire signal dynamic range. The granularity of this function limits the amount of adjacent channel reduction that can be achieved. In this work we will not concern ourselves with the optimal quantization for such a function but will assume a usage of 128 amplitude bins which is a good compromise between performance and complexity. Let *F* then signify the table with a discrete set of entries, each corresponding to a unique input amplitude. The adaptation of *F* can then be accomplished with either a linear or secant update method of the form,

$$F_i(k+1) = F_i(k) + \alpha \frac{z - s}{z.F_i(k)} \tag{2.8}$$

where $F_i(k)$ denotes the i^{th} entry of table at k^{th} iteration and α is the adaptations factor.

2.3.2 A Polynomial predistortion architecture:

It is pertinent here to discuss the polynomial pre-distortion architecture, because it allows us insight into nonlinear modeling with polynomials, which will play a critical role in co-existence architecture to be discussed in later chapters.

The polynomial predistortion is based on the so-called indirect learning architecture, whereby the adaptive system converges automatically to a post inverse which can be used as a pre-inverse too. Figure 2.4 shows the diagram of an indirect learning based predistortion system.

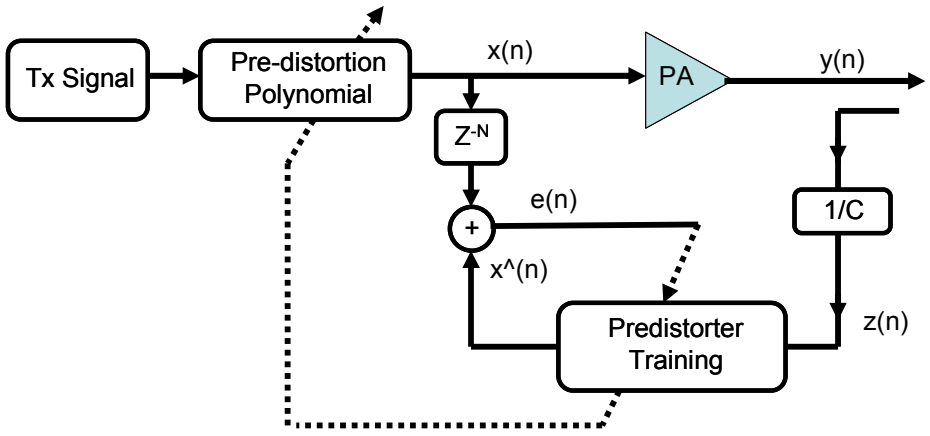

Figure 2.4 Predistortion method using polynomials and direct learning

The signal tapped from the output of the power amplifier undergoes normalization with the desired gain *C* and is fed to the predistorter training block. The training can be accomplished through the LMS based training algorithm for both the real and imaginary parts of the predistorting polynomial. Polynomial predistortion problem can again be written in terms of an inverse function *f(|z|)* which consists of an envelope and phase function to be estimated. Let *z* be the signal input to the predistorter training block with a

magnitude $r(t)$ and a phase $\varphi(t)$. Then the two components of the predistorter can be expressed as 2.9 and 2.10.

$$f_r(r) = f_{1r}r + f_{2r}r^2 + ...f_{Lr}r^L = VR_{fr}^T \tag{2.9}$$

$$f_\varphi(r) = f_{1\varphi}\varphi(t) + f_{2\varphi}r(t)^2 + ...f_{L\varphi}r(t)^{M-1} = PR_{f\varphi}^T \tag{2.10}$$

where different row vectors in the above equations are defined as,

$$R_{fr} = [r(t) \quad r(t)^2 \quad ... \quad r(t)^M] \qquad R_{f\varphi} = [\varphi(t) \quad r(t) \quad ... \quad r(t)^M]$$

$$V = [f_{1r} \quad f_{2r} \quad ... \quad f_{Lr}] \qquad P = [f_{1\phi} \quad f_{2\phi} \quad ... \quad f_{M\phi}]$$

Letting G be the operator function of amplifier on input,

$$Y = G[f_r(|x|).e^{j(\angle x + f_\varphi(|x|))}] \tag{2.11}$$

The objective function of our problem can now be formulated in terms of the input x of the amplifier and can be written as

$$J_1(V,P) = E\left(xC - (V^T R_{fr}.\exp(j.P^T R_{f\varphi}))\right)^2 \tag{2.12}$$

where C is the desired closed loop gain of the amplifier to normalize the estimator input. The input *x(n)* to the amplifier is compared against the estimate of the input formed by the predistorter training function. The error function can be used to provide the update of the polynomial function in an LMS manner, and the update equation can be described in the general form as ,

$$[V_{k+1}P_{k+1}] = [V_{k+1}P_{k+1}] - \mu_k \nabla_V J_1(V_k, P_k) \tag{2.13}$$

In most practical cases where the full gradient information is not available to the solver, we can make use of an approximation by writing,

$$V_{k+1} = V_k - \mu_k R_{fr,k} e_{v,k}, \; P_{k+1} = P_k - \mu_k R_{f\phi,k} e_{p,k} \tag{2.14}$$

The polynomial weights will converge to make it a post inverse to the amplifier nonlinearity, and this post-inverse can then be substituted in place of a pre-inverse to perform polynomial predistortion.

2.4 Design of a predistortion system

In order to demonstrate predistortion and learn about some of its shortcomings, a lookup table based predistorter was built using Matlab and Simulink. The granularity of the lookup table entries was set to 256, which is a reasonable compromise between performance and complexity. A 16 QAM signal with a double sided bandwidth of 5 MHz was originally used which was finally upgraded to a high PAPR OFDM signal using 64 sub-carriers. The PA model used is a simple polynomial model of the form given by (2.15) and (2.16).

$$|y(k)| = \begin{cases} |y(k)| - \dfrac{|y(k)|^3}{3} - \dfrac{|y(k)|^5}{5} & |y(k)| < y_{\max} \\ y_{\max} & |y(k)| \geq y_{\max} \end{cases} \qquad (2.15)$$

$$\angle y(k) = \begin{cases} k_{rad/v} \angle y(k) & |y(k)| < y_{\max} \\ \phi_{\max} & |y(k)| \geq y_{\max} \end{cases} \qquad (2.16)$$

The predistorter uses a simple training algorithm of eq 2.8. The result of running the predistorter for several thousand iterations of the training algorithm are shown in Figure 2.5. The spectrum of the different signals in Figure 2.5, show the linearization action of the predistorter in clear detail. The input signal shown in black is the multicarrier OFDM signal at the input of the system. The signal after passing through the nonlinear power amplifier appears in grey. This shows the spectral expansion caused by the nonlinearity. Once the signal is predistorted using the predistortion algorithm, the result appears in the dashed-grey trace. The spectral expansion of the signal has been curtailed in the adjacent

channel regions. This amount of reduction achievable with a certain predistorter is a function of the granularity of its table, which determines the accuracy of inverse characteristics that can be modeled.

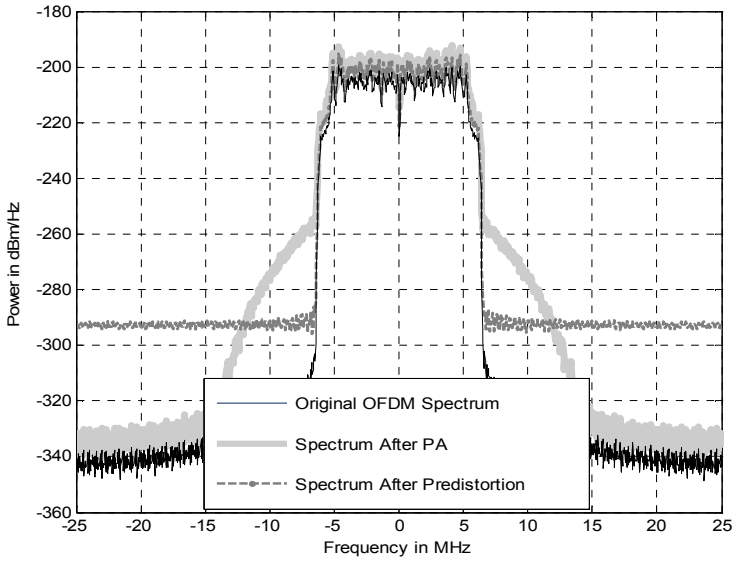

Figure 2.5 Linearization action of an LUT predistorter

There are however certain problems faced by LUT predistorters which can hamper their utilization in real-time systems. Some of these problems are illustrated in the next section.

2.4.1 Design constraints with predistortion systems

An LUT and polynomial based predistorters were discussed in the preceding sections. The major problem confronting these topologies is the use of signals with high PAPR. When used with such signals, these predistorters exhibit a very slow rate of convergence. In order to look at this effect in a closer detail, a predistorter was used from the previous section, and the perfect predistortion characteristics were apriori calculated. The converging predistorter and the ideal predistorter are superimposed on each other and the result appears in Figure 2.6. Figure 2.6 assumes that all the table entries started from

an initial value of 0.65. The figure shows the first 150 entries of the look up table. We observe that the entries in the lower amplitude regions (from 0 index to 50 index) have predominantly converged. This is symbolized by the disappearance of markers from the initial 0.65 mark. However the table entries in the high amplitude regions (index 70 and onwards) are still struggling to converge. Due to the non-convergence of these entries, the system is taking a hit in its linearization characteristics.

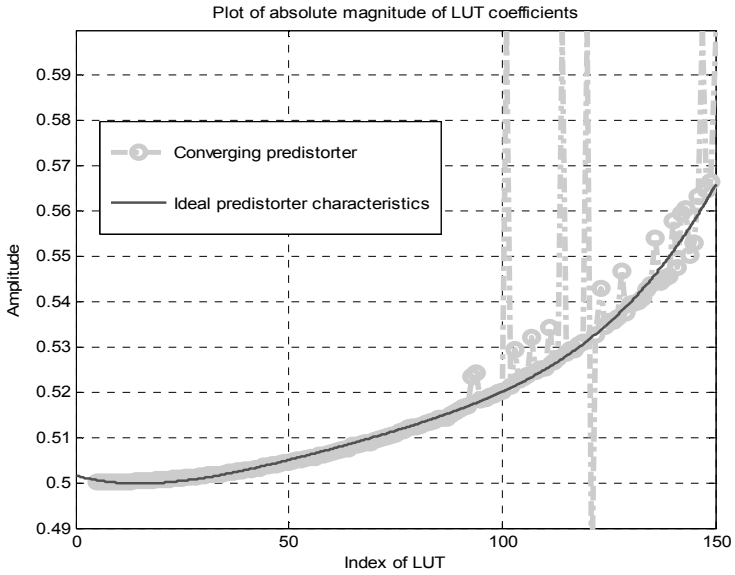

Figure 2.6 Converging vs ideal predistorter characteristics

The higher amplitude entries converge slower because of the high PAPR of the input signal, due to which the higher amplitude bins are infrequently encountered. In order to circumvent this problem of slow convergence the author proposed a modified predistortion architecture.

2.4.2 An improved predistortion architecture

The proposed pre-distorter architecture is designed to take care of the signal peculiarities described in the previous section and converge fast while working with signals of high PAPR characteristic. The architecture is based on one key observation

over the training dynamics of predistorters excited with multi-carrier signals. The observation of the training process suggests that several amplitude bins in the higher amplitude regions, do actually show convergence to optimal estimate, even with the infrequent peaks encountered. In other high amplitudes in the signal, though infrequent, are encountered in the same amplitude bins and lead to the convergence of respective coefficients. These coefficients can then be used to aid in deducing the overall form of the predistorter characteristic and hence account for the un-converged coefficient of the LUT. This leads to great improvement in the quality of predistortion. The new predistortion system, shown in Figure 2.7 consists of two fundamental loops.

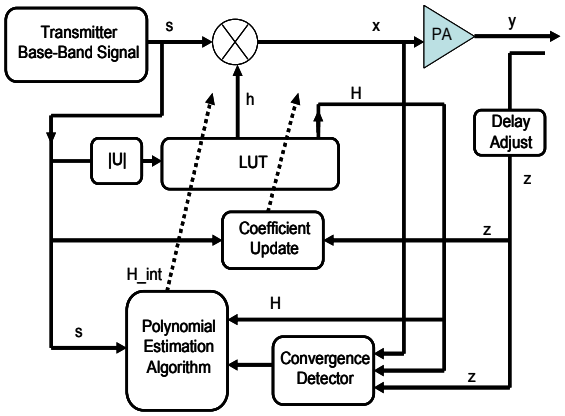

Figure 2.7 : Improved predistortion system

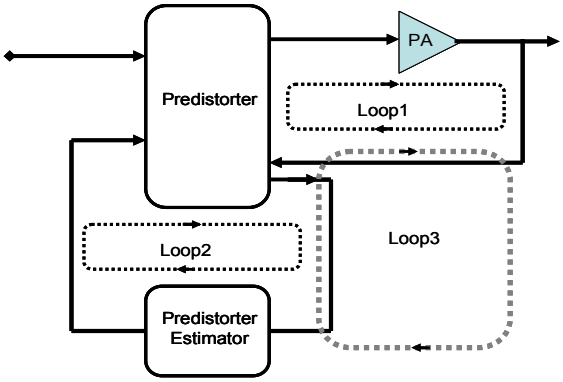

Figure 2.8 : Main loops within the new system

Loop 1 which spans signals *s, x, y, z* along with complex coefficients *h* forms the conventional predistortion loop. Loop 2 is formed between complex coefficients *h,* the coefficient vector *H* and another vector *H_int* which together form the predistorter estimation loop.

The overall operation of the system can then be broken down into three loops as shown in Figure 2.8. In the beginning, update of LUT entries consists of Loop 1 which adapts the coefficients initially to yield the vector *H*. This can be referred to as *partial fine estimation*. In the next phase Loop 2 takes the partially converged table as its input and after performing polynomial estimation, outputs its own estimate of the complete predistorter characteristic given by *H_int.* This would be referred to as *full coarse estimation*. The system then again reverts to slow update of Loop I which would finally yield a fully converged fine estimation of the predistorter characteristic. The effect of running the predistortion system in the manner discussed above is shown in Figure 2.9.

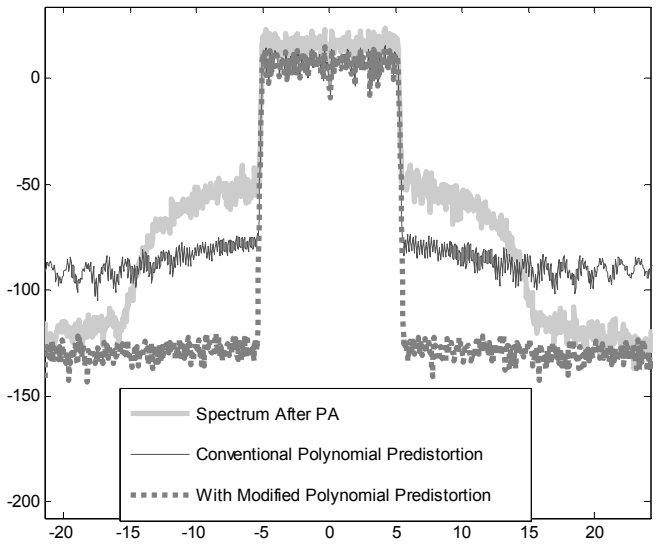

Figure 2.9 Modified predistortion system results

After processing 2000 samples of the transmitter waveform, we have the spectra shown in the figure. We observe that the conventional predistorter has not yet converged fully as demonstrated by the solid grey (2^{nd} trace) which is still far from the ideal signal spectrum. The dotted grey trace representing the modified predistortion system has

converged to its optimal value and shows a significant reduction of the adjacent channel spurious frequency components.

After running Loop 2 once, both the loops then revert to a periodic flipping between them. The initial update through Loop 1, the triggering of Loop 2 on partial convergence, switching to Loop 1 again, and subsequent periodic flipping of them in the steady state, are all the control tasks which are managed by Loop 3. The final interchange between Loop 1 and 2 in the steady state is a function of amplifier variability and susceptibility to environment and aging.

2.4.3 Predistortion system components and caveats

The above discussion has demonstrated that predistortion is a viable scheme for enabling coexistence. The primary effect of adding predistortion to a system is that of reducing the out-of-band spectral emission. The absence of out-of-band emissions allow transceivers operating in the neighborhood bands to co-exist without any interference problems. To comment on some of the system level requirements we show a more detailed diagram of the transmitter employing predistortion in Figure 2.10

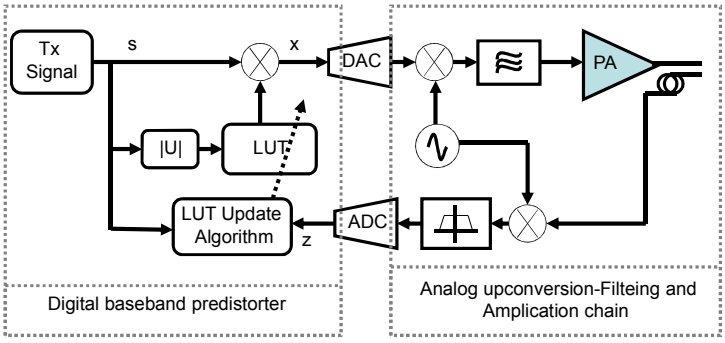

Figure 2.9 Passband or carrier frequency based model of predistorter

The system of Figure 2.10 includes up-conversion, down-conversion, A-D, D-A and other associated filtering operations. The difference between this and earlier diagrams of predistortion systems were that al the earlier ones were equivalent base-band representation of the predistortion system, while this represents the complete pass-band system.

In the system shown in the pass-band predistorter, we observe that the signal x which comes out of the digital base-band predistorter has experienced a nonlinearity contained and applied by the lookup table. This passage through the nonlinear system expands the signal bandwidth. The Digital to Analog Converter (DAC) shown in the figure has to be clocked in order to pass this excess bandwidth. Opening the bandwidth of the system leads to a lot of spurious noise from the clocks. This can have far reaching consequences for the system performance. We will have more to say about the consequences of this effect in the next chapters. For the moments, the purpose was to emphasize that predistortion leads to expansion in signal bandwidth, which leads to the rate increase in DAC/ADC clocks and the overall bandwidth of the front-end chain.

2.5 Conclusion

The purpose in this chapter was to focus on a conventional co-existence technique which familiarizes us with the need and utility of coexistence and how it can be helpful for the radios which do not want to interfere with their neighbors. The predistortion technique also adequately highlights the role of nonlinear modeling and system identification for the purpose of co-existence. As we move forward, we will look at different coexistence techniques that the authors have developed for different scenarios, and also compare them to predistortion in some instances.

The chapter has given some of the most common types of predistorters used in real systems. There are other, not so common types of predistortion, which include purely analog predistortion. There are also other linearization methods besides predistortion which can be used to enhance the linearity of the transmitter. The treatment in this chapter is not meant to be exhaustive, but to illustrate a technique that is fundamental to our discussion in later chapters and is successfully used in real commercial transceiver systems.

The next chapter will detail out the common scenario of Tx/Rx co-existence, and how the problem can be tackled by using linear and nonlinear system identification methods.

Chapter 3

Tx / Rx Coexistence for Modern Transceivers

Advances in radio technology have led to increased integration in radio transceiver chipsets. In modern chipsets there are as many as 5-7 radio standards operating and residing on the same chip. With ever shrinking device geometries and scaling of the supply voltages, the radio front-ends are forced to operate nonlinearly. Nonlinearity leads to spurious emission by front-ends which can cause disastrous effects for the receivers if left un-attended. The normal solution is to either employ pre-distortion, and/or to alleviate it using very sharp (high insertion loss) duplexer filters. The duplexers have increased in count with the emergence of these modern radios and are very resistant to integration and scaling. This chapter looks at the problem of out-of-band emission from a different perspective, by proposing to model and cancel the front-end nonlinearity using the very own receiver of the radio. This can have potentially radical consequences for radio integration, low power operation, size/cost reduction of duplexers, and overall harmonization of radio environment. Although we look at the case of a single transceiver, the coexistence of different standards can be enabled by a very straight forward application of these ideas.

3.1 Modern radio front-ends

The radios of tomorrow face increasingly big challenges. These result from technology scaling at the RF circuit level and increasing complexity of modulation at the digital baseband level [26][27]. The scaling reduces the linearity of the devices by allowing for lower IIP3's and OIP 3's (approaching ~28-30 dBm @ output power of ~32

dBm), while the modulation schemes increase the PAPR of signals (6-8 dB for LTE and forthcoming 3G/4G standards [28]) thus increasing the dynamic range and pushing the components higher into saturation [29][30]. The compounding of these factors [31] along with stricter limits on out-of-band emission (approaching -10 dBm @ 3 MHz offset from fc), drives up the size and cost of duplexers [32]. The duplexer filters are used to attenuate any out-of-band spectral components through a brute force imposition of a sharp frequency roll-off having attenuation in the range of 50-60 dB for the stop band frequency components [33]. The duplexers have shown extreme reluctance to integration, and are still off the chip components [34]. Duplexers appear in increasing numbers in a radio system because of all the different bands a radio must be able to operate in [35]. This necessarily increases the BoM and incurs cost and size penalty in transceivers.

3.2 Enabling Tx/Rx coexistence

This chapter looks at the transceiver architectures which can enable the coexistence of these highly nonlinear RF front-ends without resorting to extensive filtering approaches. This has two important consequences. One is that it necessarily relaxes the duplexer specifications which allows for low-cost, smaller form factor and can allow integrated duplexers in the receiver [36]. But more importantly, the relaxation of duplexer is also a significant step towards removing the band-limitedness of the receiver [37]. This can finally realize the vision of a universal radio, where all bandwidth selection happens down the receiver in the digital domain. By allowing the selection of bandwidth in the digital domain, arbitrary tunability (over GSM/WCDMA/LTE bands) and receiver agility can be achieved. We begin by looking at the problem of spurious emission in FDMA transceivers and the consequences it can have for the received signal.

Figure 3.1 shows the architecture of a typical direct conversion radio, where a high power transmitter is operating in the vicinity of a receiver.

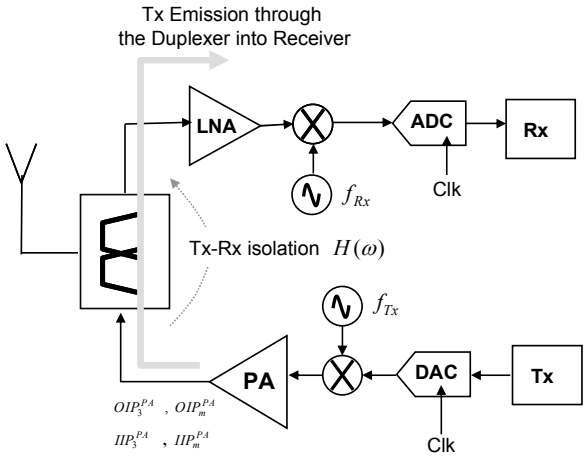

Figure 3.1 : A nonlinear transmitter affecting the receive path

The PA has finite OIP_3 and IIP_3 which lead to spurious emission that can affect the receiver if not properly attenuated by the duplexer. This asks for a highly selective, large area, large insertion loss components to attenuate the spurious frequency components.

There has been previous work to relax/eliminate duplexers in specific scenarios [38][39]. One satisfies a particular notch filtering [38] requirement and the other is geared towards the receiver [39]. None of the previous work has tried to use digital techniques to accomplish this end [41-44]. A work that comes very close in scope to the current work is that of [40] but is restricted to linear identification of front-end. In this chapter we propose a transceiver architecture that can address these challenges by using nonlinear modeling and system identification. Various configurations of this idea are explored to reduce the final chip area and power consumption for this scheme. Optimal transceiver structures are derived based on these criteria. We also lay down the mathematical

foundation for exploring this design space and come up with relevant algorithms and performance criterion. Different criteria for system performance are described and simulated. Section 3.3 begins by describing the problem of OOB (Out Of Band) emission in greater detail and deriving expressions for quantifying the emission components. Section 3.4 proposes a novel architecture to combat OOB emission and derives the mathematical expressions for designing the cancellation system. Section 3.5 proposes a reduced complexity architecture which leads to a generalized estimation and cancellation framework in Section 3.6. Measurement and simulation results are given in 3.7 which is followed by conclusion.

3.3 OOB emission problem and solutions

The problem of Tx OOB emission is shown in Figure 3.2. A transmit signal centered around the transmit frequency f_{Tx} has spurious emission surrounding it. These spurious emission components are caused by 3rd, 5th and 7th order nonlinearities in the front-end.

In FDD systems, the receive frequency is separated from the transmitter by several tens of megahertz. The receiver frequency is shown by f_{Rx} on the frequency axis. There are two noise floors shown to put the received signal *SNR* in context. The first is the system *AWGN* noise floor, which necessarily limits the received signal *SNR*. The second is the PA induced noise floor which is originally quite high but suffers significant attenuation after the duplexer.

We are interested in output emission of the amplifier at the frequency spacing of $f_{Rx} - f_{Tx}$ MHz away from f_{Tx}. We now detail a procedure to find emission component in this scenario. A general expression for PA output power is given by

$$P_o = \sum_{m=1}^{n} P_m = \sum_{m=1}^{n} g_m P_i^m \tag{3.1}$$

where P_i and P_o are the input and output power respectively, and P_m is the power in the m^{th} order product and $g_m (m = 1, 2, ..., n)$ is the power gain when $m = 1$ and nonlinear gain coefficients when $m \neq 1$.

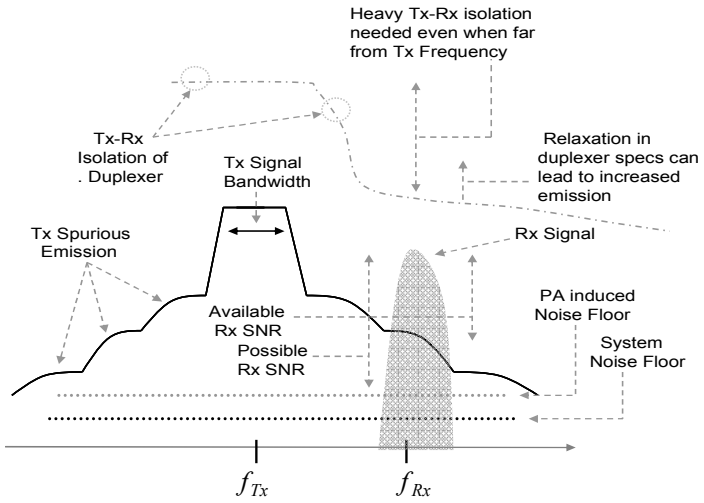

Figure 3.2 : Transmitter Interference and Duplexer Response

The two important cases of fundamental output and harmonic output can therefore be represented by

$$P_1 = g_1 P_i \quad , \quad P_m = g_m P_i^m \tag{3.2}$$

Converting these to dB scale yields

$$S_1 = G_1 + S_i \quad , \quad S_m = G_m + mS_i \tag{3.3}$$

Generally the power amplifier is characterized by measuring its OIP_m or IIP_m. OIP_m is defined as the point of intersection for the fundamental and harmonic components. For the m^{th} order inter-modulation product this can be written as

$$\begin{aligned} OIP_m &= G_1 + IIP_m \\ OIP_m &= G_m + mIIP \end{aligned} \tag{3.4-5}$$

Equating the two gives us the equation

$$(m-1)(IIP_m - S_i) = S_i - IMD_m \tag{3.6}$$

which can be manipulated to find the IMD power for any order of nonlinearity m. For the particular scenario of Tx self-jamming we define m, to be the floor of the ratio of Tx-Rx spacing to the signal bandwidth, i-e

$$m = 2 \times floor[\frac{f_{Rx} - f_{Tx}}{BW}] + 1 \tag{3.7}$$

We will look more closely at the derivation of expression in Section 3.3. Given m we can computer the total IMD signal power falling in the Rx band, by integrating the signal power due to IMD_n and IMD_{n+1} as the frequency spacing $f_{Tx} - f_{Rx}$ may not always be an integer multiple of bandwidth. The first IMD will extend from $f_{Rx} - \frac{BW}{2}$ to $f_{Tx} + nBW$, while the second IMD will extend from $f_{Tx} + nBW$ to $f_{Rx} + \frac{BW}{2}$. The total IMD power can therefore be written as a summation of these two powers.

$$\begin{aligned} S_{Interference} = &(f_{Tx} + nBW + \frac{BW}{2} - f_{Rx})(mS_i - (m-1)IIP_m) + \\ &(f_{Rx} - nBW + \frac{BW}{2} - f_{Tx})((m+1)S_i - mIIP_{m+1}) \end{aligned} \tag{3.8}$$

Theoretically the received signal should have the SNR given by the ratio of received signal power to noise power, $\frac{S_{Rx}}{S_{noise}}$ but the spurious residual emission from Tx signal acts as an interference which degrades the *Rx SNR* to $\frac{P_{Rx}}{P_{noie} + (P_{\text{int}erfernce} \square 10^{-\frac{ISO_{Tx-Rx}}{20}})}$, where ISO_{Tx-Rx} is the loss experienced by the IMD components due to the duplexer. The reduced receiver SNR is shown by '*Available Rx SNR*' in Figure 3.1. This is sometimes also referred to as de-sensitization of Rx or Tx self-jamming.

3.4 Pre-distortion method to combat Out of band (OOB) emission

As shown in Figure 3.2, duplexer must keep providing heavy attenuation at frequencies far removed from the Tx frequency. If duplexer attenuation response peaks around the Rx frequency, the spurious spectral components can increase in power and degrade Rx SNR. Besides large and bulky duplexers, another solution that has been historically adopted to prevent Tx self-jamming is pre-distortion. Pre-distortion allows formation of a nonlinear inverse characteristic of the distorting nonlinearity and it corrects for the nonlinearity by pre-inversing the input before going into the Tx front-end. The solution is shown in some detail in Figure 3.3 because it is very relevant to the current discussion and adequately highlights the shortcomings, which are addressed by the solution proposed in this thesis.

Figure 3.3 sketches a typical pre-distortion solution where the output of the PA is coupled through an RF coupler and fed back into a receive path. This receive path is separate from the receiver itself, as it is used to down-convert and digitize the output waveform of the PA. The digitized output is then used in conjunction with an adaptive

algorithm to adapt a forward pre-distorter to the inverse characteristics of the PA. Several facts to note in this arrangement are that a separate coupler, having an attenuation of ~ 30-40 dB is required, so as not to saturate the mixer having an IIP3 of ~ 30 dBm. A complete receiver path is also required by the system which includes an ADC which must have adequate SINR to allow for system identification. A table highlighting the comparison of predistortion with a more desirable architecture is shown in Table 3.1.

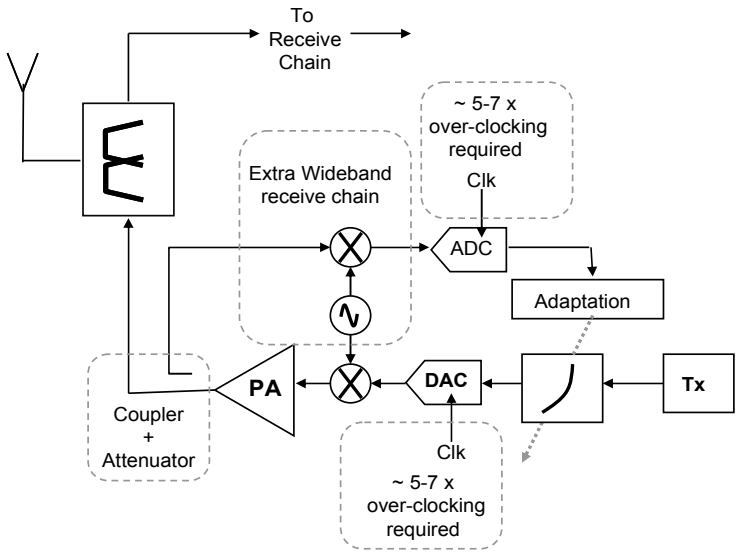

Figure 3.3. Pre-distortion and associated over-heads

TABLE 3.1
PREDISTORTION VS PROPOSED ARCHITECTURE

System Component	Predistortion	Proposed Architecture
DAC CLOCK	Requires 5-7 x over-clocking	No over-clocking required
SEPARATE ADC	Required for demodulation and base-band feedback	No requirement for a separate ADC
ADC CLOCK	Requires 5-7 x over-clocking	No overclocking required on the ADCs
SEPARATE RECIEVER CHAIN	Required, including attenuator, mixer, base-band amps and filters	No separate receive chain in required to cancel OOB emission

The ADC and DAC in the predistortion system need to be clocked at frequency $5-7\times$ higher than the Nyquist requirements of the original base-band transmit signal. This is because pre-distortion is a nonlinear transformation which necessarily expands the signal bandwidth. The exact over-clocking required is a function of correction band-width, i-e which order of nonlinear characteristic need to be compensated for. In order to cancel 3rd order distortion, system would require a 2x increase in sampling frequency. For a 5th order distortion cancellation, 4x increase in original sampling frequency is required. Having shown the tremendous area and power requirements of a pre-distorting solution, it would be helpful to consider other methodologies to tackle the OOB emission problem.

3.5 Nonlinear interference cancellation

We now propose a new system for tackling Out of Band (OOB) emission problem. The proposed system architecture is shown in Figure 3.4. A separate signal tap is used at the output of the base-band digital transmitter to supply Tx signal to a parallel chain. The key idea of design is to use this base-band digital signal and to model the RF path it encountered before being reflected back into the receiver.

The proposed architectural block is shown as a dotted line in Figure 3.4. It can be understood by tracing the Tx signal $x(n)$ out of the base-band Tx block. This signal is converted to $x(t)$ using a DAC and is subsequently up-converted to the Tx frequency f_{Tx}. After up-conversion, the signal is passed through a nonlinear PA which generates inter-modulation products. The duplexer filter is shown as $H(\omega-\omega_{Rx})$ which represents a base-band filter have a response $H(\omega)$, centered at the receiver frequency ω_{Rx}. The purpose is to be able to model the action of the receive chain on the OOB spectral

components. The received signal designated as $v(t)$ is entering the receiver at the antenna terminal. The signal before the LNA shows a superposition of attenuated Tx and the received Rx signal.

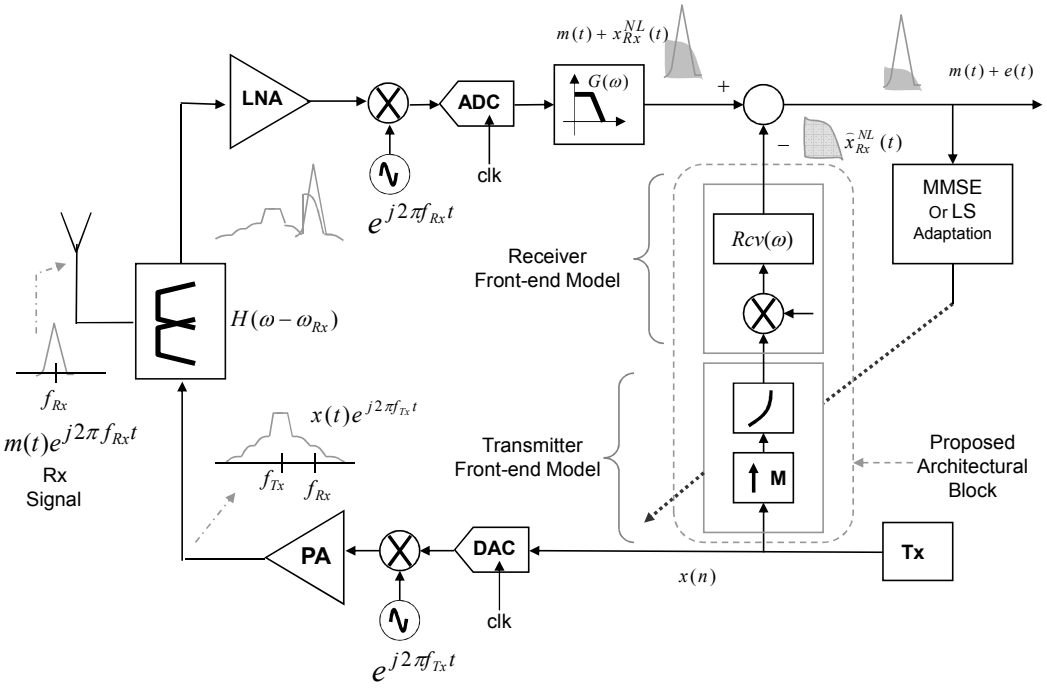

Figure 3.4 : Proposed architecture for OOB cancellation

It is noteworthy that the attenuation of the duplexer (from Tx-Rx port) is the heaviest at the transmit frequency f_{Tx}, but the weakest at the receive frequency f_{Rx}. The composite signal is processed by the receiver to yield superposition of two components, the true received signal $m(t)$ and the portion of Tx interference as shown in Figure 3.4. The proposed system (shown in dashed line) attempts to create a replica of the transmit signal interference and cancel it before going into further receive processing.

3.5.1 Nonlinear modeling of the front-end

As shown by the block diagram in dotted lines, the transmitted signal first goes through a $\times M$ up-sampler. This is essential in order to open the bandwidth span of the signal from B MHz to MB MHz. This is because nonlinear expansion in going from $x(n)$ to $\sum h(n_1\ n_2\ ...n_p)\,x(n-n_1)...x(n-n_p)$ can only be observed with increased bandwidth. The signal is then passed through a nonlinear system of volterra kernels. This system is adaptive and is able to learn the non-linearity in the RF signal path on the fly. The remaining half of the components mimic the receiver operation in the receive band. There is a mixer imitating the down-conversion operation $\delta(\omega-\omega_{Rx})$ such that the Tx emission in the receive band is centered at zero. For a base-band signal where ω_{Tx} happens to be zero, this boils down to a mixer of the form $\delta(\omega-\omega_{Tx})*\delta(\omega-\omega_{Rx})=\delta(\omega-\omega_{Rx-Tx})$ assuming that the receiver LO resides on the high side of the transmitter LO. The signal is finally passed through a receive filter $Rcv(\omega)$ which has a low pass form and cutoff equal to the receiver band-width.

We now formulate a base-band equivalent model of the scenario shown in Figure 3.4. The up-converted output signal from the transmitter passes through a polynomial nonlinearity of the PA and gets filtered with $H(\omega-\omega_{Rx})$ which is an up-converted version of the equivalent base-band filter $h(t)$. The received signal $m(t)$ is added to it and the composite is passed through a down-converter with frequency f_{Rx} and the receive bandwidth is selected by the filter $G(\omega)$. The expression for the final output $x^{//}(t)$, (assuming $m(t)=0$) can then be written as

$$x^{//}(t) = \left[g(t) * \left[e^{-j2\pi f_{Rx}t} \times \left(h(t) e^{j2\pi f_{Rx}t} \right) * \left(e^{j2\pi f_{Tx}t} f_{NL}(x(t)) \right) \right] \right] \qquad (3.9)$$

where the filter response $h(t)e^{j2\pi f_{Rx}t}$ is a pass-band response with the filter pass-band centered at the receive frequency. This pass-band response gets multiplied with the exponential $e^{-j2\pi f_{Tx}t}$ to yield a base-band version of $h(t)$ centered at the zero frequency. The expression can then be written as

$$x^{//}(t) = [g(t) * h(t)] * [e^{-j2\pi(f_{Rx} - f_{Tx})t} f_{NL}(x(t))] \qquad (3.10)$$

the function f_{NL} is a nonlinear distorting function which represents the response of the power amplifier. The approximation theory results tell us that a general nonlinear function can be represented as a linear combination of kernel functions as the following.

$$f_{NL}(x) = \sum_{k=1}^{P} a_k \phi_k(x) \qquad (3.11)$$

where ϕ_k are polynomial kernels which range from $\phi_k = [x^1 \quad x^2 \quad x^3 \quad ..... \quad x^p]$ as k varies from 1 **to** p. From the knowledge of nonlinear distortion in RF spectrum, we know that only odd order nonlinearities actually contribute to the in-band distortion as well as adjacent channel spectral leakage. The even order nonlinearities generate spectral products which are far out-of-band. Since we are interested in Tx emission in the adjacent receive bands, we restrict our kernels to $\phi_k = [x^1 \quad x^3 \quad x^5 \quad ..... \quad x^{2k+1}]$. Using these kernel functions one can predict the nonlinearities causing emission in the adjacent channels. Our nonlinear formulation can also benefit from the apriori knowledge that we are only interested in Tx emission falling within the received signal bandwidth. All the remaining spurious components would be necessarily filtered out by the receive filter.

There is no use in computing the nonlinear products which do not appear in the final received signal. We can therefore prune the kernel series further by writing

$$\tilde{f}_{NL}(x) = \sum_{k=m}^{p} a_k \phi_k(x) \qquad (3.12)$$

where $\tilde{f}_{NL}(x)$ represent the modified nonlinear function, and m is the starting point of kernels which contribute to the distortion in the receiver. The value of m is the same as calculated in section 3.2. We can now justify the computation of m by looking at the effect of nonlinear distortion on spectral leakage as shown in Figure 3.5.

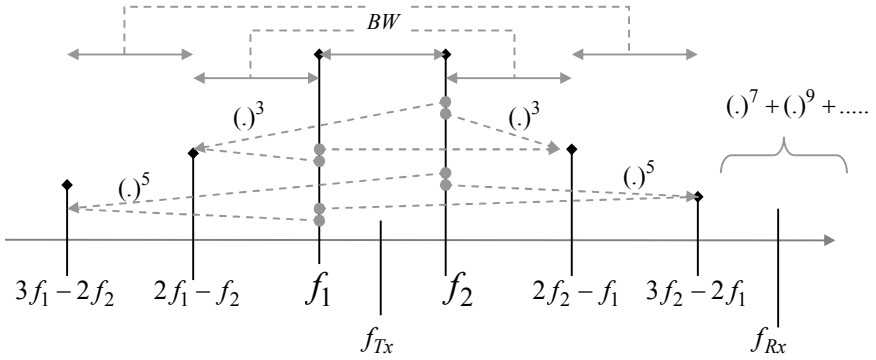

Figure 3.5. Spectral expansions from different nonlinear orders

The figure shows a transmit frequency f_{Tx} bounded by two frequencies f_1 and f_2 which represent the band of operation. The even order distortion will cause spectral expansion. The figure shows how a third order distortion $(.)^3$ will cause spectral expansion to the left and right of transmit frequency. The highest adjacent channel frequency of this expansion is given by $2f_2 - f_1$ and lies at a distance of $1 \times BW$ away from the transmit band. Similarly the lowest frequency of this distortion product given by $2f_1 - f_2$ is located $1 \times BW$ away to the low side of the transmit LO. Similarly the highest adjacent frequency of the 5th order product, $3f_2 - 2f_1$ lies at a distance of $2 \times BW$ away from the edge of the

transmit band. The figure also shows the receive frequency f_{Rx} which lies beyond the 5th order distortion product range. For this given receiver frequency the distortion products affecting the received signal would range from 7th , 9th and higher order nonlinearities.

3.5.2 Adaptive system identification

Having determined the value of m and using this pruned volterra kernel series, we can write $x^{//}(t)$, the portion of transmit signal interference (by a transmitter operating at frequency f_{Tx}) and received by a receiver (operating at f_{Rx}) at its base-band output is given by,

$$x^{//}(t) = \left[g(t) * h(t)\right] * e^{-j2\pi(f_{Rx}-f_{Tx})t}\left[\sum_{k=m}^{p} a_k \phi_k(x)\right] \qquad (3.13)$$

where the exponential term $e^{-j2\pi(f_{Rx}-f_{Tx})t}$ is a one to one mapping of frequency components and can be taken inside the summation which leads to,

$$x^{//}(t) = \left[g(t) * h(t)\right] * \left[\sum_{k=m}^{p} a_k e^{-j2\pi(f_{Rx}-f_{Tx})t}\phi_k(x)\right] \qquad (3.14)$$

This represents a down-conversion of each of the kernel components before being summed together using scaling coefficients a_k's. The convolution $g(t) * h(t)$ can be combined and represented as a single low-pass filter $rcv(t)$ at the receiver input. The convolution operator between the first and second half of equation is a linear operator and can be taken inside the summation sign as well. Our objective in doing such manipulation is to come up with a version of equation which can be used to adaptively estimate the nonlinear system response. After making the required substitutions, we can write eq as

$$y(t) = \sum_{k=m}^{p} a_k rcv(t) * e^{j2\pi(f_{Rx}-f_{Tx})t}\phi_k(x) \qquad (3.15)$$

and this yields an expression which can be used to estimate the nonlinearity $\tilde{f}_{NL}(x)$ in the signal path of the transmit signal. We can formulate a discrete time estimator for $y(t)$ by writing a vector form equation using kernel transformation, down-conversion and filtering operators.

$$\hat{y}(n) = A_{mp}.\left(Rxfilt_{1\times L}.X_{mp} \right)^{T} \qquad (3.16)$$

where A_{mp} is a row vector having components $A_{mp} = [a_m \quad .... \quad a_p]$, X_{mp} has dimensions $L \times Q$, where Q is the number of kernels ($p-m$) and *Rxfilt* is a filtering vector given by,

$$Rxfilt_{1\times L} = \left[rcv(0) \quad .. \quad .. \quad rcv(L) \right] \qquad (3.17)$$

where L is the order of the equivalent digital FIR receive filter and

$$X_{mp} = \begin{bmatrix} ... & \Phi_{mp}(n) & ... \\ ... & \Phi_{mp}(n-1) & ... \\ ... & .. & ... \\ ... & \Phi_{mp}(n-L) & ... \end{bmatrix} \qquad (3.18)$$

where $\Phi_{mp}(n) = e^{-j2\pi\frac{f_{Rx}-f_{Tx}}{f_s}} \left[\phi_k(x(n)) \quad \phi_{k+1}(x(n)) \quad .... \quad \phi_{k+p}(x(n)) \right]$ is a single row in the X_{mp} matrix and consists of multiplication of each of the kernel functions with the complex down-converting exponential. The kernels are starting from order m and going up to order p whereas each row of the matrix X_{mp} represents the evaluation of kernel functions for a single time step. Given that we need some adaptive mechanism to update the coefficient vector A_{mp}, the entire cancellation system and equivalent transceiver base-band model can be represented as a signal flow shown in Figure 3.6.

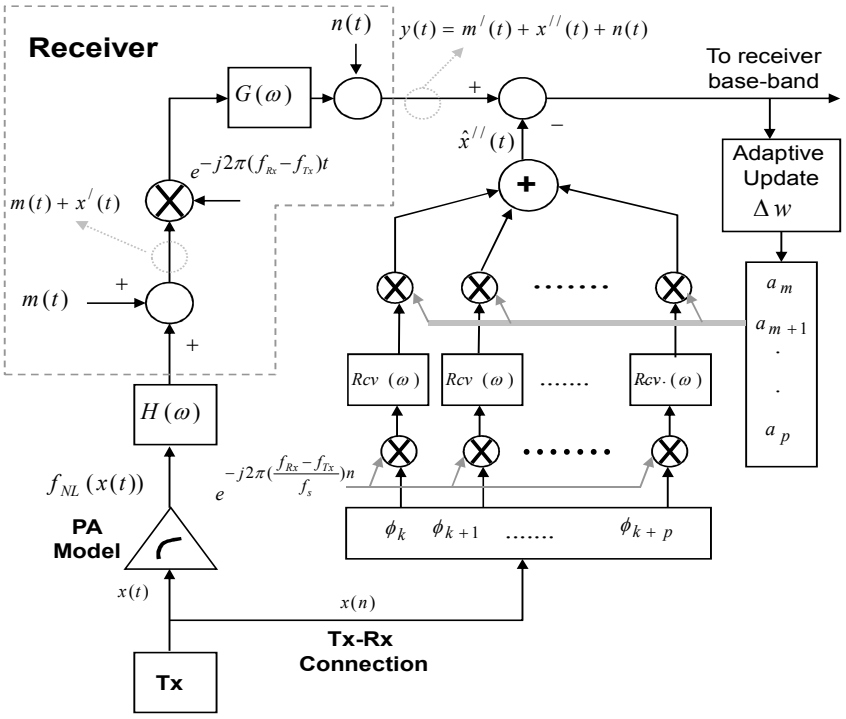

Figure 3.6. Base-band model of the proposed cancellation

A least squares solution to eq 3.16 can be found by minimizing the sum of squared error, and is given by

$$A_{mp} = \left[(Rxfilt.X_{mp})^T (Rxfilt.X_{mp}) \right]^{-1} Y \qquad (3.19)$$

where $Y_{L\times 1}$ is a vector of output samples $y(n)$. For the purpose of real time implementation, we formulate it as a recursive least squares problem and write the vector $\mathbf{U}$ as $\mathbf{U} = Rxfilt.X_{mp}$ and define and initialize an inverse autocorrelation matrix of the form $\mathbf{S}(-1) = \delta(I)_{Q\times Q}$. The instantaneous error is formed from the product of kernelized input $\mathbf{U}$ and the weight vector A_{mp}

$$e(n) = y(n) - \mathbf{U}(n) A_{mp}(n-1) \qquad (3.20)$$

an intermediate matrix for updated the correlation matrix is formed using

$$\boldsymbol{\psi}(n) = \mathbf{S}(k-1)\mathbf{U}(n) \qquad (3.21)$$

and the update of the inverse correlation matrix can be accomplished by

$$\mathbf{S}(n) = \frac{1}{\lambda}\left[\mathbf{S}(n-1) - \frac{\boldsymbol{\psi}(n)\boldsymbol{\psi}^T(n)}{\lambda + \boldsymbol{\psi}^T(n)\mathbf{U}(n)}\right] \qquad (3.22)$$

where λ is the forgetting factor and a very important parameter of the RLS algorithm. It determines how the effect of past input decays with respect to the estimation of current output. We will see later that λ has an important role to play in determining the quality of interference cancellation. The last update is that of the coefficient vector and is equal to $\Delta A_{mp} = e(n)\mathbf{S}(n)\mathbf{U}(n)$. The update equation can be written as,

$$A_{mp}(n) = A_{mp}(n-1) + e(n)\mathbf{S}(n)\mathbf{U}(n) \qquad (3.23)$$

Together eq(3.16-3.23) along with the formation of $\mathbf{U}$ constitute the adaptive update algorithm that is used to perform adaptive cancellation. On the right of Figure 3.6 is a vertical portion representing the transmitter and receiver chain with the receiver boundary being delineated in the dotted line. On the left is the estimation system outlined in the discussion. Figure 3.6 assumes that Transmit signal has been over-sampled by a sufficient amount to be processed by volterra kernels. We see that each kernel transformation is separately processed by the receive filter. This is the most straightforward way to approximate the nonlinear transformation happening in the combined Tx-Rx front end of the radio. The receive filter is a very sharp filter (with filtering performed in multiple stages of the receiver front-end) and has a heavy computational load. The computational complexity of this architecture is therefore high and scales up with the increase in the maximum approximating order p. This situation is not desirable. We now propose a modified formulation that is able to cut down significantly on the computational complexity of the proposed architecture.

3.6 Reduced complexity interference cancellation

The complete update equation for the kernel coefficients is given by

$$A_{mp}(n) = A_{mp}(n-1) + \mathbf{S}(n)\mathbf{U}(n)\left[y(n) - A_{mp}(n-1)\mathbf{U}(n) \right] \qquad (3.24)$$

with the current formulation of $\mathbf{U}$ being given by $\mathbf{U} = Rxfilt.X_{mp}$. Hence the expanded update equation can be written as

$$A_{mp}(n) = A_{mp}(n-1) + \mathbf{S}(n)\mathbf{U}(n)\left[y(n) - A_{mp}(n-1).Rxfilt.X_{mp} \right] \qquad (3.25)$$

In order to reduce the instances of received filters, the coefficient vector A_{mp} must be applied to the nonlinear kernels before the application of receive filter operators i-e the prediction $\hat{y}(n)$ must be formulated as

$$\hat{x}^{//}(n) = Rxfilt.A_{m-p}(n-1).X_{mp} \qquad (3.26)$$

as opposed to the previous instance of $\hat{y}(n)$ formation which was given by $\hat{x}^{//}(n) = A_{m-p}(n-1).Rxfilt.X_{mp}$. But the new formulation of $\hat{y}(n)$ can no longer be used in the formation of estimation error because the $\hat{x}^{//}$ and X_{mp} are offset from each other through the delay of the receive filter $Rxfilt$. The error $e(n) = y(n) - \hat{x}^{//}(n)$ used to adapt the coefficients would therefore correspond to the input X_{mp} that occurred D samples earlier, where D is the group delay of the receive filter. We can therefore synchronize the prediction $\hat{x}^{//}$ and the actual output by delaying the input X_{mp} and feeding the delayed replica, for the computation of weight update in this interference cancellation arrangement. The modified architecture is shown in Figure 3.7. The equation below shows the shift in the operators which lead to the hardware reduction.

$$A_{m-p}(n) = A_{m-p}(n-1) + \mathbf{S}(n)\mathbf{U}(n)\left[y(n) - A_{m-p}(n-1).Rxfilt.X_{mp} \right] \qquad (3.27)$$

Figure 3.7 represents a path for kernel functions which represents an array of values with a bold grey line. The dot product of kernel functions is formed prior to filtering and hence only uses a single received filter. A delayed extra parallel path is required for coefficient update.

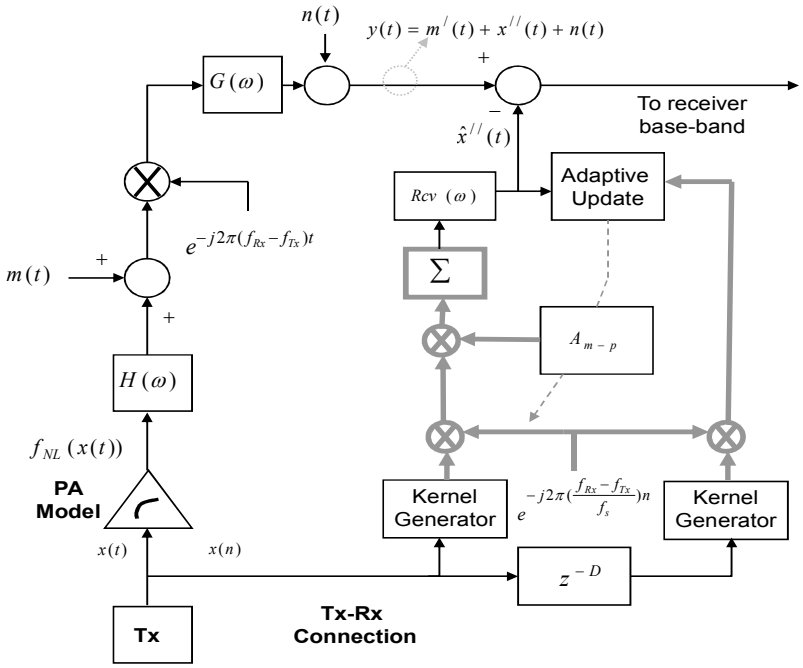

Figure 3.7. Modified hardware efficient architecture

The computational complexity can also be decreased by using multi-rate signal processing to down-sample the signals after passing through the receive filter. Since the receive filter curtails the bandwidth to the extent required by the receiver, decimators can be used after that to provide substantial computational savings.

3.7 Generalized Interference Cancellation

The previous sections have demonstrated the use of Volterra kernels to perform interference cancellation. This requires nonlinear estimation of Volterra series coefficients. We accomplished this estimation using a cascade of linear and nonlinear structures and performing linear estimation of coefficients. In this section, we generalize

this estimation theory to include estimation in Hilbert space of functions, by connecting together ideas from reproducing kernel spaces, adaptive kernel LMS methods, and the architecture that we have derived in the last section. The structure derived in the last section, allows us to use the modern statistical regression tools and write an elegant formulation. This part of the chapter reviews a little background on RKHS framework and goes on to show that this can be gainfully applied for online estimation in radio front-ends. Although plenty of theory on kernel spaces exists, it has never been applied and demonstrated in the context of radio front-ends. We show that useful simplifications are possible in this domain and they can be used to obtain advantages in terms of computational complexity.

We begin by highlighting Mercer's Theorem, which is used in the context of support vector machines. It states that any continuous symmetric kernel $k(\mathbf{x},\mathbf{x}')$ that is defined in a close interval $a \le \mathbf{x} \le b$ and like-wise for $\mathbf{x}'$ can be expanded in the series given by equation

$$k(\mathbf{x},\mathbf{x}') = \sum_{i=1}^{\infty} \gamma_i \varphi_i(\mathbf{x}) \varphi_i(\mathbf{x}') \qquad (3.28)$$

with positive coefficients $\gamma_i > 0$ for all i. For this expression to be valid, and for it to converge absolutely and uniformly, the kernel $k(\mathbf{x},\mathbf{x}')$ must satisfy the positive definiteness property. In other words

$$\int_b^a \int_b^a k(\mathbf{x},\mathbf{x}')\psi(\mathbf{x})\psi(\mathbf{x})\, d\mathbf{x}\, d\mathbf{x}' > 0 \qquad (3.29)$$

holds for all $\psi(.)$ as long as they satisfy

$$\int_a^b \psi^2(\mathbf{x}) d\mathbf{x} < \infty \qquad (3.30)$$

The power of Mercer's theorem lies in the fact that it relates a Kernel function as a dot product of two identical nonlinear functions. This property will be very effective in fast computation of our estimators. It also puts a limit on admissible kernel functions which can be used for nonlinear estimation.

Now considering a Mercer's kernel $k(\mathbf{x},.)$, let F be any vector space of all real valued functions of $\mathbf{x}$ that are generated by the kernel $k(\mathbf{x},.)$. If we pick up a function $f(.)$ from the space F, we can represent the function using

$$f(.) = \sum_{i=1}^{l} a_i k(\mathbf{x}_i,.) \qquad (3.31)$$

Similarly we can define another function $g(.)$ as

$$g(.) = \sum_{j=1}^{n} a_j k(\tilde{\mathbf{x}}_j,.) \qquad (3.32)$$

Given $f(.)$ and $g(.)$ we can introduce the bilinear form and write it as

$$\langle f, g \rangle = \sum_{i=1}^{l} \sum_{j=1}^{n} a_i k(\mathbf{x}_i, \tilde{\mathbf{x}}_j) b_j \qquad (3.33)$$

which can be written as

$$\mathbf{a}^T \mathbf{K} \mathbf{b} \qquad (3.34)$$

where $\mathbf{K}$ is the Gram or kernel matrix. We have also made use of the relation

$$k(\mathbf{x}_i,.)k(\mathbf{x}_j,.) = k(\mathbf{x}_i, \mathbf{x}_j) \qquad (3.35)$$

By virtue of above equations we can readily derive that the bilinear form of functions obeys the properties of symmetry, scaling and distributive, and having a square norm greater than or equal to zero. Since it satisfies all these properties it is indeed a dot product in the function space. One additional property that it exhibits is of interest to us, which can be obtained by substituting

$$g(.) = k(\mathbf{x},.) \qquad \text{` (3.36)}$$

and so substituting in eq 3.33 for dot product gives us

$$\begin{aligned} \langle f, k(\mathbf{x},.) \rangle &= \sum_{i=1}^{l} a_i k(\mathbf{x}, \mathbf{x}_i) \\ &= \sum_{i=1}^{l} a_i k(\mathbf{x}_i, \mathbf{x}) \\ &= f(\mathbf{x}) \end{aligned} \qquad (3.37)$$

This property of the Mercer's kernel is referred to as the reproducing property. This property gives a reproducing structure to a Hilbert space which can then be referred to as a reproducing kernel Hilbert space (RKHS).

We can evaluate $f(.)$ at a number of points, and from the above discussion, express it as follows

$$f(\mathbf{x}_j) = \left\langle \sum_{i=1}^{l} a_i k(\mathbf{x}_i,.), k(\mathbf{x}_j,.) \right\rangle \qquad (3.38)$$

which can be written as

$$f(\mathbf{x}_j) = \sum_{i=1}^{l} a_i k(\mathbf{x}_i, \mathbf{x}_j) \qquad (3.39)$$

which is a statement of the Representer theorem. Representer theorem says that any function defined in an RKHS space can be represented as a linear combination of Mercer's Kernel functions using a set of points. Many different kernel functions can exist, but the Gaussian and the polynomial kernels are very famous. Gaussian kernel is given by

$$k(\mathbf{x}, \mathbf{x}') = \exp\left(\frac{\left\| \mathbf{x} - \mathbf{x}' \right\|^2}{2\sigma^2} \right) \qquad (3.40)$$

where as a polynomial kernel is given by

$$k(\mathbf{x},\mathbf{x}') = \left(\mathbf{x}^T\mathbf{x}' + 1\right)^p \tag{3.41}$$

where the degrees of freedom available in them are the parameter σ in the case of Gaussian kernel (which determines the spread of the function around each point) and the order p in the case of polynomial kernels. Using the exponential kernel can allow us to transform our inputs into possibly infinite dimensional space, which can be used to estimate highly nonlinear responses. Such estimation can be performed using a simple adaptive algorithm, like Kernel-LMS (KLMS) for example, which can yield very low complexity accurate filters for nonlinear interference reconstruction. A KLMS algorithm as detailed out in [45] begins by writing the output of the nonlinear system as

$$\tilde{f}_{NL}(\mathbf{x}(i)) = \mathbf{w}^T\varphi\left(\mathbf{x}(i)\right) \tag{3.42}$$

where i is the time index of input x and k is the order index of the nonlinear coefficients, and $\varphi(.)$ is the nonlinear operator transforming the input data from a lower order linear space to a higher dimensional space. We can then write the approximation error and the weight update using simple instantaneous gradient update

$$\begin{aligned} e(i) &= d(i) - \mathbf{w}^T(i-1)\varphi\left(\mathbf{x}(i)\right) \\ \mathbf{w}(i) &= \mathbf{w}(i) + \eta e(i)\varphi\left(\mathbf{x}(i)\right) \end{aligned} \tag{3.43}$$

if the weight update iteration is continued in this manner from time index 1 to i we can write an expression for weights at the time index i to be

$$\mathbf{w}(i) = \eta\sum_{j=1}^{i} e(j)\varphi\left(\mathbf{x}(j)\right) \tag{3.44}$$

The output of the system to a new input $\mathbf{x}'$ can be expressed using the dot product of the weight vector and the input

$$\begin{aligned}\mathbf{w}(i)^T\varphi(\mathbf{x}^{/}) &= \left[\eta\sum_{j=1}^{i} e(j)\varphi(\mathbf{x}(j))\right]\varphi(\mathbf{x}^{/}) \\ &= \eta\sum_{j=1}^{i} e(j)\left[\varphi(\mathbf{x}(j))^T\varphi(\mathbf{x}^{/})\right]\end{aligned} \tag{3.45}$$

At this point we can use eq (3.28) to write the product inside the square brackets as an evaluation of a nonlinear kernel function by writing

$$\mathbf{w}(i)^T\varphi(\mathbf{x}^{/}) = \eta\sum_{j=1}^{i} e(i)k(\mathbf{x}(j),\mathbf{x}^{/}) \tag{3.46}$$

which is commonly referred to as the kernel trick. The kernel trick allows us to write the output equation as a sequence of kernel evaluations. This is particularly important because the transformation to higher dimensional space is now being done implicitly as opposed to the earlier architecture where explicit transformation is performed and the solutions may suffer from curse of dimensionality, especially when the nonlinear system is suffering from significant memory effects (caused by finite bandwidth biasing circuits and thermal time constants). The overall algorithmic update for the KLMS recursion can be written as follows

$$\begin{aligned}&\tilde{f}_{NL(i-1)} = \eta\sum_{j=1}^{i-1} e(j)k(\mathbf{x}(j),.) \\ &\tilde{f}_{NL(i-1)}(\mathbf{x}(i)) = \eta\sum_{j=1}^{i-1} e(j)k(\mathbf{x}(j),\mathbf{x}(i)) \\ &e(i) = d(i) - \tilde{f}_{NL(i-1)}(\mathbf{x}(i)) \\ &\tilde{f}_{NL(i)} = \tilde{f}_{NL(i-1)} + \eta e(i)k(\mathbf{x}(i),.)\end{aligned} \tag{3.47}$$

One can see that the algorithm accomplishes its action by allocating an adaptive unit with each new input. Thus it suffers from the uninhibited growth of nonlinear coefficients which must be pruned to manage the computational complexity of this scheme effectively. In the case of nonlinear RF PA systems which we are interested in, the complexity can be easily managed by looking at the IIP_3 / P_{1dB} of the RF component or

overall system. The total dynamic range of the receiver is generally approximated by the expression

$$DR_{Rcvr} = \frac{2}{3}\left(IIP_3 - NoiseFloor\right) \tag{3.48}$$

The P_{1dB} is a point for the onset of nonlinearities. The AM/AM and AM/PM distortion of the PA therefore manifests itself most sharply in the nonlineat regime of operation. By recognizing the fact that P_{1dB} point correlates with the onset of nonlinearities, we can include an input element to the dictionary only in the case of exceeding a certain threshold determined by the characteristics of the RF front-end. The allotment of coefficients can be sparse in the region of low nonlinearity and more dense in the region of higher nonlinearity.

Once a new element (input output pair) is encountered, its location is checked within the available dynamic range of the system. Based on its location, it is compared with all the elements available in one of the dictionaries. If the distance from any of the elements of the dictionary satisfies the threshold criterion, the element is added to the dictionary, otherwise it is neglected. When the steady state MSE of the system has grown down below a certain level, the continuous evaluation may well be stopped. This will drastically reduce the complexity because only kernel transformations on the input need to be performed. In authors experience, the update to dictionary is not required after 30-40 iterations with an LTE 10 MHz signal. In reality the convergence will depend upon the type of nonlinearity being modeled and the extent of bandwidth for which the model should hold.

We can thus summarize the algorithm for kernel update in the form given in Algorithm GIC (Generalized Interference Cancellation).

Algorithm GIC : Nonlinear RF Front-end Identification
using Kernel Methods

Inititialization

Choose step size parameter η (range 0.001 to 0.1)

Choose Kernel specification $K(x,x)$

Compute the total dynamic-range of signal excursion
using the expression in eq (3.7)

Estimate order of the system M

Allot 1/3rd of the order to the first half of the DR and
2/3rd of the order to the second half (before and after P_{1dB})

Determine two different thresholds δ_1 and δ_2 for
including the input point in the dictionary

Initialize $\mathbf{a}_1 = \eta d(1)$, $Dict(1) = [x(1)]$, $\widehat{f}_{NL}(1) = \mathbf{a}_1 K(x(1))$

Initialize Depth of the dictionary to $i = 1$

Computation

@ the next available input-output pair $\{ x(n), d(n) \}$

{

$$\widehat{f}_{NL}(x(n)) = \sum_{j=1}^{i} \mathbf{a}_j K(x(n), x_j)$$

Computer output using eq

Compute the error $e = d - \widehat{f}_{NL}(x(n))$

if ($x(n) < P_{1dB}$ **and** $\min\{[x(n) - Dict(i-1)]\} > \delta_1$)

$$\{ \; Dict(i+1) = \{x(n)\} \; ; \quad a_i = \eta e \; ; \; i++ \; \}$$

else if $x(n) > P_{1dB}$ **and** $\min\{[x(n) - Dict(i-1)]\} > \delta_2$

$$\{ \; Dict(i+1) = \{x(n)\} \; ; \quad a_i = \eta e \; ; i++ \; \}$$

}

End Nonlinear RF front-end Identification

This algorithm can be used to obtain very compact low order nonlinear filters for interference cancellation in receivers. We were able to demonstrate very good performance and low computational complexity with such an algorithm.

3.8 Simulation and measurement results for interference cancellation

The adaptive nonlinear cancellation systems discussed above have been simulated using MATLAB and SIMULINK tools. The system was built using HSUPA and LTE signal, over-sampled by 12x. This can accommodate nonlinearities upto 11th order. The

initial signal was output at the rate of 122.88 MHz and passed through a nonlinear input-output mapping and down-converted and filtered with the receive filter selecting the receive bandwidth of 5 MHz. The interference contained within this bandwidth is to be estimated by the adaptive systems described in the earlier sections. To simulate the received signal , a dual carrier downlink signal was added to the interference in a certain SNR ratios. We will describe some of the measurements which will characterize the performance of the system. In order to do that, we must first understand some of the signals present in a system like this. A summary of them is shown in the Figure 3.8.

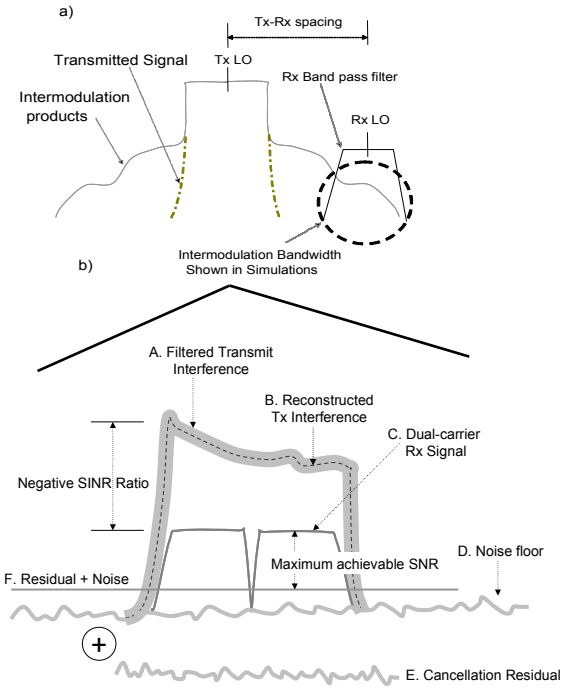

Figure 3.8. Simulated signals and relative spectrums

Part a) of the figure shows in dotted line, the portion of transmit signal interference which is magnified in Part b). The transmit signal interference is exaggerated by assuming a very low selectivity duplexer. A receive dual carrier signal is also embedded within this interference. Signal strength of the received signal is less than that of the transmit interference and we are therefore operating under a negative SINR scenario where

received signal cannot be decoded without adequate interference cancellation. If we are successfully able to cancel transmit interference, we will be left with interference residual (Trace E) which will add to the system noise floor to create a new floor (Trace F) that will determine the final SNR of the receiver signal.

We therefore formulate two metrics of performance defined by Tx MSE and Rx SNR to characterize the performance of these simulations. The terms used to characterize the performance are the ones used in Figure 3.6. Tx MSE is defined as

$$Tx\_MSE_{dB} = -1 \times 10 \log_{10} \frac{E[(Tx\_leak - T\hat{x}\_leak_{Estim})^2]}{E[(Tx\_leak)^2]} \qquad (3.49)$$

which represents the quality of interference prediction by the estimation systems discussed in the earlier sections. Substituting quantities from Figure 3.6 would give us,

$$Tx\_MSE_{dB} = -1 \times 10 \log_{10} \frac{E[(x^{//} - \hat{x}^{//})^2]}{E(x^{//2})} \qquad (3.50)$$

The second metric of performance Rx SNR is given in terms of system quantities as

$$Rx\_SNR_{dB} = 10 \log_{10} \frac{E[(Rcvd - TxLeak_{Estim})^2]}{E[(Rcvd_{Injected})^2]} \qquad (3.51)$$

Substituting these quantities with those shown in the base-band equivalent model of Figure 3.6 will yield,

$$Rx\_SNR_{dB} = 10 \log_{10} \frac{E[(y - \hat{x}^{//})^2]}{E[m^{/2}]} \qquad (3.52)$$

The SNR's on different branches in the simulation system can be changed to yield realistic values actually propagating in the radio system. The results of one such experiment are shown in Figure 3.9 below.

The figure is a periodogram plot of several signals present in a system. The first trace shows a composite signal $y(t) = m'(t) + x''(t) + n(t)$ consisting of received signal, noise, and the transmitter out-of-band emission leaking into the receiver. In this particular experiments, the value of emission is 20 dB above the noise floor, such that the $E\left(x''(t)^2\right) / E\left(n(t)^2\right) = 20dB$. The received signal added at the antennae is only 10 dB above the noise floor $E\left(m'(t)^2\right) / E\left(n(t)^2\right) = 20dB$. In other words, received signal is completely buried within the interference present and hence having a negative SINR.

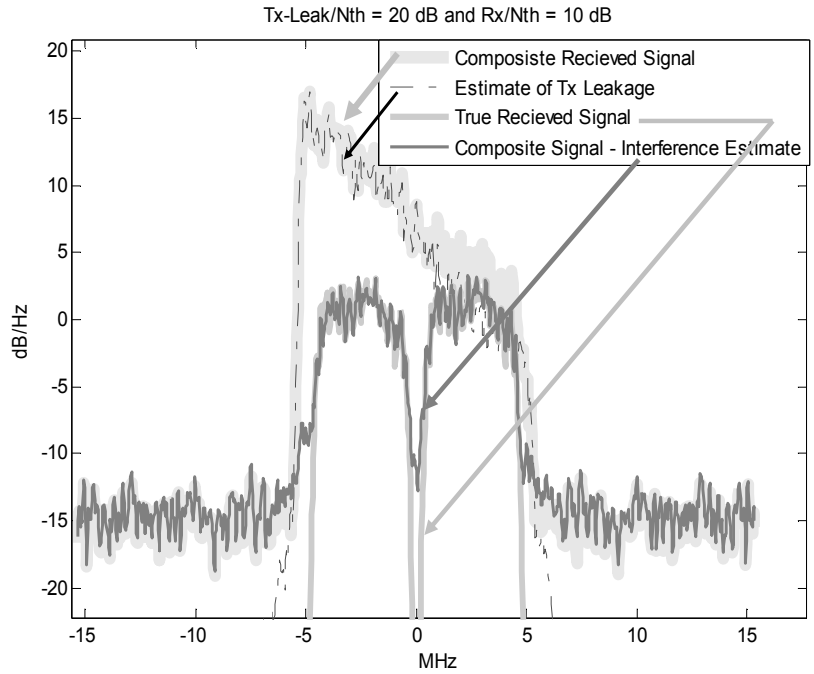

Figure 3.9 Simulation results for SINR of ~ 10 dB

The second trace shows an estimate of the Tx Leakage formed by the nonlinear estimation system using volterra kernels. Once the estimate is subtracted from the composite signal, the received signal and residual interference are left (along with noise) which is shown as Trace 4. If the cancellation system is able to function well, this resulting signal should be very close to the original pure received signal $m(t)$. This is

shown by superimposing the $m(t)$ spectrum as Trace 3. The results show that the recovered received signal, very closely conforms to the original received signal. The exact measure of comparison is shown by the Rx_SNR metric. The experiment is performed for several practically useful values of the received signal and interference and the results are tabulated in Table 3.2. The first row of the table shows a scenario where high Tx leakage can completely swamp the Rx signal. The system shows good reconstructed performance and can restore the receive SINR from -15 dB to 2.89 dB. When the received signal is already above the Tx signal with an SINR of 10 dB, the system acts to maintain the nominal SINR.

Measurements were performed using an HSUPA signal with a commercial handset PA operating at an output power of 26 dBm. Figure 3.10 shows the experimental setup

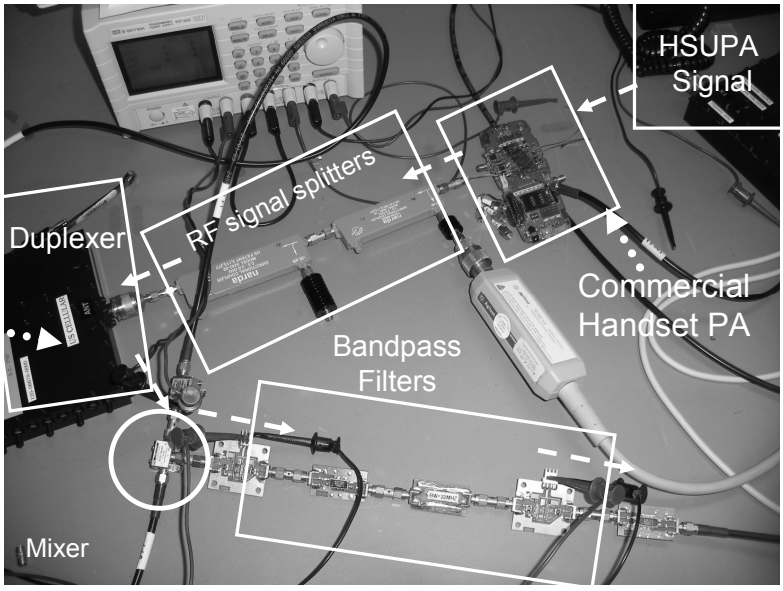

Figure 3.10 Experimental setup for validation

An HSUPA waveform generator is used to inject RF signal into a handset PA working in its compression regime. The RF output is passed through a cell-band duplexer and then mixed down to base-band. The mixer output is then passed through two cascaded SAW filters to capture the 10 MHz wide portion of the emission. This is then sampled into the logic analyzer with a sample rate of 30.72 MHz.

Figure 3.11, shows the results of post processing with the acquired data. The acquired data was run through the same setup as given in Section 3.3.

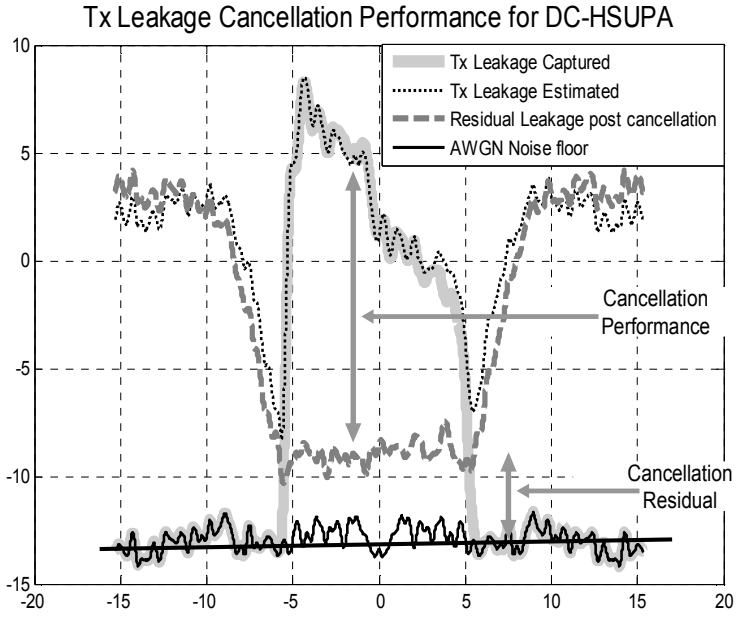

Figure 3.11 . Measurement results on the RF test bench

As shown in the figure, we had a Tx_leakage of ~ 20dB into the received path. The nonlinear adaptive cancellation system produced a replica shown in the dashed curve. After the subtraction of these two, we are left with a residual interference which is only ~ 2 dB above the noise floor. Hence ~ 18 dB of cancellation performance was obtained with the measurements. The result shows that it is indeed possible to cancel spurious

components leaking into the receiver, with an adaptive interference cancellation scheme that borrow its elements from volterra kernel theory and can additionally be generalized using kernel regression theory.

The experiment was repeated for some representative scenarios of Tx and Rx signal SNRs. The results are shown in Table 3.2.

TABLE 3.2
RECEIVED SIGNAL RECOVERY PERFORMANCE

SCENARIO		PERFORMANCE	
Tx Leakage / Nth (dB)	Rx/ Nth (dB)	Tx_MSE (dB)	Rx_SNR (dB)
20	5	23.99	2.89
20	10	19.01	6.20
10	15	4.56	8.34
10	20	-0.41	9.22

We observe from the first row that in the presence of high Tx leakage, the system is able to perform the estimation very well and give a good MSE of ~ 24 dB. The received signal SNR (Rx/Nth) which had deteriorated to (5-20=-15 dB) is restored to 2.89 dB which is a significant improvement. In the presence of a very strong Rx signal, the estimation does not perform at all. It gives an MSE of -0.41 (last column). But this is also the case, in which the cancellation performance is least required, because the received signal is already stronger than interference and does not need any boosting. We therefore conclude that in all the scenarios where it is needed, the cancellation is able to perform well and give a boost in SNR.

3.9 Conclusion

Future wireless systems will suffer from increasing interference from co-located or closely located radios. The chapter explored a particular instance of this interference scenario, where transmitter is self-jamming its own receiver due to significant emission levels present in the receive band caused by wider bandwidth system and reduced duplexer spacing. We proposed a novel compensation scheme based on a digital adaptive NL filter to faithfully reconstruct and cancel the Tx OOB generated by the PA intermodulation products.. The technique has been simulated with excellent performance gains. Finally we have demonstrated the applicability by verifying it on a real commercial handset PA.

Chapter 4

Coexistence in Radios with Multiple Receivers

Modern radio front-end chips house an increasingly dense array of circuits. This is due to the integration of many different radio standards on a single platform. The integration results in multiple RF receivers with non-harmonically related receive frequencies working in parallel . The receiver LO's use a complex network of frequency synthesizers to generate a whole range of receive frequencies. The frequency synthesis uses highly nonlinear components and the signals are increasingly coupled to each other through various substrate coupling mechanisms [46]. The resulting spurs can fall in the vicinity of Tx frequency and can down-convert a very strong Tx signal to the base-band. This can lead to a strong interference to the received signal and can substantially reduce the SINR of the received signal. In this chapter we look at a novel compensation scheme for radio systems with spurious receiver LO's. The action of LO can be cancelled by using an adaptive cancellation scheme which tries to reconstruct a replica of transmit signal interference. A theoretical framework is developed around ideas in RF systems and adaptive signal processing to realize architectures for such cancellation. A practical demonstration is performed on commercial RF front-ends to demonstrate the feasibility of this approach to enabling flexible, tunable, highly integrated RF front-ends.

4.1 The problem of spurious receivers

The radios of tomorrow face increasingly big challenges. These result from aggregation of standards on a single radio platform, and the aggressive scaling of semiconductor technology nodes. The aggregation of different radio standards on a single platform leads

to the need for highly complex frequency synthesizers. These should be able to provide multiple frequency outputs and tuning ranges, along with low phase noise. The different frequency outputs from synthesizer systems are arbitrary and may not be harmonically related to each other. The frequency synthesizer is composed of nonlinear components itself which include frequency multipliers and dividers. This leads to nonlinear interactions between various different LO frequencies, and these nonlinear interactions lead to spurs in the receiver LO. If the spur falls close to the Tx frequency, it can lead to the down-conversion of Tx spectrum to the base-band, where it interferes with the received signal and reduces the SINR ratio [47]. This action of the transmitter is referred to as self-jamming, and has been addressed in the literature as a Tx cancellation problem in different contexts.

Our discussion is centered around a fully baseband architecture which can enable transceivers to operate in this environment using proposed techniques without significant deterioration in the SINR. The problem and the associated proposed solution is shown in Figure 4.1. It shows that a signal from the transmitter referred to as u passes through the DAC and gets up-converted to the Tx frequency f_{Tx}. The signal passes through the duplexer and onwards to the antenna. The received signal $v(t)$ enters at the antenna and is to be demodulated by the receiver. It passes through the duplexer which is designed to preserve all the components of the received signal. The duplexer is a three port element having different frequency response between each pair of ports. The response of the duplexer from antenna to receiver called G_{Ant-Rx} is designed to equal one. Similarly the response of the duplexer from transmitter to antenna G_{Tx-Ant} is also designed to be unity. The duplexer response from the Tx to Rx port is heavily attenuated, and is referred to as

$G(\omega)$ in the figure. This response is centered at the transmit frequency f_{Tx} and is meant to attenuate any transmitter signal from entering the receiver and degrading its linearity performance. The receiver's front-end IIP determines the maximum amount of interference it can tolerate from the residual transmit leakage.

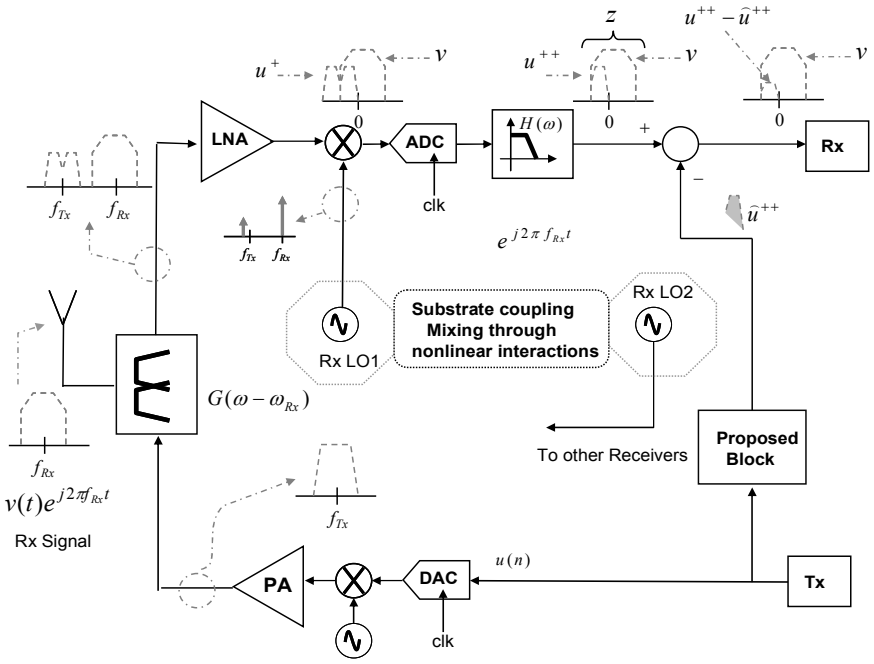

Figure 4.1 Problem illustration of RFICs with spurious receivers

Rx LO 1 as shown in Figure 4.1 shows the problem facing this multi-receiver system. Due to substrate coupling of different receive LO frequencies, this oscillator has developed a spur close to the Tx frequency. The frequency of the spur can be given by the expression

$$f_{spur} = nf_a + mf_b \tag{4.1}$$

where f_a and f_b are two frequencies inside the synthesizer (two different receive frequencies) and

$$|n| + |m| = k \tag{4.2}$$

where k is the order of the nonlinearity which has led to the inadvertent mixing of the two oscillators. A nonlinearity of order $k+2i$ where i is zero or any positive integer; can also create a spur at the same frequency. The spur amplitude produced by the nonlinearity will be proportional to

$$A^{|n|}B^{|m|}(A^2+B^2)^i \tag{4.3}$$

where A is the amplitude of LO having frequency f_a and B is the amplitude associated with LO of frequency f_b.

The spur at frequency f_{spur} and amplitude proportional to (4.3) can down-convert the residual Tx leakage coming out of the duplexer. This will act an in-band interference to the received signal and degrade the SINR ratio. This degradation in SINR is the problem addressed by this work. We next determine what impacts the total amount of interference coming into the receiver bandwidth, and the proposed solution to mitigate this effect.

Let N_{Tx} be the transmit signal power spectral density in dBc/Hz and ΔR be the rejection of the duplexer at the transmit signal frequency. The residual Tx leakage out of the duplexer gets down-converted by the spur at frequency f_{spur}. The total power of the leakage at the input to the LNA, designated as S_{Tx_Leak1} will be given by

$$S_{Tx\_Leak1}\Big|_{@LNA\_Input} = N_{Tx} + 10\log(BW_{Tx}) - \Delta R \tag{4.4}$$

This leakage power is down-converted as an interference to the base-band by the spur present close to the Tx frequency. The Tx leakage power at the output of down-conversion mixer will be given by

$$S_{Tx\_Leak2}\Big|_{@Mixer\_Output} = N_{Tx} + 10\log(BW_{Tx}) - \Delta R + L_{spur} \tag{4.5}$$

where L_{spur} is the amplitude of the LO. The signal representing this leakage power is referred to as u^+ in Figure 4.1. This signal is acted on by the receive filter $H(\omega)$ shown in Figure 4.1. The receive filter selects the components within the receiver bandwidth, and hence leads to an attenuation of interference components. Assuming that $H(\omega)$ has a perfect brick-wall filter response in its pass-band, we can write the Tx leakage power at the output of receive filter as

$$S_{Tx\_Leak3}\Big|_{@RxFilter\_out} = N_{Tx} + 10\log(BW_{Tx}) - \Delta R + L_{spur} - 10\log(BW_{Rx} - BW_{Tx} - \Delta_{Tx-Spur}) \tag{4.6}$$

where $\Delta_{Tx-Spur} = f_{Tx} - f_{spur}$ .The expression (4.6) comes out of the effective bandwidth over which the Tx interference is corrupting the Rx signal. We see that the Tx leakage power is determined by the rejection offered by the duplexer, the strength of the spur tone, the difference in the Tx and spur frequency as well as the effective bandwidth of transmitter and receiver front-ends. This can be intuitively understood by the interference potential diagram in Figure 4.2.

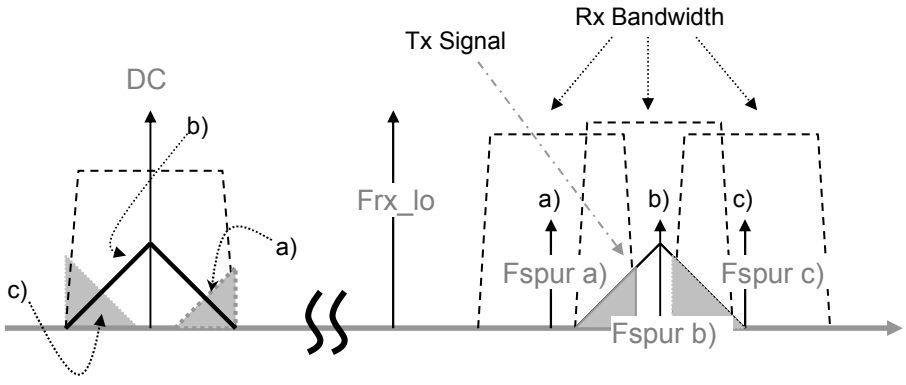

Figure 4.2. The location of spur and its interference potential

Figure 4.2 shows the base-band spectra on the left and the pass-band receiver LO and spur frequencies on the right. It shows three different locations a), b) and c) for the spur frequency. Each location of spur results in a different portion of transmit signal being down-converted to base-band and resulting in interference within the receive bandwidth. We see that spur b) can cause the highest amount of interference to the received signal because it brings all the Tx signal within the Rx bandwidth leading to the highest value of leakage in eq 4.6. Figure 4.2 assumes equal Rx and Tx bandwidths. The portion of Tx interference which falls in-band and is finally selected by the receive base-band filter is referred to as u^{++} in Figure 4.1.

4.2 Compensator for spurious receivers

As shown in Figure 4.1, the Tx signal leaking through the duplexer acts as an interference to the received signal v. The portion of Tx signal acting as an interference within the receive bandwidth is referred to as u^{++}. The compensator shown as a 'proposed system' block in Figure 4.1, attempts to reconstruct this interference by mimicking the transceiver front-end. The output of the proposed system block is shown as $\hat{u}^{++}$. The proposed system output is subtracted from the composite received signal which leads to the cancellation of interference, resulting in improved SINR for the received signal v.

4.2.1 system derivation

Next we are going to discuss the realization of this proposed block, which can accurately predict the transmitter interference, and synthesize an accurate replica of it. For the purpose of discussion ahead, let $u(t)$ and $m(t)$ represent the continuous-time,

complex base-band versions of Tx and Rx signal respectively. Let the composite signal available at the output of receive filter be z, which can be written as a summation of true received signal $m(t)$ and the residual portion of Tx interference called $u^{++}(t)$. The expression can be given by

$$Z(\omega)=H(\omega)[\delta(\omega-\omega_{Rx})*M(\omega-\omega_{Rx})+\delta(\omega-\omega_{spur})*G(\omega)U(\omega-\omega_{Tx})] \tag{4.7}$$

where $M(\omega)$, $U(\omega)$ are the frequency domain versions of received signal $m(t)$ and transmit signal $u(t)$ respectively. The portion of received signal caused by Tx interference can be written as

$$U^{++}(\omega)=H(\omega)\left[\delta\left(\omega-\omega_{spur}\right)*G(\omega)U(\omega-\omega_{Tx})\right] \tag{4.8}$$

which shows the down-conversion of the Tx signal using a spur and subsequent receive filtering of the spectrum. We can write a time domain version of the same expression, in which we explicitly show the sequence of linear and nonlinear operations on the input signal.

$$u^{++}(t)=\underbrace{h(t)}_{\text{Linear}}*\underbrace{[e^{-j\omega_{spur}t}}_{\text{Nonlinear}}\{\underbrace{g(t)}_{\text{Linear}}*\underbrace{[e^{j\omega_{Tx}t}u(t)]}_{\text{Nonlinear}}\}] \tag{4.9}$$

where $h(t)$ is the equivalent impulse response of $H(\omega)$ which is the receive filter, and $g(t)$ is the equivalent impulse response of $G(\omega)$ which is the response of the duplexer filter. The sequential operation of $G(\omega)$, down conversion with spur frequency, and operation of receive filer $H(\omega)$ is pictorially illustrated in Figure 4.3 which shows the two cases with high side and low side spurs. Figure 4.3 helps in understanding of the spectral picture, which can lead to the design of effective estimators for u^{++}.

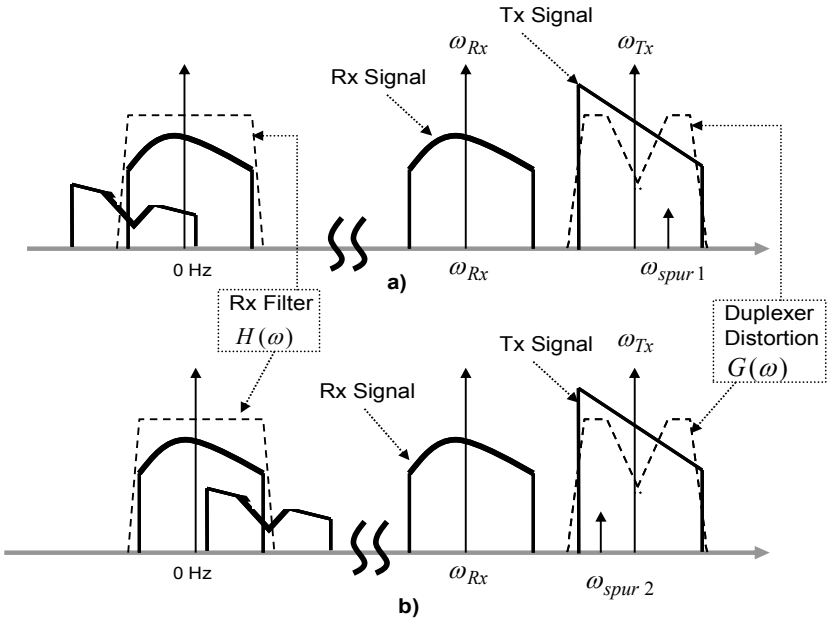

Figure 4.3 The creation of transmit signal interference at base-band

It is important to note that eq 4.9 represents a set of linear and nonlinear operations in succession which cannot be re-ordered. (4.9) can be re-written by introducing a multiplication of unity after convolution with $g(t)$

$$u^{++}(t) = h(t) * [e^{-j\omega_{spur}t} \frac{e^{-j\omega_{Tx}t}}{e^{-j\omega_{Tx}t}} g(t) * [e^{j\omega_{Tx}t} u(t)]] \tag{4.10}$$

which becomes

$$u^{++}(t) = h(t) * [e^{-j(\omega_{spur}-\omega_{Tx})t} e^{-j\omega_{Tx}t} g(t) * [e^{j\omega_{Tx}t} u(t)]] \tag{4.11}$$

we can now perform the convolution as a product in the frequency domain by writing,

$$u^{++}(t) = h(t) * [e^{-j(\omega_{\Delta})t} e^{-j\omega_{Tx}t} \mathbf{F}^{-1}[G(\omega)U(\omega-\omega_{Tx})]] \tag{4.12}$$

where the difference between the transmit frequency and the spur frequency has been called ω_{Δ}.We can allow the down-conversion operator $e^{-j\omega_{Tx}t}$ in (4.12) to translate the terms inside the brackets to its equivalent base-band form and write

$$u^{++}(t) = h(t) * [e^{-j(\omega_\Delta)t} \mathbf{F}^{-1}(D(\omega)U(\omega))] \tag{4.13}$$

where $d(t) = e^{-j\omega_{Tx}t}.g(t)$ is the equivalent base-band response of the duplexer shaping filter, which is being applied to the base-band waveform $u(t)$. Since linear operators can commute, we can write (4.13) as

$$u^{++}(t) = [h(t) * e^{-j(\omega_\Delta)t} u(t)] * d(t)] \tag{4.14}$$

Equation (4.14) gives the expression for continuous time transmitter interference reaching the receiver for subsequent base-band processing. Additionally all terms in (4.14) are equivalent base-band representations. We can therefore use this expression to build a nonlinear estimator for $u^{++}(t)$.

4.2.2 Adaptive estimation system

The equivalent base-band estimator can be written by neglecting the convolution with the term $d(t)$ on the right of (4.14) , taking the remaining expression and writing a discrete time version of that which we refer to as x_{NL}, we can write,

$$x_{NL}(n) = [h(n) * e^{-j\phi_k n} u(n)] \tag{4.15}$$

where ϕ_k is the discrete time frequency given by the ratio of ω_Δ to the sampling frequency ω_S of the ADC/DAC in the transceiver system. The convolution with $d(t)$ can be represented as a dot product of a delayed x_{NL} vector and an unknown impulse response of the duplexer filter. The estimate of u^{++} can therefore be written as

$$\widehat{u}^{++} = X_N \mathbf{w}_N^T \tag{4.16}$$

where $X_N = [x_{NL}(n)\, x_{NL}(n-1).....x_{NL}(n-N)]$ and $\mathbf{w}_N$ is a weight vector of length N which represents the discretized version of the impulse response of $d(t)$. The optimal weight vector can be determined using normal equations, which give

$$\mathbf{w}_N = R_{XX}^{-1} p_{Xz} \tag{4.17}$$

where R_{XX} is the correlation matrix for vector X_N and p_{Xz} is the cross-correlation vector between X_N and z. For an online algorithm, the estimate of $\mathbf{w}_N$ has to be computed recursively. Both LMS and RLS algorithms can be used for this recursion. We initially use RLS algorithm based on the least squares criterion to adapt the weights, but later show the comparison between the two methods as well, to highlight the tradeoff in computational load and speed of convergence. The RLS recursion can be performed by using the X vector, along with the signal z coming into the receiver. The recursion can be initialized using $S(-1) = \delta(I)$, where S is the estimate of inverse autocorrelation matrix of X_N and δ is a small positive constant. Thereafter the updates proceeds as given in (4.18)-(4.21)

$$e(n) = z(n) - X_N^T(n)\mathbf{w}(n-1) \tag{4.18}$$

$$\psi(n) = S(k-1)X_N(n) \tag{4.19}$$

$$S(n) = \frac{1}{\lambda}[S(n-1) - \frac{\psi(n)\psi^T(n)}{\lambda + \psi^T(n)X_v}] \tag{4.20}$$

$$\mathbf{w}_N(n) = \mathbf{w}_N(n-1) + e(n)S(n)X_N(n) \tag{4.21}$$

where λ is a forgetting factor having values from 0 to 1. The architecture of the estimator is shown in Figure 4.4, where a transmit signal u is used to create the interference u^{++} coming into the receiver. The RLS algorithm is used to operate on the error and adapt

the weights of the filter approximating the duplexer response. The output of the canceller consists of the actual received signal plus the estimation error. If the adaptive filter has estimated the interference well, the cancellation residual would be very small, and the received signal SNR would be improved. The forgetting factor can be increased to reduce the steady state mean square error of the system and lead to optimal received signal SNR.

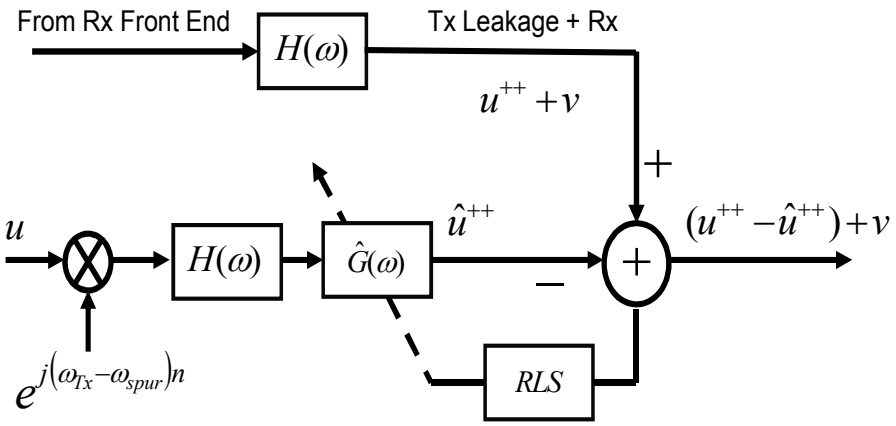

Figure 4.4 Signal flow for estimation of Tx interference

4.2.3 Duplexer response characterization

In order to perform realistic system simulations of the above scheme, we captured the frequency response of an actual duplexer in the lab. The VNA captured S-parameters were used to plot the S21 response of the duplexer from Tx to Rx port. The results are shown in Figure 4.5 over a frequency range of 15 MHz. Using the actual duplexer response, a 32 order IIR filter was used to fit the to the measured magnitude and phase response of the duplexer. Figure 4.5 shows the result as a second trace. We observe that duplexer stop-band consists of large notches which create a frequency response over the residual transmitter leakage. The depth of the notched regions could be as high as 20 dB,

over a bandwidth of ~ 2MHz. We are primarily interested in running the system over a CDMA chipset with a chip rate of 1.2288 MHz. Therefore the channel bandwidth of 2 MHz is relevant for the study of duplexer system

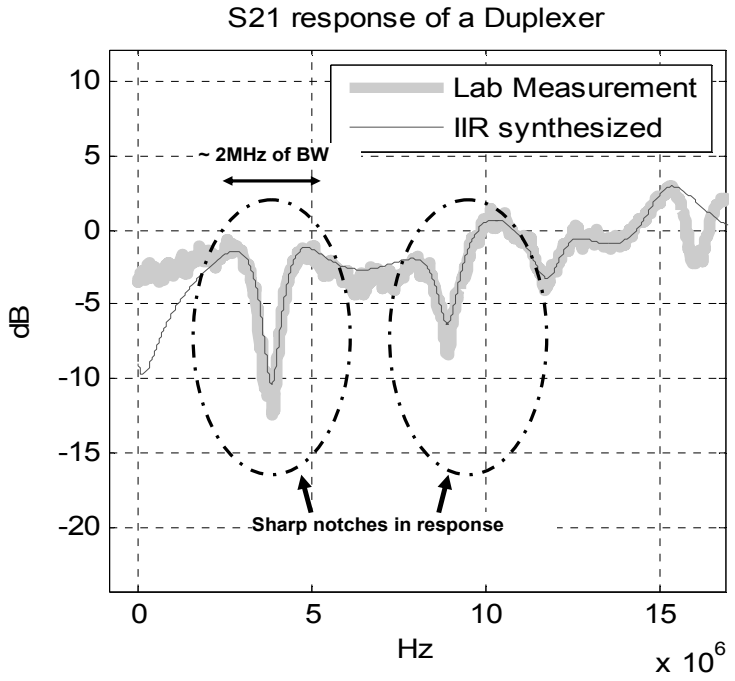

Figure 4.5. Lab characterized Duplexer

Figure 4.6 shows the frequency domain response of a simple FIR filter, having 5 taps, operating over the sampling rate of Chipx8 i-e 9.83 MHz. The filter taps are selected to generate a notch-like response. The taps used are $h_{FIR} = \begin{bmatrix} 1 & 0 & 1 & 1 \end{bmatrix}$, which lead to the presence of a notch at the zero frequency. The frequency response has been highlighted to show the presence of a sharp notch, which produce 15-20 dB of attenuation over a bandwidth span of nearly 2 MHz. Such a filter is remarkably successfully in regenerating the notches found in the circular-marked regions of duplexer response Figure 4.5. From the frequency response of such a filter, we gather that FIR filters with few taps are able to mimic a sharp notch in the spectral response. Since such notches are prevalent in the duplexer frequency response, we can use these FIR structures to model the duplexer.

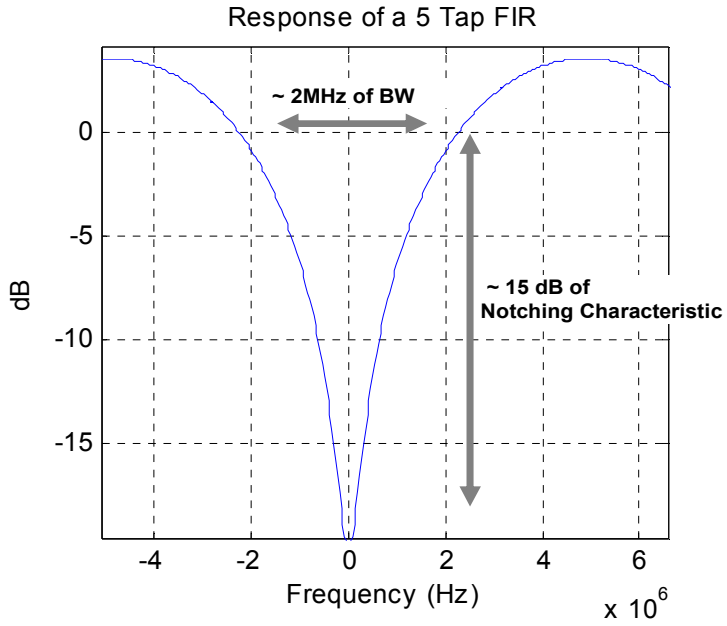

Figure 4.6. Simulating duplexer notches using 5 Tap FIR

4.3 Synthesizer spurs in actual RFICs

The compensation architecture discussed in the previous section will work well for purely complex spurs which can perform perfect down-conversion of the Tx leakage signal. When the spurs were captured in the lab, they showed a degree of imbalance associated with them. This complicates matters, as perfect down-conversion is no longer guaranteed.

4.3.1 Problem of Imbalanced Spurs

In order to understand the problem, lets remind ourselves that the signal $u(t)$ referred to as the original transmit signal in Section 4.2 is actually an analytic signal or complex base-band signal which consists of both in-phase and quadrature components $u(t) = u_I(t) + ju_Q(t)$. The band-pass version of the signal is constructed from translation of the signal and it conjugate to positive and negative carrier frequencies resulting in

$$[u_I(t) + ju_Q(t)]e^{+j\omega_c t} + [u_I(t) - ju_Q(t)]e^{-j\omega_c t} \tag{4.22}$$

$$u_I(t)\cos(\omega_c t) + u_Q(t)\sin(\omega_c t) \tag{4.23}$$

which is recognized as the modulated version of a complex baseband analytic signal. Fig 4.7 part a) shows the modulated transmitter signal. Part b) shows a complex spur located at the frequency $-\omega_{spur}$ which is made to be the same as $-\omega_c$.

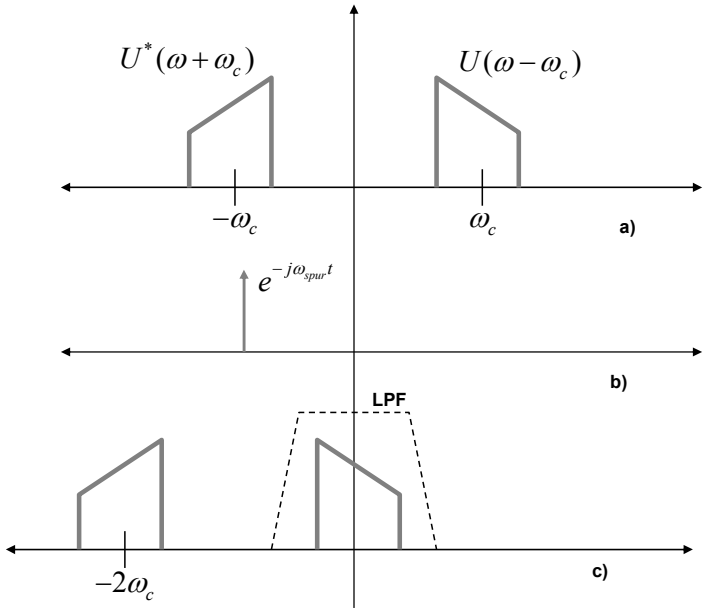

Figure 4.7. Demodulation with purely complex spur

This spur leads to the down-conversion of the transmit signal resulting in the spectra shown in part c). A low pass filter can pick out the spectral replica at the zero frequency and leads to the recovery of baseband signal. The down-conversion process can be represented by a the set of eqs (24-25).

$$\{[u_I(t) + ju_Q(t)]e^{+j\omega_c t} + [u_I(t) - ju_Q(t)]e^{-j\omega_c t}\}e^{-j\omega_c t} \tag{4.24}$$

$$[u_I(t) + ju_Q(t)] + [u_I(t) - ju_Q(t)]e^{-2j\omega_c t} \tag{4.25}$$

which on application of a low pass filter shown in Figure 4.7 Part c) recovers the original base-band signal. On the contrary, the signal being demodulated with a real-world imperfect spur is shown in Figure 4.8.

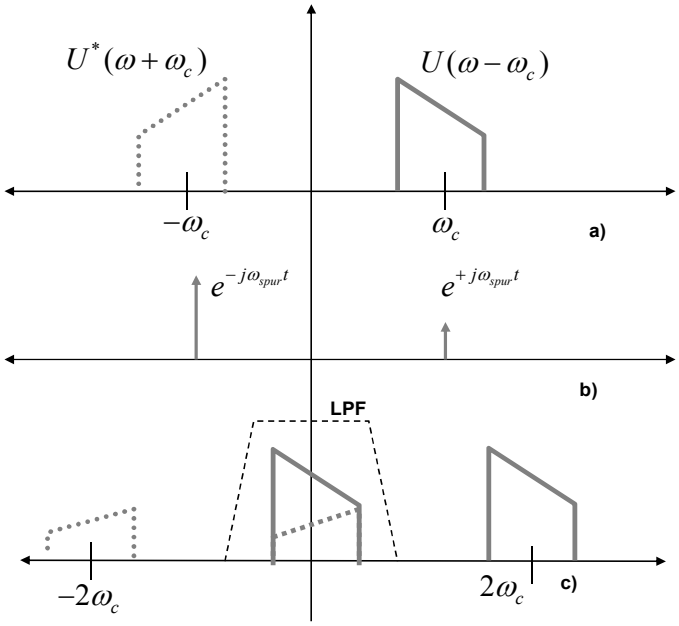

Figure 4.8. Demodulation with imbalanced spur

The spur with an imbalance has a contribution from the positive exponential. In mathematical terms, the imbalanced spur would have a representation given by

$$Spur_{imbalanced} = \cos(\omega_c t) + \beta \sin(\omega_c t + \theta) \qquad (4.26)$$

where β and θ represent the magnitude and phase imbalance respectively. The imbalanced spur will lead to the down-conversion of both the positive and negative frequency components to the baseband as shown in Figure 4.8, which shows the negative frequency image of the signal in dotted line. The negative frequency image is a conjugate version of the original signal and gets added to the original transmit signal at the baseband frequencies. If the spur is of the form represented in (4.26) our estimator would

no longer give an accurate reconstruction of the interference, because the interference is now comprised of super-imposed components from the negative and positive frequency images of the signal.

4.3.2 Modified compensator for imbalanced spurs

In order to circumvent this problem, a revised estimator is formulated. Given that the original signal is $u(t)$ we can write the down-conversion with imbalanced spur as follows,

$$u(t)\big|_{Modulated} \times Spur_{imbalanced} = [u(t)e^{+j\omega_c t} + u^*(t)e^{-j\omega_c t}][\cos(\omega_c t) + \beta \sin(\omega_c t + \theta)] \quad (4.27)$$

The down-converted signal is filtered before further processing. Hence we apply a low pass filter to the product in (4.27) as shown in Fig 4.7 & 4.8. We therefore, first expand the product in (27) and then apply a low-pass filter to the resulting waveforms. (27) can be written as a sum of two products associated with $u(t)$ and $u^*(t)$ respectively yielding,

$$u(t)\big|_{Modulated} \times Spur_{imbalanced} = \gamma_1 u(t) + \gamma_2 u^*(t) \quad (4.28)$$

where γ_1 and γ_2 can be obtained by expanding (27) further. We perform and show this expansion for γ_1 and it would be an identical procedure for γ_2

Using Euler's formula for the exponential terms, we can write γ_1 as

$$\gamma_1 = [\cos(\omega_c t) + j \sin(\omega_c t)][\cos((\omega_c t) - j\beta \sin(\omega_c t + \theta))] \quad (4.29)$$

Expanding (29) we can write

$$\begin{aligned} \gamma_1 = \cos(\omega_c t)[\cos(\omega_c t) - j\beta \sin(\omega_c t + \theta)] + \\ j \sin(\omega_c t)[\cos(\omega_c t) - j\beta \sin(\omega_c t + \theta)] \end{aligned} \quad (4.30)$$

which on further expansion yields

$$\gamma_1 = \frac{1}{2} + \frac{\cos(2\omega_c t)}{2} - j\beta\left[\frac{\sin(2\omega_c t)}{2} + \frac{\sin\theta}{2}\right] + j\left[\frac{\sin(2\omega_c t)}{2} + \frac{\sin 0}{2}\right] + \beta\left[\frac{\cos(\theta)}{2} + \frac{\cos(2\omega_c t + \theta)}{2}\right] \tag{4.31}$$

upon elimination of high frequency terms we are left with

$$LPF[\gamma_1] = \frac{1}{2} + \frac{\beta}{2}\cos(\theta) - j\frac{\beta}{2}\sin(\theta) \tag{4.32}$$

which finally yields

$$LPF[\gamma_1] = \frac{1}{2}\left[1 - \beta e^{j\theta}\right] \tag{4.33}$$

Performing similar operations on γ_2 yields

$$LPF[\gamma_2] = \frac{1}{2}\left[1 + \beta e^{-j\theta}\right] \tag{4.34}$$

which shows that the coefficients of (4.28) can be completely expressed using the imbalance parameters. If these imbalance parameters are known, one can calculate the value of coefficients required to compute an estimate of transmit interference. In practice however, the imbalance coefficients would never be known exactly and may change on the fly during the operation of the transceiver. We therefore propose to estimate these coefficients adaptively as detailed out in the next section.

4.3.3 Adaptive estimation and cancellation system

From the last section, we conclude that down-conversion resulting from imbalanced spurs can be a superposition of an analytical signal and its complex conjugate image. We can therefore modify the discrete time estimator of (4.15) and (4.16) by writing,

$$\hat{u}^{++}(n) = \gamma_1^{LPF}\{\mathbf{w}^T.[h(n) * e^{-j\theta_k n}u(n)] + \gamma_2^{LPF}\mathbf{w}^T.[h(n) * e^{-j\theta_k n}u(n)]\}^* \tag{4.35}$$

where the dot product with $\mathbf{w}^T$ represents convolution with the estimate of the channel response and γ_1^{LPF} and γ_2^{LPF} represent the low-passed versions of the coefficients γ_1 and γ_2 in (4.28). The estimate $\hat{u}^{++}(n)$ can be formed by two step processing on the input vector $X_N = [x_{NL}(n)\ x_{NL}(n-1).....x_{NL}(n-N)]$ where x_{NL} is the same as defined in eq 4.15. We can write the two step processing by defining the intermediate signals as follows

$$x_{NL}(n) = [h(n) * e^{-j\phi_k n} u(n)] \tag{4.36}$$

$$x_{LNL}(n) = \mathbf{w}^T . [X_N] \tag{4.37}$$

$$\hat{u}^{++}(n) = [\gamma_1^{LPF} \quad \gamma_2^{LPF}] \begin{bmatrix} x_{LNL}(n) \\ x_{LNL}^*(n) \end{bmatrix} \tag{4.38}$$

There are two updates for the adaptive coefficients. We form an error signal using the output of the receiver and the estimate of the transmitter interference. The error signal is given by

$$e = v(n) + noise + [u^{++}(n) - \hat{u}^{++}(n)] \tag{4.39}$$

where $v(n)$ is the signal received at the antenna and $noise$ is the AWGN noise present in the signal. The error signal e is fed to recursive least squares adaptive update algorithm which updates the following two set of weights as follows

$$\mathbf{w}_N(n) = \mathbf{w}_N(n-1) + e(n) S_\alpha(n) X_N(n) \tag{4.40}$$

where S_α refers to the kalman gain vector of the first RLS algorithm, which can be computed using relations (4.19)-(4.20). Similarly the coefficients for the original and image signals can be computed adaptively using the update,

$$\begin{bmatrix} \gamma_1^{LPF}(n) \\ \gamma_2^{LPF}(n) \end{bmatrix} = \begin{bmatrix} \gamma_1^{LPF}(n-1) \\ \gamma_2^{LPF}(n-1) \end{bmatrix} + e(n) S_\beta \begin{bmatrix} x_{LNL}(n) \\ x_{LNL}^*(n) \end{bmatrix} \tag{4.41}$$

where S_β is the kalman gain vector of the second RLS algorithm using the vector $\left[x_{LNL}(n) \quad x^*_{LNL}(n)\right]$ as input. The new architecture for cancellation in the presence of imbalanced spurs is shown in Figure 4.9.

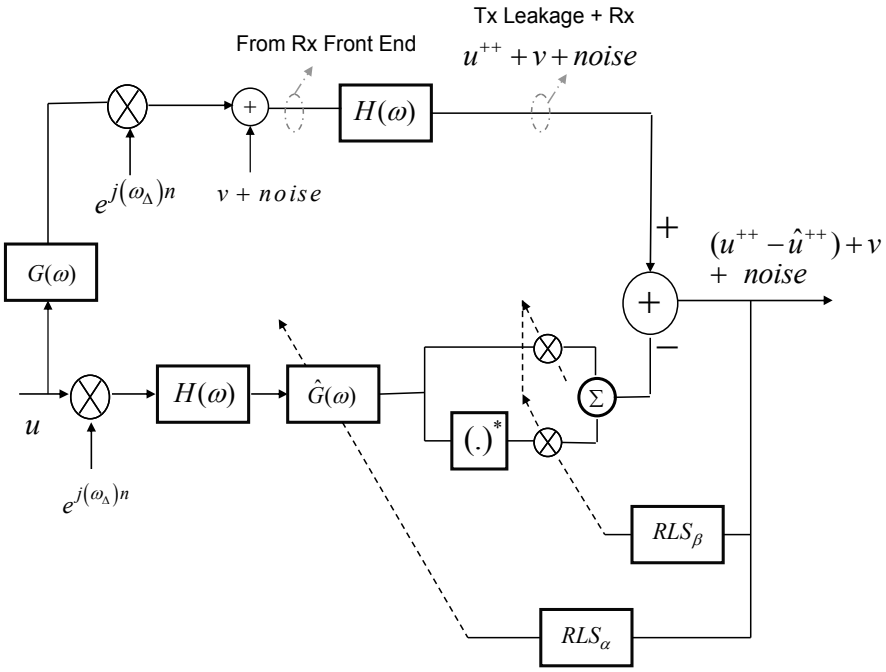

Figure 4.9. Compensation architecture for imbalanced spurs

Fig 4.9 has taken after Figure 4.4, but it also shows the base-band equivalent version of receiver front-end which generates the transmit interference. The signal u at the bottom left corner of the figure, is the transmit base-band signal. This encounters the duplexer response $G(\omega)$ going upwards, and is frequency shifted by the demodulating spur with the frequency $\Delta\omega$ as shown in the figure. To the frequency shifted version of the transmit signal, we add the received signal and pass the composite signal through the receive low-pass filter.

While the top half of Figure 4.9 represents the system encountered by the transmit signal in a real RFIC, the bottom half represents the internal signal processing being performed

on the transmitted signal to create an estimate of transmit signal interference being received by the receiver. The signal u is first frequency shifted to create the nonlinear transformation as shown in Section 4.2. The signal is then filtered using the receive filter, and is subsequently fed to an adaptive filter being tuned to match the frequency response of the duplexer. The output of the adaptive filter is split into two parallel streams, one of which is conjugated to create the effect of image signal. The signal and its conjugate image is multiplied with a two tap filter to create an estimate of the transmit interference. Once the estimate is subtracted from the composite received signal at the top of Figure 4.9, we are left with the actual received signal and the residual of cancellation. This error signal is used to adapt the weights of two separate RLS blocks, referred to as RLS_α and RLS_β in the figure. The adaptive tuning of the channel estimator weights, and the imbalance equalization weights, leads to a system which is able to reconstruct the transmit interference even in the presence of strongly imbalanced spurs. We will demonstrate the superior performance of such a system in the simulation results in the next section.

4.4 System validation using lab characterized duplexer

Using the setup shown in Figure 4.9, we can perform system validation by implementing the discrete time base-band equivalent version, and the measured duplexer response shown in Figure 4.5. A CDMA modulated transmit signal with a bandwidth of 2 MHz is used as the input signal to the system. The strength of transmit and received signal can be varied to test different performance limits of the proposed cancellation system.

4.4.1 Performance metrics

We benchmark performance on the basis of three different performance metrics. The first described as Tx MSE or –MSE, is expressed in terms of quantities from Figure 4.4 or Figure 4.9 as follows,

$$Tx\_MSE_{dB} = -1 \times 10 \log_{10} \frac{E[(u^{++} - \hat{u}^{++})^2]}{E[(u^{++})^2]} \tag{4.42}$$

This metric describes the accuracy with which the system is able to predict the transmit interference u^{++}. Therefore its referred to as Tx mean square error (Tx_MSE). The multiplication with -1 ensures that this is a positive number, and the higher value of this number represents greater prediction accuracy. The other two metrics are used in combination to represent the received signal recovery performance of the system. The first called Rx SNR pre IC represent the degradation of received signal SNR with the increase in the level of transmit interference. This can be expressed as

$$RxSNR_{dB,\mathrm{Pre}IC} = 10 \log_{10} \frac{E[(v)^2]}{E[(u^{++} + v + noise)^2]} \tag{4.43}$$

where the received signal v represents the desired signal in the numerator, and the sum of received signal, transmit interference and noise represents the corrupted version in the denominator. This pre-interference-cancellation SNR will decrease with the increase in the level of interference. Once the signal is cleaned using the proposed scheme, we represent the resulting SNR as post interference cancellation, and write it as

$$RxSNR_{dB,PostIC} = 10 \log_{10} \frac{E[(v)^2]}{E[(u^{++} - \hat{u}^{++} + noise)^2]} \tag{4.44}$$

The post interference cancellation SNR is limited by the cancellation residual $(u^{++} - \hat{u}^{++})$ appearing in the denominator.

4.4.2 Spectral analysis

The meaning of different performance metrics can also be illustrated on the power spectral density plot. After simulation the system we plot the different signals in the frequency domain. An example system simulation result is shown in Figure 4.10.

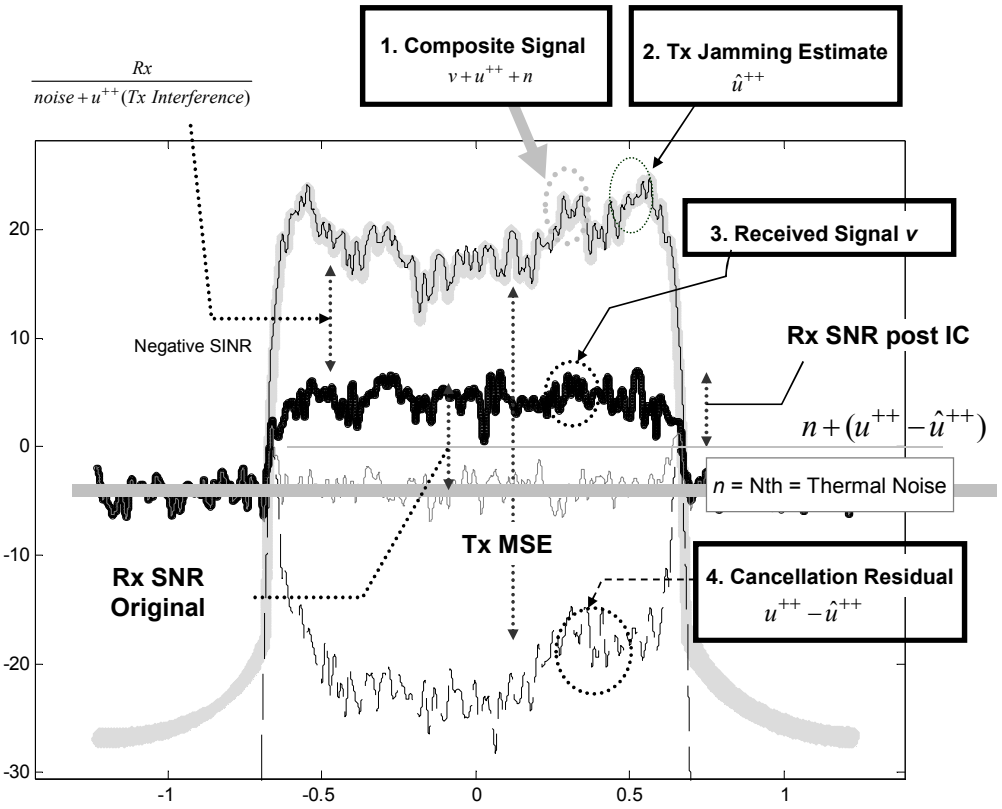

Figure 4.10. PSD signal plots and performance metrics

A strong Tx self-jamming signal of 20 dB/N_{th}(Thermal noise) was used and a weak received signal of strength 5 dB/N_{th} was added to it along with AWGN that sets the noise floor. The sum of three signals is Trace 1 at the top of Figure 4.10. The composite signal is passed through the proposed cancellation system and the estimate of Tx self-jamming signal (Trace 2) is subtracted out. The residual (Trace 4), adds to the noise floor and determines the final Rx SNR post cancellation. The figure shows 4 Traces along with

noise floor and illustrates the meaning of two performance metrics Tx MSE and Rx SNR post IC.

4.4.3 System performance under different scenarios

The performance of the system was tabulated for a variety of transceiver operating scenarios, in which various levels of Rx signal were used. A very low strength received signal scenario is shown in Figure 4.11.

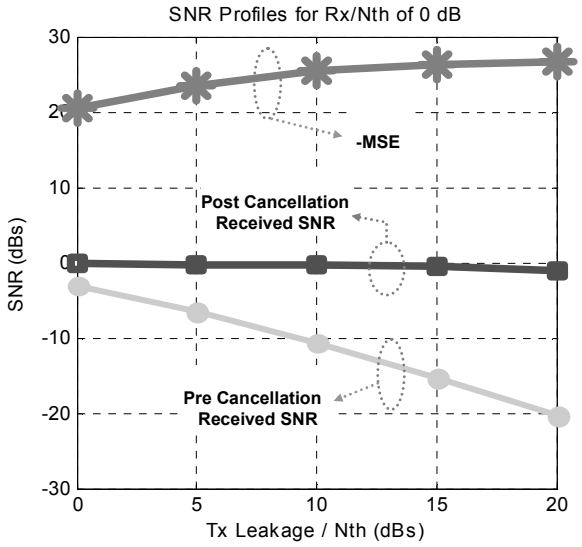

Figure 4.11. Performance metrics with Rx/Nth of 0 dB

The original strength of the received signal was 0 dB over thermal noise. The deterioration of received signal SNR with the increase in Tx interference is shown by the 'Pre Cancellation received SNR' trace in Figure 4.11. Once the compensation system is put on, the received signal SNR increases to the values shown in 'Post Cancellation received SNR' trace. We see that the SNR has been almost restored to its nominal value, except a slight degradation at very high levels of Tx interference (~ 20 dB over thermal noise). The values of Tx MSE corresponding to each power level are shown by the third trace. We see that in order to restore the received SNR, the MSE performance must

become higher with the increase in interference level. At some point, the MSE performance will be limited by the number of filter taps, and the over-sampling ratios employed in the system, after which the system will no longer be able to recover the received SNR to its nominal values.

The received signal designated as v in the diagrams and figures above, acts as a disturbance to the estimation of Tx interference. This fact may lead one to believe that the system performance will deteriorate with the increase in the level of received signal. Figure 4.12 dispels this notion by showing the system performance with a high value of received signal of 15 dB over thermal noise.

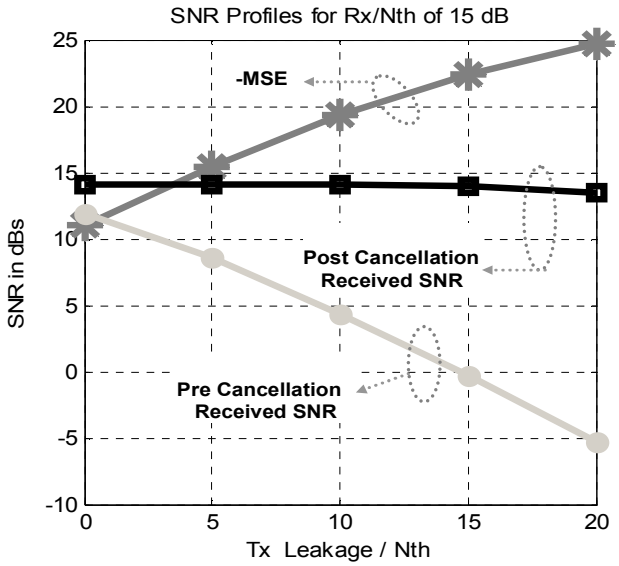

Figure 4.12. Performance metrics with high Rx/Nth of 15 dB

As Figure 4.12 shows, the system can clearly restore the SNR in this case of very high Rx/Nth. However, the restoration is not exact and the post cancellation SNR does not reach the original 15 dBs. It is restored close to ~14 dB. This loss of restoration can be ascribed to a high value of disturbance or noise within the desired signal, which leads to a

slightly higher mean square error. We observe that the negative MSE curve does not go as far as the MSE curve of the first example.

In the case of imbalanced spurs, the system is re-simulated by injecting imbalanced waveforms in place of the spur frequency exponential. The spectrum of this kind of imbalanced waveform is shown in Figure 4.13.

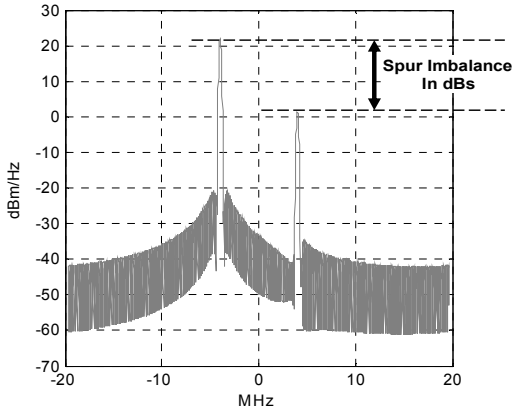

Figure 4.13 Spectral picture of imbalanced receiver spurs

We observe that positive and negative frequency impulses are imbalanced from each other. The amount of imbalance can be tuned by selecting the constants β and θ as stated in expression 4.26. The system with no compensation for imbalance is referred to as 'Single RLS', whereas the system having compensation for imbalance is called 'Dual RLS'. The results of the simulations are shown in Figure 4.14 and Figure 4.15..

The bottom most Trace (in the legend) in Figure 4.14 represents the decrease in Rx SNR with the increase in Tx Leakage, when there is 20 dB of imbalance present on the spur. We observe that the decay in Rx SNR is present even with the adaptive compensation system working. This is because the system is not taking the imbalanced spur into account. Although in this case, the decay in Rx SNR is not as steep as it happens in the

case of completely uncompensated system. So the single RLS is still offering some compensation but not enough to restore the SNR completely.

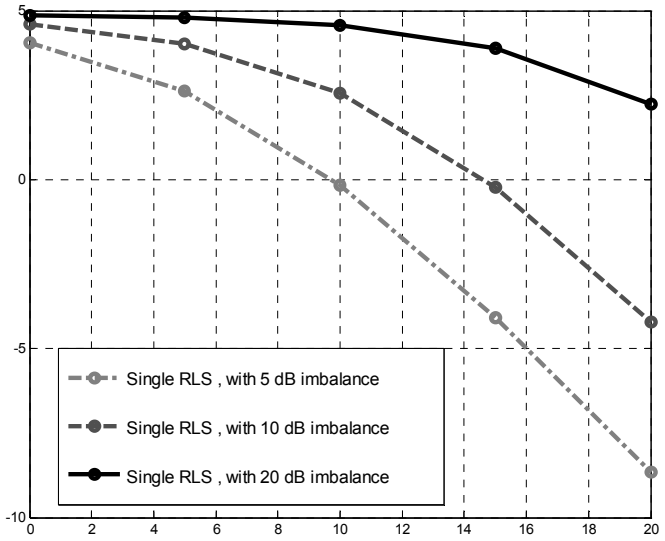

Figure 4.14. Single RLS with Imbalanced Spur for Rx/Nth = 5dB

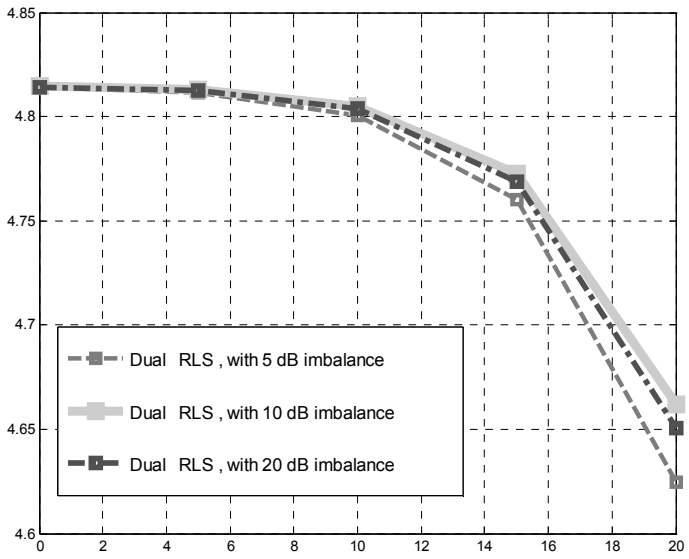

Figure 4.15. Dual RLS with Imbalanced Spur for Rx/Nth = 5dB

In order to compare with what happens in the case of using the imbalance compensated system of Figure 4.9, we look at the bottom most trace (in the legend) of Figure 4.15. We

observe that the Dual RLS system is able to restore the Rx SNR almost completely to its nominal value of 5 dB. Comparing the corresponding curves between Figure 4.14 and Figure 4.15, it can be concluded that the Dual RLS architecture is agnostic to the presence of imbalance. Whatever imbalance may be present in the spur can be compensated using this architecture.

The simulations experiments gave us enough verification to perform validation on the actual hardware. The next section details the hardware setup and the performance results achieved using that.

4.5 RF Test-Bench and measurements

The true test of the proposed compensation technique comes from measurements on actual RFIC chipsets suffering from spurious LO problem. A commercial RFIC was mounted on a test RF board. The board was provided with an interface to the baseband I/Q samples. The test-setup and the board are shown in Figure 4.16.

The transmitter and receiver were tuned to frequencies to simulate the spurious LO problem. The Tx emission down-converted by the spur was sampled and taken into the receive chain. The board containing the RFIC is fed with base-band WCDMA I/Q signals from the signal generator. Inside the RFIC, the signal is up-converted and passed through an onboard duplexer which connects to the antenna. Due to imperfect attenuation, some of the Tx leaks through the duplexer and gets down-converted by the spurious receiver LO. This becomes available at the 'Receiver I/Q out' in Figure 4.16. We add synthetic noise and received signal to this interference to create a mixture which can be given to an adaptive filter input as the desired signal referred to as z in the Figure.

A synchronizer block was used to align the baseband Tx interference estimate with the interference received from the receiver baseband.

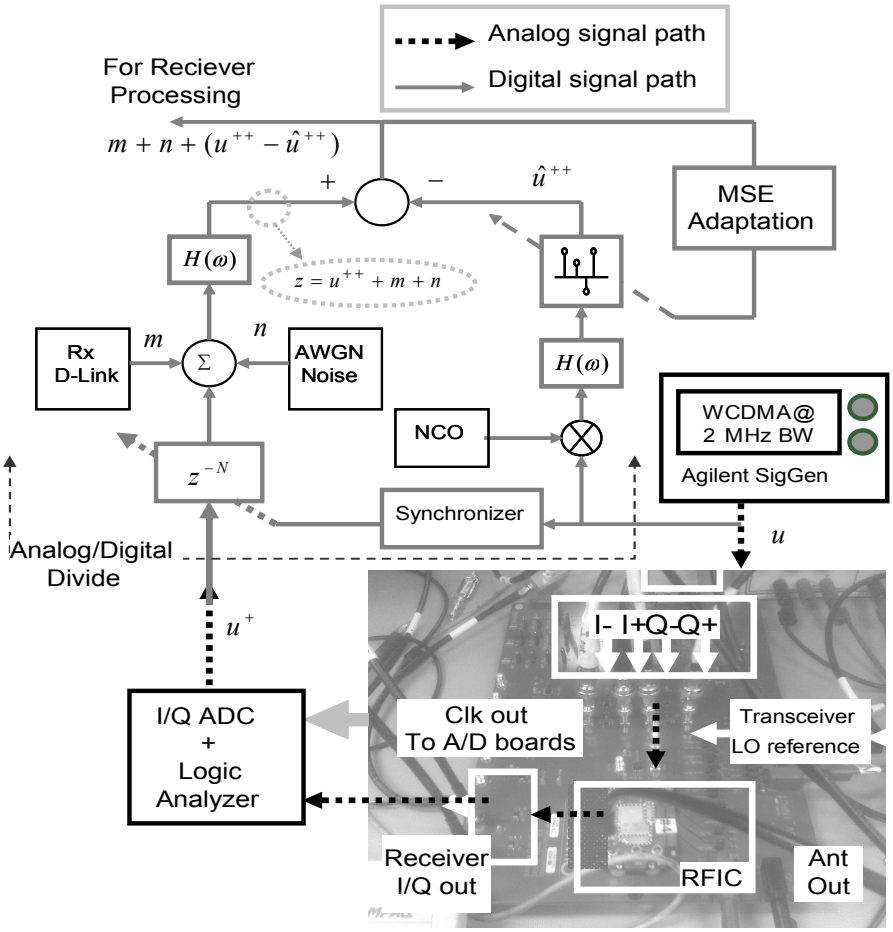

Figure 4.16. Experimental setup for validating performance

After performing the digital operations of interference predictions and cancellation, as detailed out in the sections above, we come up with the metrics for Tx MSE and Rx SNR. Results of the experiments are shown in Table 4.1 & 4.2. We take up different scenarios of Tx Leakage and Rx signal powers, and perform a particular experiment on the test-setup. The scenarios listed in the tables have been carefully selected to highlight the performance under typical and extreme operating conditions.

Scenario		**Performance**		
Tx Leakage / N_{th} (dB)	**Rx/ N_{th} (dB)**	**Rx_SNR (dB)**		
		LMS	RLS	Hybrid
0.00	0.00	-0.94	-0.23	-0.21
5.00	5.00	3.14	4.28	4.20
10.00	15.00	8.50	11.99	11.91
20.00	5.00	-1.80	-1.20	-2.01
5.00	20.00	9.71	15.12	15.01

Table 4.1 MSE performance measurement from RF test bench

Scenario		**Performance**		
Tx Leakage / N_{th} (dB)	**Rx/ N_{th} (dB)**	**Tx_MSE (dB)**		
		LMS	RLS	Hybrid
0.00	0.00	7.61	12.21	9.28
5.00	0.00	11.12	13.89	12.83
10.00	15.00	4.86	9.77	9.48
20.00	5.00	13.94	14.48	14.02
5.00	20.00	-4.2	1.80	1.92

Table 4.2 Rx SNR performance measurement from RF test bench

In order to provide a comparison between different adaptive algorithms, we perform adaptive update of the weight using LMS and RLS algorithm. Along with these two, we also include a tuning algorithm which is called 'Hybrid' in the table. This refers to the method in which the filter response is learned using LMS whereas imbalance coefficients are learned using RLS method. This method was implemented to cut on the complexity of RLS adaptation, while allowing faster convergence of the imbalance coefficients.

Row 3 in Table I shows that in the event of a high Tx Leakage of 20 dB above the noise, the proposed system can offer ~13-14 dB of MSE, hence attenuating the interference causing signal from 20 dB to just 6 dB. Row 3 in Table III shows that if the interference is attenuated to 6dB, the received signal SINR can be boasted, from its original level of -15 dB to -2 dB. This is an extreme case of interference, and even in such a situation, the system gives good performance. For low interference scenarios, as shown in row 3&5 of the tables, the interference cancellation advantage can be substantial. Comparing the last three columns from both the tables tells us that the hybrid method of adaptation is a good compromise between the complexity and performance of RLS and LMS methods.

Conclusion

With the increase in the number of radios per platform, the RFIC has to have to encapsulate increasing complexity of synthesizers for accommodating all the receive signal paths on chip. This synthesizer complexity necessarily entails a large number of spurs. If left unattended, a spur can have disastrous consequences for the received signal. Till now, the only method of combating spurs is with additional filtering, or pruning the

channel combinations to exclude those that lead to spurs. This chapter has proposed a different method of combating spurs, by using digital assistance between the transmitter and receiver path. By modeling the spur generation, and subsequent Tx down-conversion process, one can come up with an estimate of interference caused by the spur and cancel it at the receiver. We have shown that adaptive filtering theory can be used to construct an online model of the spur induced jamming process and tune the parameters for optimal cancellation. The system has been simulated and then experiments have been conducting by prototyping with an actual RFIC. By using different transmission scenarios and testing them on our setup, we have shown that significant performance boost is possible by using the proposed technique.

Chapter 5

Coexistence with Excess Noise

The evolution of efficiency in RF power amplifiers has been very gradual. Even today, they dissipate a lot of energy as heat which reduces the efficiency and increases the noise level. This PA noise is generally attenuated down to the thermal noise floor of the receiver by using highly selective duplexers. High selectivity necessarily carries high insertion loss and hence the PA output power requirement further increases. In the next generation of radios, efforts are underway to substantially reduce duplexer size and selectivity specifications. This will lead to a significant increase in the PA noise falling into the receive band. This chapter looks at a new technique to mitigate this receive-band noise by means of a mixed signal architecture using analog and digital components. We demonstrate that the cancellation of this noise can be accomplished by the receiver, and SNR gains can be demonstrated using commercial RFICs. By using this noise cancellation technique we allow difference radios to co-exist in the presence of such noisy transmitters.

5.1 Rx Band noise problem

Duplexers happen to be the most area occupying components in the radio front-end [34][35]. They increase cost and size of the transceiver system as well as decrease its flexibility to support various radio band configurations [37]. Efforts have long been underway to reduce or eliminate the SAW duplexers [33][41]. One of the major issues in removing the Tx-Filter component of the Duplexer, is that of receive band noise [48]. The noise generated at the PA output, if it is only partially attenuated, will fall into the

receive band and degrade the receiver SNR. From here on we refer to the PA noise falling into the receiver spectrum as RxBN. The block diagram of the transceiver system and our proposed solution is shown in Figure 5.1. In a conventional transceiver, the signal from the transmitter is passed through a mixer and power amplifier on the top. The power amplifier produces inter-modulation products as well as raises the far-out noise spectrum. The portion of noise spectrum falling into the receive band (RxBN) is referred to as u^{Tx+8BW} in the figure.

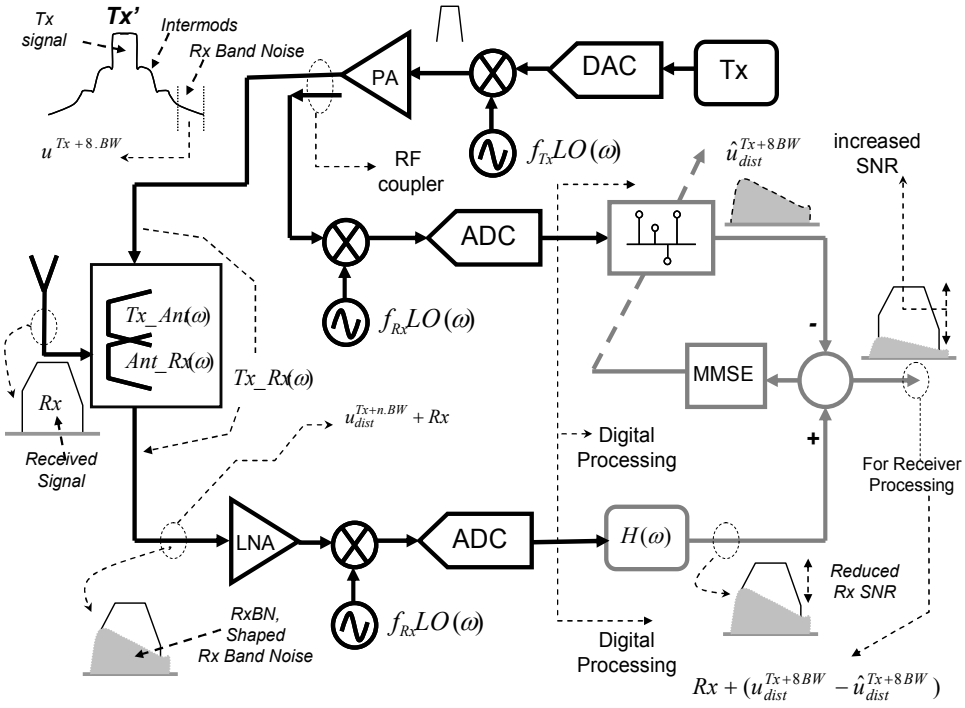

Figure 5.1. Rx Band noise problem and the proposed solution

The noise passes through a duplexer shown as a cascade of two filters $Tx\_Ant(\omega)$ and $Ant\_Rx(\omega)$. The cumulative effect of passing from the transmitter to the receiver is shown as $Tx\_Rx(\omega)$. The noise signal captured by the receiver after passing through the duplexer is referred to as u_{dist}^{Tx+8BW}. The antenna also receives the desired signal Rx which

is to be demodulated. The signal u_{dist}^{Tx+8BW} and Rx get added together and are subsequently down-converted by the receiver LO. The signal u_{dist}^{Tx+8BW} adds to the signal Rx to reduce its SNR as shown after the filter $H(\omega)$ in the lower branch of Figure 5.1.

5.2 Rx Band noise cancellation

Figure 5.1 also shows the proposed solution to address the leakage of RxBN. An auxiliary branch samples the output to sense the PA noise prior to leaking in the receiver band. This signal has the PA noise contribution embedded within it. It is down-converted to extract the portion of noise which is of interest for the receiver, and then passed through an adaptive digital chain. The purpose of the chain is to estimate the distortion incurred to the PA noise as it leaks into the receive chain.

The cancellation scheme consists of an adaptive tapped delay line filter which estimates the distorted signal u_{dist}^{Tx+8BW} coming in through the receiver. This is shown as $\hat{u}_{dist}^{Tx+8BW}$ in the figure. The estimate of interference is subtracted from the received signal, and the resulting cleaner signal consists of the received signal Rx and the residual of the estimation. For this discussion, the receiver thermal noise has been neglected but as we will see later, the actual apparatus used in lab will always have some thermal noise floor associated with it.

5.3 System design for noise cancellation

In order to demonstrate the feasibility we setup a noise cancellation scheme using existing RFIC chipsets. The basic idea is to use a diversity receiver, already present in an RFIC, to sample the PA noise signal leaking through the Tx-filter of the duplexer and utilize a DSP-based approach to estimate the frequency response of the filter and perform

noise cancellation in the digital domain. The system is illustrated in Figure 5.2 which shows the base-band equivalent model of the test setup. The filters have been replaced by their equivalent base-band representation having the subscript DC attached to it.

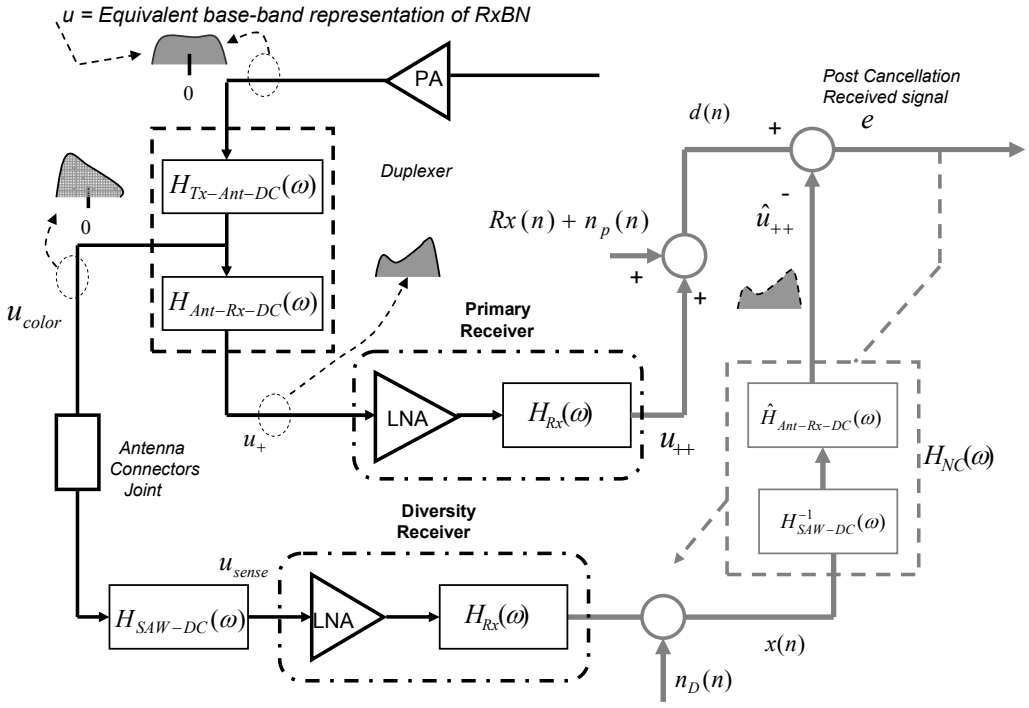

Figure 5.2. Base-band modeling of the noise problem and solution

To simplify the notation, only equivalent base-band Rx-Band noise component is shown as this is the relevant signal of interest. At the top of Figure 5.2, we show a signal u which represents the complex base-band equivalent of RxBN component falling in the receiver band. The signal is passed through a duplexer model shown as broken down into two components (inside a dashed line boundary). After passing through the duplexer sub-filter $H_{Tx-Ant-DC}$ it appears as u_{color} at the antenna output. This u_{color} is spilled to form the reference signal for the noise cancellation loop. The signal u_{color} also passes through another shaping filter $H_{Ant-Rx-DC}$ and appears at the input of primary receiver as u_+.

Assuming that LNA causes no significant distortion to the received signal, we can write the resulting signal at the output of primary receiver as

$$U_{++}(\omega) = H_{Rx}(\omega)H_{Ant-Rx-DC}(\omega)U_{color} \tag{5.1}$$

To this signal we add a received signal $Rx(n)$ which represents the desired signal input at the antenna. The signal u_{color} is also routed to a diversity receiver, by connecting the respective antennas of primary and diversity receivers. The signal passes through SAW filter of the diversity receiver $H_{SAW}(\omega)$ and the receiver filter $H_{Rx}(\omega)$ to appear at the output of diversity receiver. Let the signal be called $x(n)$ at this point and it would be given by

$$X(\omega) = H_{Rx}(\omega)H_{SAW-DC}(\omega)U_{color} + N_D(\omega) \tag{5.2}$$

This digital signal is passed through an extra digital path, as proposed in Figure 5.1. Let $H_{NC}(\omega)$ be the response of the adaptive filter in the diversity path, and let its output be designated by $\hat{u}_{++}$. The adaptive loop will try to force the NC filter output to be as correlated as possible with the RxBN observed in the primary path. If no disturbance was present i-e $Rx(n) = n_p(n) = 0$, then

$$H_{SAW-DC}(\omega)H_{Rx}(\omega)H_{NC}(\omega) = H_{Ant-Rx}(\omega)H_{Rx}(\omega) \tag{5.3}$$

from which the response of the filter $H_{NC}(\omega)$ is given by

$$H_{NC}(\omega) = \hat{H}^{-1}_{SAW-DC}(\omega)\hat{H}_{Ant-Rx-DC}(\omega) \tag{5.4}$$

assuming the filters are linear, time-invariant components, the estimation can proceed by using a tapped delay line structure and forming a vector $\mathbf{x}(n) = [x(n) \quad x(n-1) \quad \ldots \quad x(n-m)]$, and formulating an estimate of the noise in the primary path

$$\hat{u}_{++}(n) = \mathbf{X}^T w \tag{5.5}$$

where w_{opt} will be given by

$$\mathbf{F}[w_{opt}] = \widehat{H}^{-1}_{SAW-DC}(\omega)\widehat{H}_{Ant-Rx-DC}(\omega) \tag{5.6}$$

The optimum value of the filter is obtained by allowing the system to converge using RLS recursion of the form,

$$P_i = \lambda^{-1}[P_{i-1} - \frac{\lambda^{-1}P_{i-1}\mathbf{X}^*_i\mathbf{X}_iP_{i-1}}{1+\lambda^{-1}\mathbf{X}_iP_{i-1}\mathbf{X}^*_i}] \tag{5.7}$$

where λ is the forgetting factor (0-1) and a weight update is given by

$$w_i = w_{i-1} + P_iX_i\,[d(n) - X_iw_{i-1}] \tag{5.8}$$

The mean square error coming out of the cancellation system is given by

$$e = J = EMSE + J_{\min} \tag{5.9}$$

where $J_{\min} = \sigma^2_{Rx} + \sigma^2_{n_p}$ is the power in the received signal and noise floor, and EMSE is the excess mean square error due to the stochastic gradient method used. Ideally the EMSE should be zero which would lead to nominal value of received signal SNR $\frac{\sigma^2_{Rx}}{\sigma^2_{n_P}}$.

The presence of excess mean square error deteriorates these values by the amount of extra gradient noise present. The value of EMSE for RLS algorithm is given by

$$EMSE_{RLS} \approx \frac{(\sigma^2_{Rx} + \sigma^2_{n_p})(1-\lambda)m}{2} \tag{5.10}$$

We see from (5.10) that the excess mean square error is a function of forgetting factor λ and the order *m* of the RLS filter. We can trade off filter convergence time with EMSE by increasing the forgetting factor. We define and report two metrics of performance for noise cancellation system which are based on accurate prediction of noise, and the final

recovered SNR of the received signal. The first referred to as NC_MSE is defined in terms of signals in Figure 5.2, and is given by

$$NC\_MSE_{dB} = -1 \times 10 \log_{10} \frac{E[(u_{++} - \hat{u}_{++})^2]}{E[(u_{++})^2]} \tag{5.11}$$

The second metric is that of received SNR post cancellation, which is dependent on the original strength of received signal and the residual of cancellation

$$RxSNR_{dB,PostIC} = 10 \log_{10} \frac{E[(Rx)^2]}{E[(u_{++} - \hat{u}_{++} + n_p + n_D)^2]} \tag{5.12}$$

5.4 Simulation studies on noise cancellation

In order to test the theoretical ideas and quantify the system performance we begin our investigation using a SIMULINK model. An AWGN noise signal is colored through an autoregressive moving average filter. The colored noise is passed through a duplexer filter and then subsequently through the first receiver. The results are shown in Figure 5.3 and 5.4. On the X axis of the figures is the level of this Rx Band noise in the primary branch, with respect to the thermal noise added into it i-e the ratio of u_{++}^2 to n_p^2 in dBs (referred to as RxBN/Nth). Figure 5.3 shows the cancellation performance that can be achieved with different filter orders. NC MSE is plotted against different values of the RxBN/Nth. The figure also contains a separate trace representing the minimum performance required to achieve the criteria of 0.5 dB RoT (Rise over Thermal). This criteria represents the fact that after cancellation, the residual Rx band noise, will contribute to the thermal noise floor so as to increase it only by 0.5 dB and no more. We see that this criterion is satisfied by all the filter orders investigated. Figure 5.4 shows the effect of cancellation on the final SNR of the received signal.

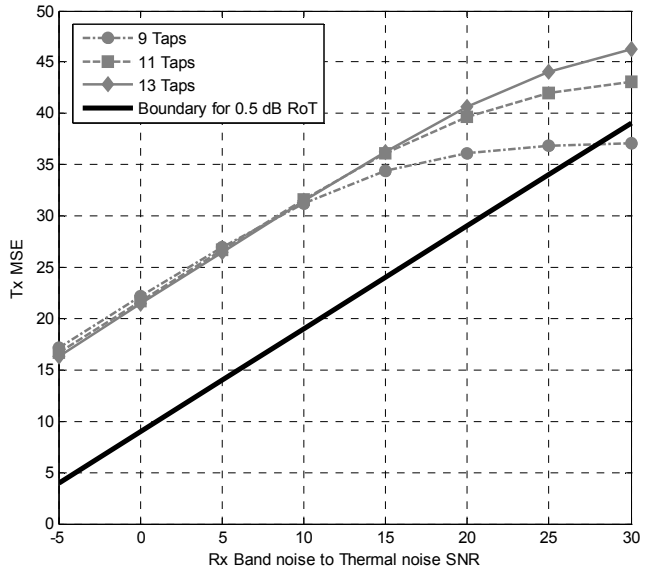

Figure 5.3. MSE for different filter orders

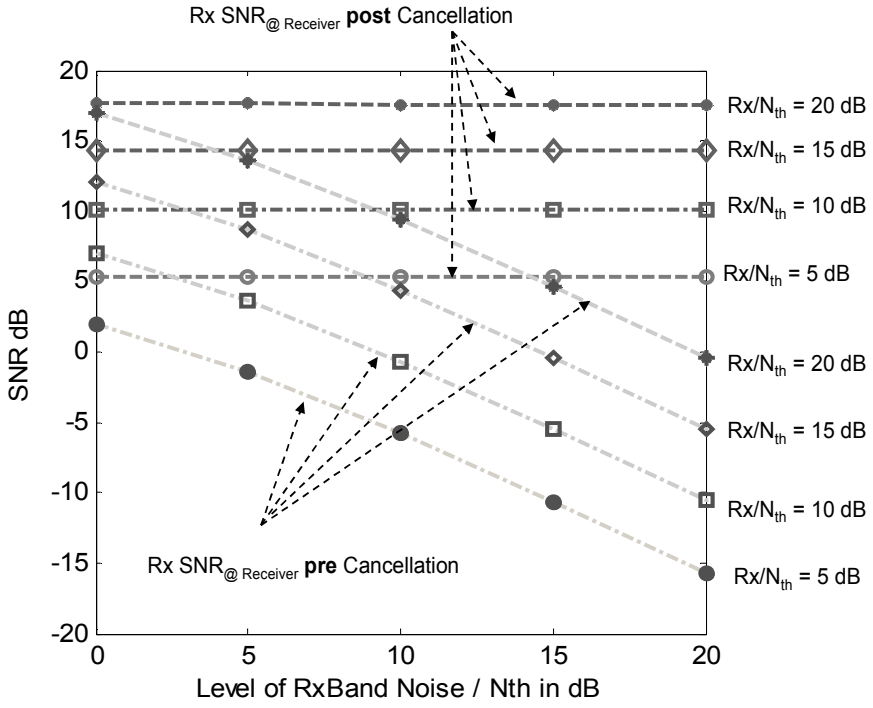

Figure 5.4. Simulation results for pre/post cancellation

The first set of four curves in Figure 5.4 represent different levels of injected *Rx* signal injected into the system. The figure shows that as RxBN/Nth ratio increases (light colored curves), the SNR of the received signal degrades which confirms the intuition. Another set of curves (dark color) represent the Rx SNR post cancellation It can be seen that the cancellation algorithm has been able to restore Rx signal to its nominal values w.r.t to the thermal noise. As much as a degradation of 20 dBs in SNR has been nullified by the adaptive cancellation algorithm. In order to observe how the performance of the algorithm deteriorates with the quality of auxiliary receiver, we plot the results of Figure 5.5.

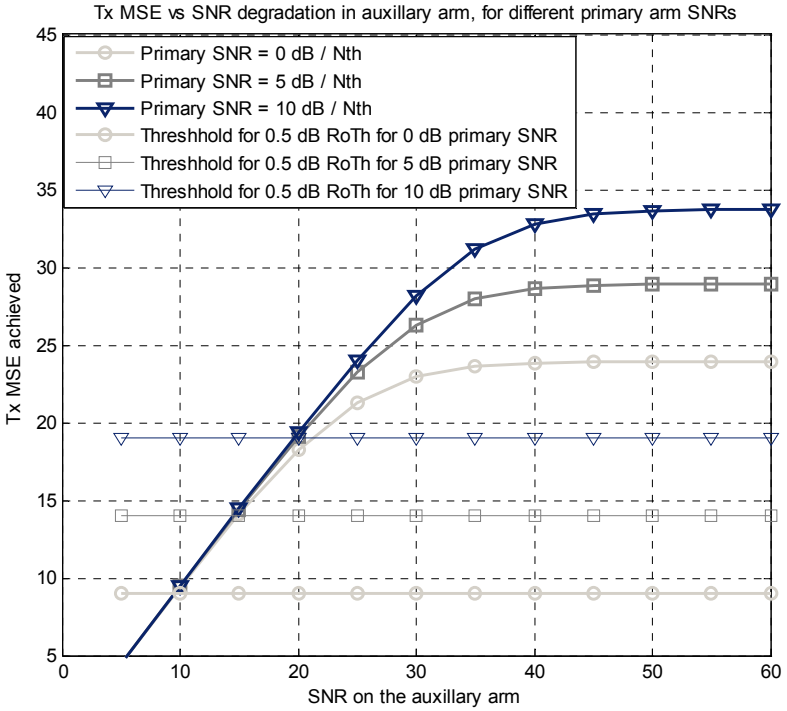

Figure 5.5. Auxiliary receiver performance requirement for noise cancellation

Figure shows that the auxiliary receiver has to have a certain minimum threshold to satisfy the requirement for 0.5 dB rise over thermal (RoT). From the Figure it can be

concluded that SNR on the auxiliary arm has to be 10 dB higher in order to do perfect noise cancellation.

5.5 RF measurement system for noise cancellation

In order to demonstrate the ideas mentioned in section 5.2, a test setup was built to see if the PA thermal noise can actually be cancelled in commercial RFIC chipsets. It is shown in Figure 5.6.

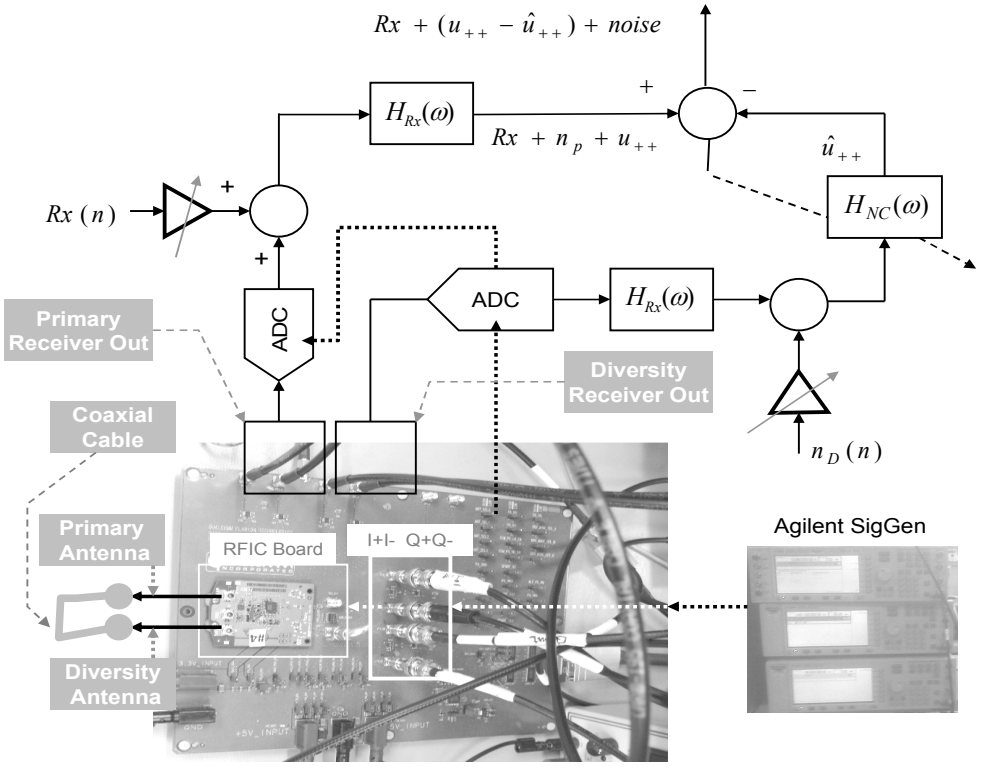

Figure 5.6. Measurement setup with a commercial RFIC

The setup exactly mimics the arrangement in Figure 5.2. A signal generator is used to inject a signal into the RFIC front-end. The antenna output of the transmitter is connected to the receiver input (antenna) of the diversity receiver to realize the arrangement in Figure 5.2. PA thermal noise leaking through relaxed duplexer attenuation finds its way into the primary receiver. The signal output from both the primary and secondary

receivers is taken out and sampled into the digital base-band where it is processed to see if adequate noise cancellation can be demonstrated.

Since this experiment uses commercial RFIC chipsets and boards, the duplexer attenuation was already sufficient to attenuate all the PA thermal noise down to the ambient thermal noise floor of the receiver. The observation of Rx Band noise is therefore not possible with commercial components and designated bands. The problem is depicted in Figure 5.7.

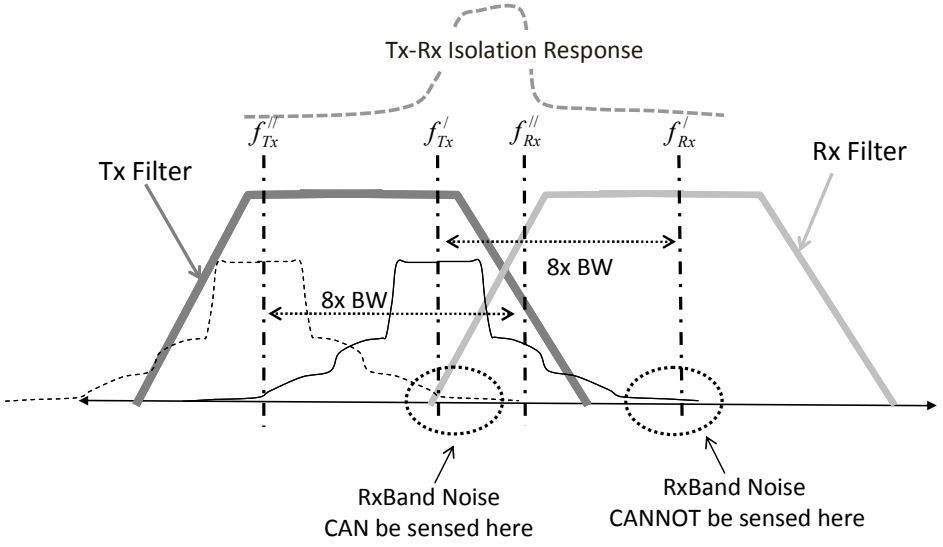

Figure 5.7 Method to capture Rx Band Noise (RxBN) with current generation of duplexers

The observation of noise at the receiver frequency of $f_{Rx}^{/}$ is not possible because of the duplexer attenuation. For this reason, the transmit frequency was moved from $f_{Tx}^{/}$ to $f_{Tx}^{//}$ so that the noise spectrum (lying at 8x bandwidth away) falls at the receiver frequency of $f_{Rx}^{//}$. This is an unconventional frequency for the receiver as it falls in the guard band of UMTS frequency allocation. Since the receiver frequency can be tuned to an arbitrary value, this flexibility of the PLL was exploited to move the receiver to the designated frequency. Figure 5.8, shows the results of experiments conducted on a CDMA based

EVDO signal having 2 MHz of bandwidth. The receiver is tuned to a frequency of 1916 MHz , roughly 8x bandwidth away from the transmission frequency of 1908.75. The output PA is configured to generate 23 dBm of output power.

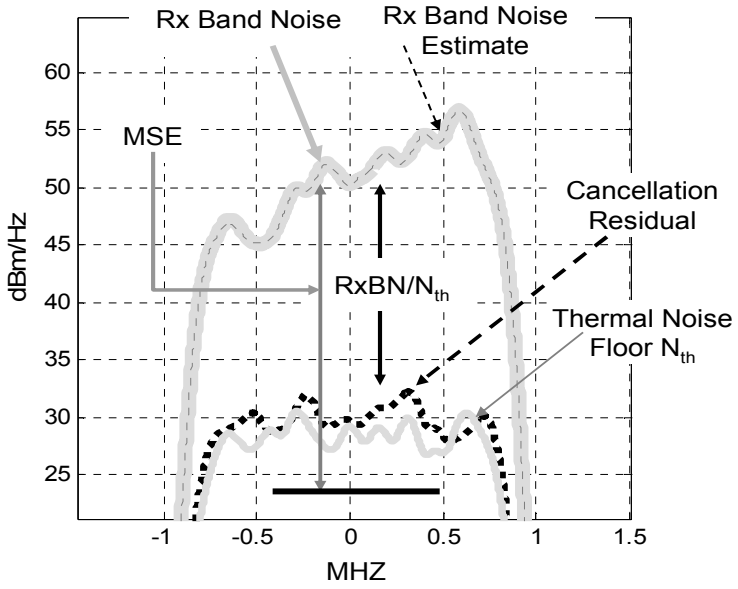

Figure 5.8 Lab Test bench results with a 2 MHz EVDO system

The thermal noise floor of the receiver was first measured with the power amplifier off. It is plotted as a trace in Figure 5.8 and is around 30 dBm/Hz on a relative scale. The noise floor was again measured with the PA on, and it has risen to around 50 dBm/Hz. Subsequently the cancellation system was put on, using a signal from auxiliary receiver. The signal captured in the auxiliary branch was about 10 dB higher in power than the primary RxBN signal shown in the Figure 5.8. The dotted black trace shows the residual after cancellation. It is apparent that the cancellation algorithm has reduced the PA generated noise below the noise floor (shown by MSE in Figure 5.8) such that the residual of cancellation is falling slightly above the noise floor.

The experiment was repeated by injecting Rx signal into the system at the antenna input. The Rx signal acts as a disturbance to the cancellation algorithm and hence deteriorates the cancellation performance of the system. We plot the two metrics of performance mentioned in Section 5.3 along with the level of Rx signal over Thermal Noise. The results are summarized in Table 5.1 for some practically relevant values of PA noise and Rx signal.

SCENARIO		PERFORMANCE		
RxBN / N_{th} (dB)	Rx/ N_{th} (dB)	NC_MSE (dB)	Rx SNR Pre IC (dB)	Rx_SNR Post IC (dB)
0.00	5.00	18.98	2.05	4.94
5.00	5.00	23.19	-1.21	4.91
0.00	10.00	14.90	7.00	9.86
20.00	10.00	28.48	-10.68	9.45
5.00	20.00	10.45	13.77	18.91
20.00	20.00	24.05	-0.24	18.55

Table 5.1 Received signal recovery performance after noise cancellation

By looking at the last column of Table 5.1, it is apparent that the severely deteriorated SINR pre cancellation has been restored close to the nominal values by the cancellation algorithm. Row 2, 4 and 6 demonstrate that SINRs have been restored from previously negative values. Rows 1,3 and 5 demonstrate how improvement in SNR can be accomplished for increased data rates.

5.6 Conclusion

The duplexer is a significant area/cost consuming component in the wireless transceivers. It also introduces post PA losses which reduce the effective radiated power. Research is underway to build tunable / multiband duplexers for receiver frontend. A fundamental problem with that is the reduced duplexer rejection of out-of-band emission results in higher levels of PA thermal noise falling in the receiver bandwidth. This can cause severe receiver signal deterioration by compromising the SNR. An adaptive cancellation architecture to mitigate the receive band noise problem has been proposed, by using an auxiliary receiver for PA noise sensing. The essential concept has been demonstrated by using the diversity receiver of a commercial RFIC. Measurements on RFIC using proposed scheme have shown good performance, restoring the desired Rx SNR close to its nominal value. Both simulation and measurement results have been reported and shown to be consistent.

Chapter 6

Coexistence with Highly Efficient Modern Transmitters

In building highly efficient transmitters of today, one is forced to sacrifice linearity for efficiency. Some of the highest PA efficiency figures are reported by envelope tracking amplifiers. These amplifiers can generate strong higher order harmonics which can lead to interference with receivers operating at the harmonic frequencies. Using nonlinear interference cancellation, we can help to remove the interference being caused in those receivers. This chapter looks at the problem of modeling the third harmonic emission from an envelope tracking amplifier. It derives the nonlinear kernel for estimating such interference. This kernel has been rigorously expanded to show its correlation with the third harmonic and its effectiveness in predicting the harmonic content. We then set up an envelope amplifier test-bench to capture the third harmonic and cancel it using the derived kernel model. The experiment yields excellent agreement with theory and provides a validation of the system and concept. By using this method of cancellation of the higher harmonic, we make the coexistence possible with highly nonlinear but efficient transmitters of today.

6.1 Higher frequency harmonics of ET transmitters

The transceivers of today are populated with different types of radios and the efficiency of transmitter is becoming increasingly important to conserve battery life. The highest efficiency demands highly nonlinear power amplifier architectures of which envelope tracking amplifiers have yielded best results [49]. An envelope tracking amplifier uses the information in the envelope to modulate the power supply voltage of

the PA and hence force the PA into its most efficient operating point. This modulation of the power supply can yield significant higher order harmonics. The situation is shown in Figure 6.1.

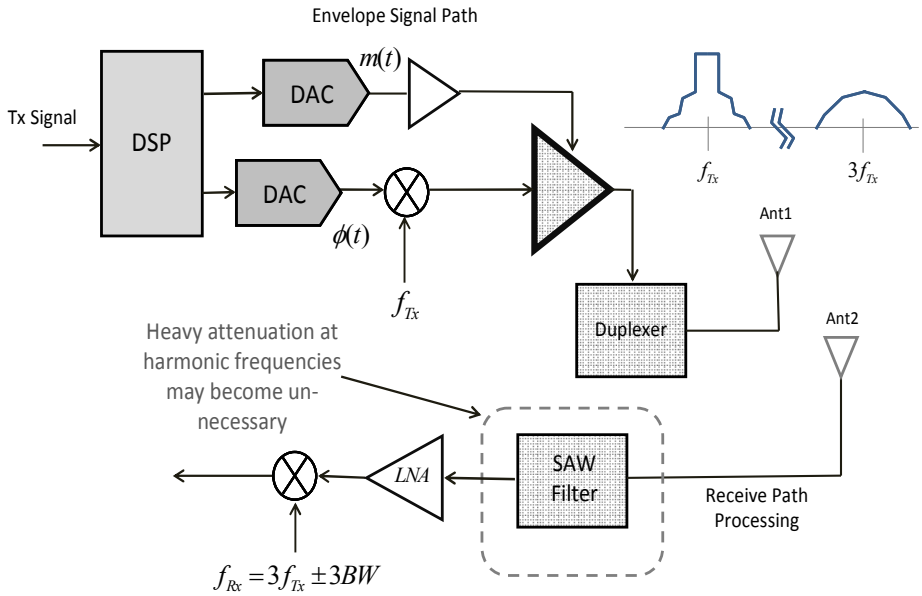

Figure 6.1. Impact of Envelope Tracking amplifier on collocated receiver

We see that the envelope tracking system produces an output signal centered at the transmit frequency f_{Tx}. The signal is suffering from spectral expansion due to nonlinearities which produce close in spectral regrowth as demonstrated by adjacent channel shoulders. However, the nonlinearities also produce harmonic distortion at far off frequencies like $3f_{Tx}$. With many radios operating in parallel on the same platform, a receiver within the same system may be operating at this far-off frequency. Figure 6.1 shows a receiver operating close to that frequency. As long as the tuning frequency of the receiver in within 3x the bandwidth of the original base-band signal, the receiver can possibly be impacted by the spectral emission at harmonics of f_{Tx}.

The close in spectral regrowth has been extensively studied in the literature [17] and nonlinear models for it have been developed. Interference cancellation techniques have also been proposed for this kind of spurious emission. The emission at harmonic frequencies has however not received attention. For the first time, to author's knowledge, we perform analytical derivations for the harmonic emission content, and then suggest nonlinear kernels that can model this emission. We derive and generalize these kernels and then setup an envelope tracking amplifier test-bench to test the theory on real RF system. The derivation of kernels is performed in Section 6.2 and the results of using these kernels with an experimental setup appear in Section 6.3.

6.2 Kernel model for third harmonic

We first discuss the derivation of kernels for accurate modeling of third harmonic. In order to do this, we need to first derive the effect of 3rd order nonlinearity on the modulated signal. We will then use that derivation to create a base-band equivalent model of the third harmonic.

$$TxPAIn = I(t)Cos(\omega t) - Q(t)Sin(\omega t) \tag{6.1}$$

If this signal was to encounter a third order nonlinearity we can write the expansion as follows

$$\begin{aligned}(TxPAIn)^3 = {} & I(t)^3 Cos^3(\omega t) - 3I(t)^2 Q(t) Cos^2(\omega t) Sin(\omega t) \\ & + 3I(t)Q(t)^2 Cos(\omega t) Sin^2(\omega t) - Q(t)^3 Sin^3(\omega t)\end{aligned} \tag{6.2}$$

calling the output as Tx^3, the expression can be simplified by using trigonometric identities. The simplified expression can be written in terms of harmonics of fundamental sines and cosines. This can allow the calculation of inphase and quadrature signals appearing at the harmonic frequencies. Such an expression is given by,

$$Tx^3 = \frac{1}{4}\begin{bmatrix} 3I(t)^3 Cos(\omega t) - 3I(t)Q(t)^2 Cos(\omega t) + I(t)^3 Cos(3\omega t) \\ +Q(t)^3 Sin(3\omega t) + 3I(t)Q(t)^2 Cos(3\omega t) - 3Q(t)^3 Sin(\omega t) \\ -3I(t)^2 Q(t) Sin(3\omega t) \end{bmatrix} \tag{6.3}$$

We can collect the terms representing the fundamental and the harmonics to re-write (3) as follows

$$\begin{aligned} H_3 &= \frac{3}{4}\left(I(t)^3 + I(t)Q(t)^2\right)Cos(\omega t) - \frac{3}{4}\left(I(t)^2 Q(t) + Q(t)^3\right)Sin(\omega t) \\ &+ \frac{1}{4}\left(I(t)^3 - 3I(t)Q(t)^2\right)Cos(3\omega t) - \frac{1}{4}\left(-3I(t)^2 Q(t) + Q(t)^3\right)Sin(3\omega t) \end{aligned} \tag{6.4}$$

If a filter is applied to select the fundamental frequency we get the form given in (6.5)

$$\begin{aligned} Tx^3{}_{@\omega} &= \frac{3}{4}I(t)\left(I(t)^2 + Q(t)^2\right)Cos(\omega t) \\ &- \frac{3}{4}Q(t)\left(I(t)^2 + Q(t)^2\right)Sin(\omega t) \end{aligned} \tag{6.5}$$

This is a well known form for representing IM3 close to Tx frequency. The equivalent complex baseband representation of a source signal given by (x=I+jQ)

$$H_{3-BB} = \left[|x|^2\, x\right] \longrightarrow \left\{\begin{matrix} x = I(t) - jQ(t) \\ |x|^2 = I(t)^2 + Q(t)^2 \end{matrix}\right\} \tag{6.6}$$

However if we apply a filter to collect the third harmonic (centered at 3ω), the terms we get are shown separately in (6.7)

$$\begin{aligned} Tx^3{}_{@3\omega} = H_3 &= \frac{1}{4}\left(I(t)^3 - 3I(t)Q(t)^2\right)Cos(3\omega t) \\ &- \frac{1}{4}\left(-3I(t)^2 Q(t) + Q(t)^3\right)Sin(3\omega t) \end{aligned} \tag{6.7}$$

We observe that coefficients of real and imaginary part no longer relate to the complex baseband model inferred in (6.6) for the fundamental signal component. Assuming a

complex baseband representation identical to that shown in (6.6), we formally define the complex baseband signal as,

$$x = I(t) - jQ(t) \tag{6.8}$$

we form a complex number after performing complex multiplications of the number with itself as shows in (6.9)

$$\widehat{H}_{3BB} = \left(I(t) - jQ(t)\right)^3 = x^3 \tag{6.9}$$

The power operation shown in (6.9) is accomplished by performing two complex multiplications. The result is given as a baseband estimate of the nonlinear products existing at the third harmonic.

$$\widehat{H}_{3BB} = I(t)\left(I(t)^2 - 3Q(t)^2\right) + j\ Q(t)\left(-3I(t)^2 - Q(t)^2\right) \tag{6.10}$$

The expression in 6.10 is significant. It tells us that real and imaginary parts of the product exactly correspond to the Cosine and Sine coefficients in (6.7). The distortion generated at the third harmonic can be modeled by the complex equivalent baseband model in (6.10)! Although we have found the model for the third harmonic caused by third order nonlinearity, we can generalize this model for higher order nonlinearities as well.

6.2.1 Third harmonic modeling with higher order nonlinearities

It is known from nonlinear systems theory that higher order nonlinearities will also create distortion at the location of third harmonic. In order to generalize the modeling of third order distortion, we need to include higher order nonlinearities. If the receiver is specifically tuned to the frequency of around $3f_{Tx}$, we need to find the order of nonlinearity that can generate spectral content at 3x the transmit frequency. Raising Tx

signal to the next available power of 4, and performing trigonometric simplification we obtain,

$$Tx^4 = \frac{1}{8}\begin{bmatrix} +\left(3I(t)^4 + 6I(t)^2Q(t)^2 + 3Q(t)^4\right) \\ +\left(-4I(t)^4 + 4Q(t)^4\right)Cos(2\omega t) \\ +\left(8I(t)^3Q(t) + 8I(t)\ Q(t)^3\right)Sin(2\omega t) \\ +\left(I(t)^4 - 6I(t)^2Q(t)^2 + Q(t)^4\right)Cos(4\omega t) \\ +\left(-4I(t)^3Q(t) + 4I(t)\ Q(t)^3\right)Sin(3\omega t) \end{bmatrix} \tag{6.11}$$

We observe that this leads to distortion products at the DC as well as 2x and 4x the transmit frequency. These distortion products are not relevant for the receiver tuned around $3f_{Tx}$ .When we raise the Tx signal to the next odd power of 5, we obtain distortion products at the third harmonic. This is shown in (6.12)

$$Tx^5 = \frac{1}{16}\begin{bmatrix} \left(10I(t)^5 + 20I(t)^3Q(t)^2 + 10I(t)Q(t)^4\right)Cos(\omega t) \\ +\left(-10I(t)^4Q(t) - 10I(t)^2Q(t)^3 + 5Q(t)^5\right)Sin(\omega t) \\ +\left(+5I(t)^5 - 10I(t)^3Q(t)^2 - 15I(t)Q(t)^4\right)Cos(3\omega t) \\ +\left(-15I(t)^4Q(t) - 10I(t)^2Q(t)^3 + 5Q(t)^5\right)Sin(3\omega t) \\ +\ \textbf{Higher Harmonic Terms} \end{bmatrix} \tag{6.12}$$

Paying careful attention to the 3rd harmonic terms, we try to reconstruct it using the baseband signal of (6.8). A first guess would yield a baseband estimator of the form

$$\hat{H}_{3BB}(5^{th}) = \left(I(t) - jQ(t)\right)^5 \tag{6.13}$$

Interestingly, the estimator of (6.13) does not yield the correct coefficients. Expanding (6.13) yields,

$$\begin{aligned} \hat{H}_{3BB}(5^{th}) = &\left(I(t)^5 - 10I(t)^3Q(t)^2 + 5I(t)Q(t)^4\right) \\ &+ j\left(5I(t)^4Q(t) - 10I(t)^2Q(t)^3 + Q(t)^5\right) \end{aligned} \tag{6.14}$$

Comparing the cosine and sine coefficients of third harmonic in (6.12) with the real and imaginary parts of (6.14) respectively will tell us that (6.13) is not the correct nonlinear

model for estimating the third order coefficients. The correct baseband model turns out to be

$$\widehat{H}_{3BB}(5^{th}) = \left(I(t) - jQ(t)\right)^3 \left|\left(I(t) - jQ(t)\right)\right|^2 \tag{6.15}$$

which when expanded leads to the real and imaginary parts as shown in (6.16)

$$\begin{aligned}\widehat{H}_{3BB}(5^{th}) &= \left(I(t)^5 - 2I(t)^3Q(t)^2 - 3I(t)Q(t)^4\right) \\ &+ j\left(-3I(t)^4Q(t) - 2I(t)^2Q(t)^3 + Q(t)^5\right)\end{aligned} \tag{6.16}$$

which exactly match the cosine and sine terms of the third harmonic in (6.12) (within a scale factor). Similarly we calculated the contribution to third harmonic by the impact of 7^{th} order nonlinearity and found that the coefficients can be given by

$$\widehat{H}_{3BB}(7^{th}) = \left(I(t) - jQ(t)\right)^3 \left|\left(I(t) - jQ(t)\right)\right|^4 \tag{6.17}$$

This leads us to postulate for the first time in the nonlinear literature, that the third harmonic located at $3f_{Tx}$ can be modeled using nonlinear kernels of the form,

$$\widehat{H}_{3BB}(n) = \left(I(t) - jQ(t)\right)^3 \left|\left(I(t) - jQ(t)\right)\right|^{(n-3)} \quad n = 3,5,7,..... \tag{6.18}$$

using the expression in (6.18) one can model and predict the harmonic content at the third harmonic frequencies. The model can be further used to cancel this interference causing harmonic.

6.3 Model and spectra for odd order harmonics

Using nonlinear polynomial expansions, we are able to derive the model for the third harmonic. During the derivation, it was noticed that certain symmetry of complex baseband representation can lead to the correct nonlinear expansions for harmonics. By using this symmetry of notation, we can further postulate that any odd order harmonic can be modeled using nonlinear kernels of the form

$$\hat{H}_{kBB}(n) = \left(I(t) - jQ(t)\right)^k \left|\left(I(t) - jQ(t)\right)\right|^{(n-k)} \quad n = k+3, k+5, k+7, \ldots\ldots \qquad (6.19)$$

Generally, the harmonic content has decreased in power to zero by the sixth or ninth harmonic, so that (6.19) may not be very useful in practice. More often than not, the third harmonic is the troublesome interference in many radio systems of today.

The expansion properties and the relationship of harmonics to expansion can also be observed graphically. In order to show this, two complex tones at 100 and 200 hertz were generated, and passed through a third order nonlinearity. A Fourier transform of the output shows the spectral components involved. The results are shown in Figure 6.2.

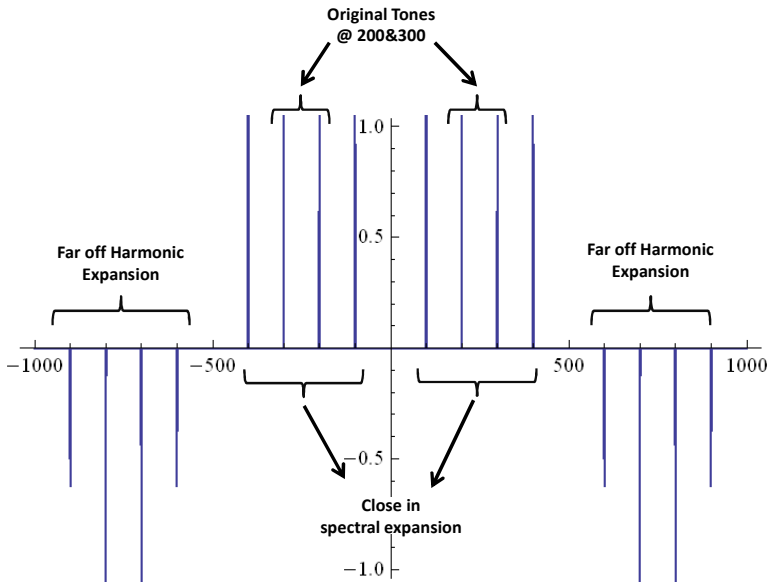

Figure 6.2. Illustration of third harmonic emission using two tones

We observe that the two tones of 200 & 300 Hz lead to close in spectral components ranging from 100-400 Hz. This represents a 3x extension in original tone spacing. The nonlinearity also leads to a spectral component at the harmonic frequencies. These components shown as 'Far off Harmonic Expansion' in Figure 6.2, and extend from 600Hz to 900 Hz. This also represents a 3x extension in the original tone spacing

(reflecting Bandwidth). We should therefore observe a similar bandwidth profile for a modulated multi-carrier signal. The third harmonic content should occupy a wider bandwidth, and frequency components would slowly taper in magnitude towards the edges.

We can now use equation (6.18) to predict the signal present at the 3rd harmonic frequency due to nonlinearities of several orders. We use (6.18) and substitute different values of n to create different kernels. These kernels are then linearly combined to model the frequency content at the third harmonic. The details of adaptive nonlinear tuning of the weights to cancel the emission are provided in Chapter 4 of this thesis.

6.4 Test-Bench and harmonic measurements

In order to validate the derivation of the kernel we setup an experimental test-bench with the envelope tracking power amplifiers. The objective was to compress the amplifier and extract the harmonic component being generated by the amplifier system. We can then use the transmitter signal available to us, to generate an estimate of the harmonic using derived kernels. If the estimate is subtracted from the extracted harmonic, we should be able to significantly cancel the harmonic content. The cancellation will depend on the accuracy of modeling. Higher order estimators will make the accuracy go better, and cancellation residual smaller.

The bench is shown in Figure 6.3. The Tx signal used is an LTE waveform with a total bandwidth of 5 MHz. This waveform is used to generate the low frequency drain modulating signal and the RF signal going into the power amplifier shown towards the left. The output of the power amplifier is taken to a harmonic capture board, which

captures down-converts and digitizes the third harmonic called h_3 coming out of the system.

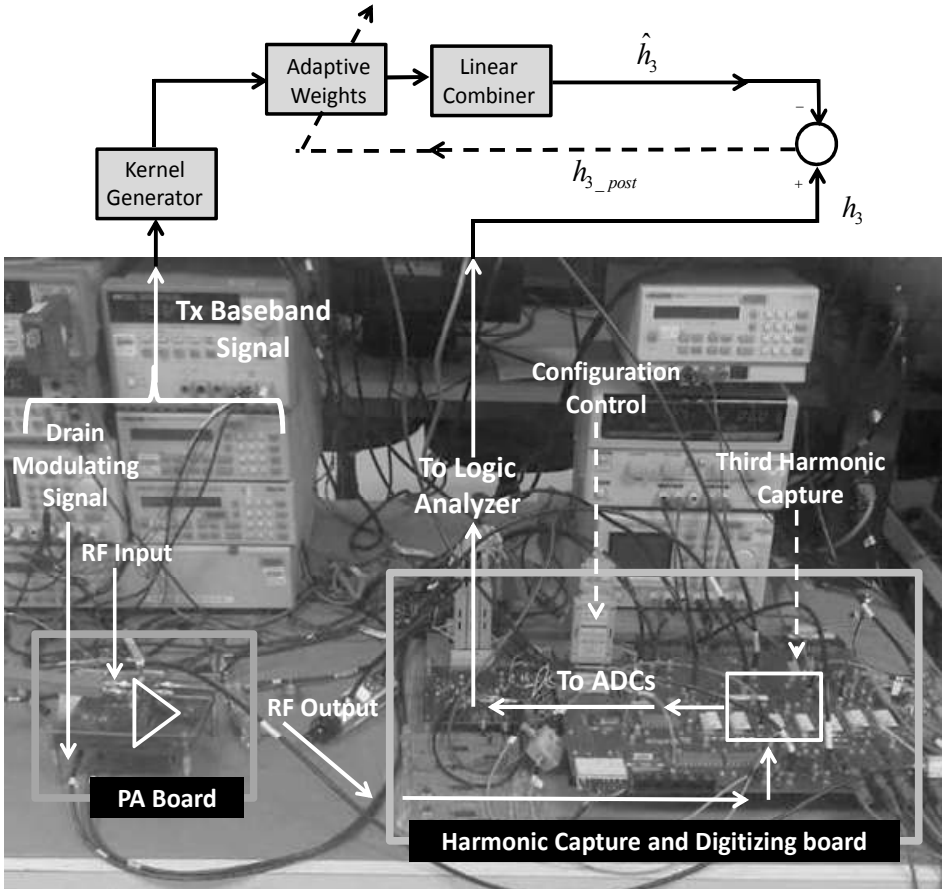

Figure 6.3. Test setup for validating cancellation performance

The top part of Figure 6.3 shows the modeling and subsequent cancellation of the 3rd harmonic. The baseband signal is over-sampled and passed through the kernel model derived in (6.18). A linear combination of these kernels (with unknown weights) is formed to create an estimate of the 3rd harmonic called $\hat{h}_3$ in Figure 6.2. The estimate is subtracted from the actual harmonic to form h_{3_post} which is the residual left after cancellation. The cancellation performance can be measured using MSE defined as a positive number as follows

$$Tx\_MSE_{dB} = -1 \times 10 \log_{10} \frac{E[(h_3 - \hat{h}_3)^2]}{E[(h_3)^2]} \tag{6.20}$$

The cancellation output h_{3_post} is also used to adapt the weights of the linear combination of kernels. This adaptive arrangement can learn the exact system model on the fly.

The result of running the experiment using the kernel complexity of the order 2 is shown in Figure 6.4.

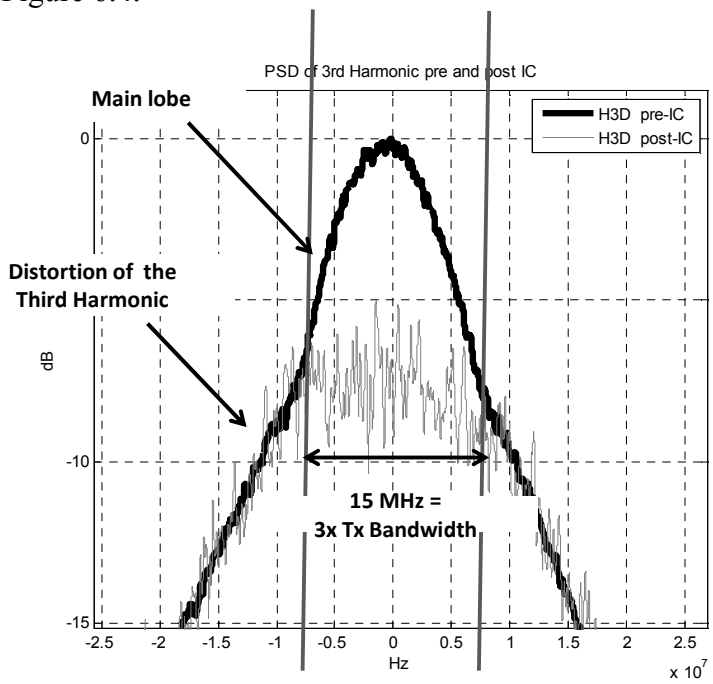

Figure 6.4. Cancellation of Third harmonic using two nonlinear kernels

The figure shows the originally captured 3rd harmonic as trace 1. We observe that the bandwidth of the main lobe is ~ 15 MHz, which alludes to the 3x bandwidth expansion to be undergone by the 3rd harmonic. Trace 2 of the figure shows the signal spectrum after cancellation. We observe that the residual interference is nearly 5 dB down from its peak values. We can observe that the cancellation of the signal is not perfect. In fact the reason can be observed clearly by looking at the time domain of the pre and post cancellation signals. Such a comparison is shown in Figure 6.5.

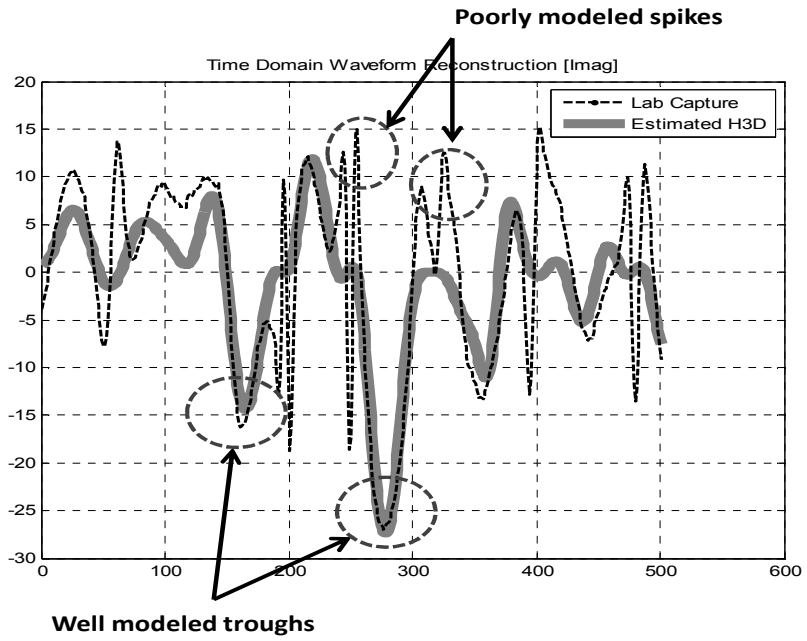

Figure 6.5. Time domain comparison of third harmonic waveforms for 2nd order kernels

Figure shows that certain troughs in the time domain waveform are very well modeled by the kernel function, and hence leads to the cancellation performance we observe in the PSD plot. At the same time, some high frequency peaks of the signal remain completely un-modeled by the kernel estimator. It is these peaks that prevent the residual distortion from going further down. This time domain picture also clearly tells us what needs to be done in order to improve the cancellation performance of the system. Increase the high frequency modeling by improving the kernel orders. Or in other words improve the modeling using models for higher order nonlinear distortion. We begin to add the nonlinear models for 7^{th}, 9^{th} and 11^{th} order distortions. The spectral and time domain results for doing that are shown in Figure 6.6, and 6.7. Figure 6.6 shows the spectral plot of pre and post cancellation signal, using three different kernel orders of 2,3 and 8.

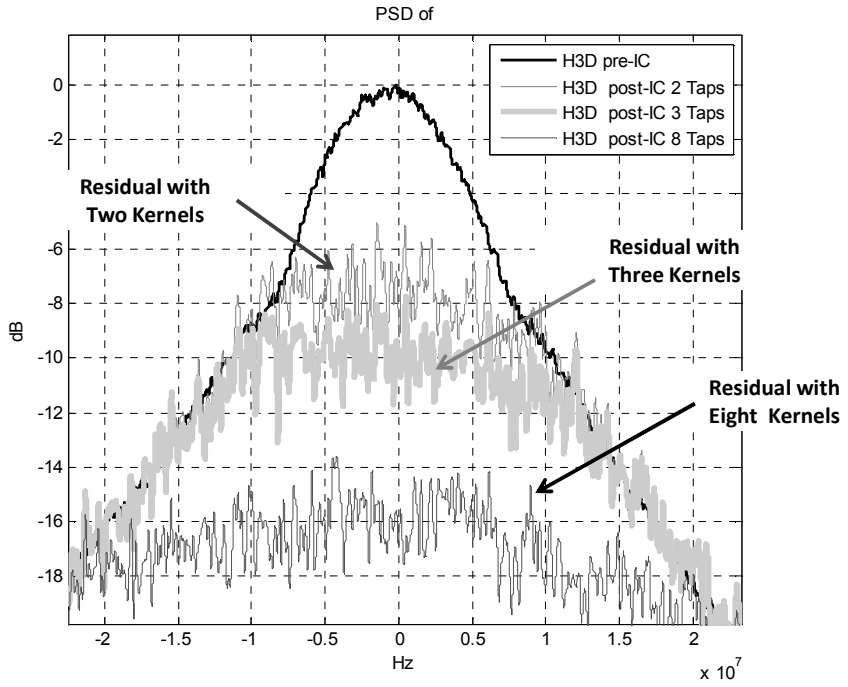

Figure 6.6. Pre and post cancellation spectra using three different nonlinear orders

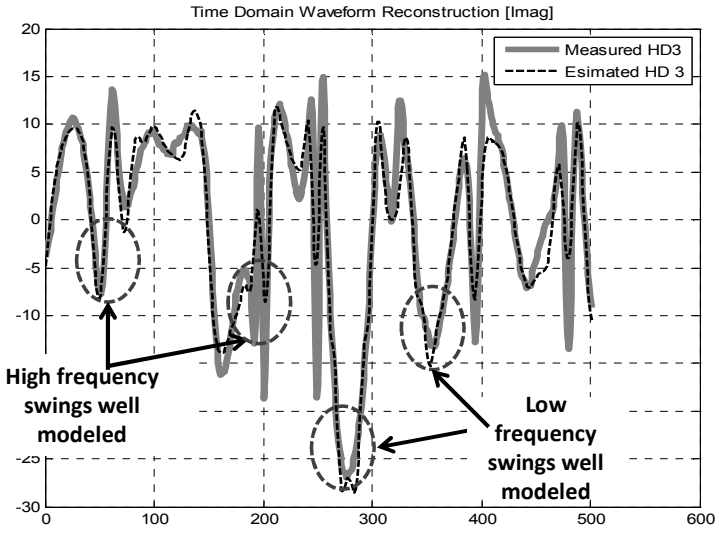

Figure 6.7. Time domain reconstruction using 8th order nonlinear kernels

Figure 6.6 shows the residual with successive increasing kernels orders. The kernel order of two uses two third order kernels from expression 6.18. We see that it is able to reduce the emission down by 5 dB and almost gets rid of the main 15 MHz lobe of the harmonic

distortion. Using three kernels can reduce emission further by ~1.5-2 dB. The last trace shows the result of using 8 nonlinear terms. We observe that nearly 15 dB of emission reduction has been achieved with the use of higher nonlinear terms. Figure 6.7 shows the time domain reconstruction of third harmonic distortion. We observe that previously un-modeled / ill-modeled high frequency swings have now been reconstructed using the 8 nonlinear terms.

6.5 Conclusion

In this chapter we looked at the problem of emission by highly efficient nonlinear transmitters. These transmitters can lead to strong adjacent channel spurious components as well as significant higher harmonic content. We tackled the problem of spurious transmitter emission at higher harmonic frequencies by developing nonlinear models for that emission. The nonlinear models for predicting this kind of interference are non-existent in the literature. We provide a derivation of the kernel for such an emission, and then use the derived kernels to predict actual interference coming from a lab setup. The theoretical model is well able to predict actual interference and provide a very good cancellation performance to validate the theory with lab measurements. If one can model and cancel such emission, co-existent with such highly nonlinear transmitters becomes a real possibility.

Chapter 7

Conclusions, Contributions and future work

Building radio frequency circuits is an art and science that began with the work of James Clerk Maxwell. Towards the close of nineteenth century, in a stroke of historic genius, Maxwell discovered the phenomena of wave propagation. The first half of the 20th century was an age of radio development. But even towards the middle of 20th century, radio was considered a black art. Practitioners learnt the discipline through years of lab training, apprenticeships, and the tricks of the trade were passed from the master to his students. For many decades this remained the situation. With the proliferation of cellular phones, in the eighties and nineties, the science of RF design became wide spread. 21st century heralded the age of modern RFICs and tremendous development in radio architectures. For a while radio design has looked easy! But with the tremendous increase in data rates over air interfaces and a plethora of different RF transmission standards hitting the air, the radio design is becoming blacker and murkier by the day. The culprit is Interference.

7.1 Summary of work

This thesis has sought to provide another look at RF interference at the fundamental level. While previous interference control and regulation methods have existed in the literature, they were more focused on preventing the interference from happening. On the contrary, we have taken a different approach of correcting the interference once it has happened. This allows the transmitters to be more nonlinear, passive filter design to be eased, and receivers to be aware of interference problems.

Under this unifying theme of building intelligent radios where receivers are more cognizant of the transmission environment, we have presented a number of architectures. The entire spectrum of these architectures has been proposed for the very first time in the literature. We begin by providing an instance of a particular RF interference problem. A candidate architecture is then proposed to attack the interference problem, and extensive system simulations are designed to validate the theory and principle of action. Every interference scenario is practically illustrated by setting up an RF test bench to emulate the interference problem. We correlate theory and measurements to illustrate the efficacy of these new architectures, and in certain instances, suggest improvements to be made to gain additional performance.

The first chapter to discuss this interference cancellation was Chapter 3, which described the problem of a transmitter jamming its own receiver by way of spurious spectral emissions due to nonlinearities. The spurious emission in the adjacent spectral regions can degrade the SNR of a receiver operating in the FDM (Frequency Division Multiplexing) mode. In Chapter 3 we attack this problem of spurious emission into the receive band by modeling the nonlinear radio front-end, coming up with an estimate of interference at the receiver, and cancelling the disturbing interference at the receiver leading to a boost in the SNR. In Chapter 4 we similarly model the frontend of RFIC in the case of operation under spurious receivers. Here too, we are able to cancel the effect of spurious receivers, by using accurate modeling and adaptive cancellation of front-end's interference. Chapter 5 addresses the excess noise problem that falls into the receive band, by sensing and cancelling the noise in a noise cancellation setup. Finally Chapter 6 demonstrates how the cancellation of spurious emission generated by highly

efficient transmitters is also possible, using a new form of volterra kernels. Harmonic emission located at higher harmonics can be cancelled using these new types of volterra kernels. We were thus able to demonstrate that using adaptive digital techniques and nonlinear systems theory we can come up with effective compensation schemes for nonlinear transmitters. These techniques allow us to cancel the transmitter interference and hence realize co-existence in various shapes and forms.

7.2 Contributions of the thesis

The following are the contributions, author has made to the area of RF systems, nonlinear compensation, and interference mitigation.

1. Proposed an alternative philosophy of managing interference by two pronged strategy of containing the emission at transmitter and cancelling at the receiver
2. Designed a new architecture for modeling the scenario of nonlinear transmitter emissions affecting the receiver. Developed a mathematical model for incorporating the transmitter and receiver front-end into a single model that can be adaptively tuned for optimal cancellation performance.
3. Simulated and lab tested an alternative to predistortion, by securing the receiver against out-of-band emission caused by the transmitter.
4. Developed a method of compensating for the interference effect caused by spurious receivers by developing a baseband model for joint transmitter-spurious-receiver frontend.
5. Designed, developed, and prototyped a system for demonstrating that compensation of spurious receivers is possible in real RFICs.

6. Proposed and simulated a method of compensating for the noise created by PA operation in the transmitter
7. Demonstrated that thermal noise interfering with receiver operation can be cancelled in an actual RFIC using proposed cancellation technique
8. Proposed a method for combating the harmonic emission caused by highly efficient nonlinear transmitters, by using new forms of volterra kernels
9. Derived nonlinear kernels for modeling harmonic emission and proved that they can accurately represent harmonic emission.
10. Prototyped an RF measurement system to extract the harmonic emission from an envelope tracking amplifier, and use the new volterra kernels to model and cancel the emission, showing the validity of mathematical derivation.

7.3 Future work

7.3.1 Interference cancellation for heterogeneous Tx/Rx

The different co-existence scenarios presented in the thesis are only the beginning of work in this area. Chapter 3 has presented a situation in which a transmitter is jamming its own receiver through nonlinear emission. A related scenario would be a transmitter of a different standard jamming a receiver. An LTE radio for example could be jamming a Bluetooth radio, or vice versa. It must be kept in mind that even if such an interference scenario does not exist in our contemporary reasoning, it can very easily be generated by the peculiar nonlinearities caused by ever shrinking newer active devices. The theory presented in this thesis can be used to take the interference causes by different radio standards into each other. There are however challenges involved in such systems which are rooted in their different power levels of operation (receiver AGC design), different

bandwidths, and the availability of synching capability between these different radio data streams. Theoretically, the ideas of interference cancellation can be applied to such scenarios but their practical challenges would need to be overcome before such a system can be demonstrated.

7.3.2 Multi-Tx to Rx interference cancellation

Similar to the problem of a transmitter jamming its own receiver and a transmitter jamming a different receiver is an associated problem of two transmitters, mixing together through an inadvertent nonlinearity and jamming one of their own, or a different receiver. This problem is particularly challenging as two different transmitters are involved. The theory laid out in the thesis can be used to tackle this class of problems as well, but we have to deal with the intermodulation and kernel products of two different signals which are not in synchronous behavior with each other. The alignment of these transmitter waveforms and subsequent kernel generation would be a challenge that needs to be solved before such a system can be demonstrated.

7.3.3 Complex nonlinear RF front-ends

Several different challenges also relate to the effective modeling of radio front-ends. The fundamental idea put forth in the thesis is that co-existence between radios can be made possible if the nonlinear transmitter and receiver front-ends can be effectively modeled. The models used were however simplistic. The most important model put forth in Chapter 3 was a cascade of a nonlinear transmitter and a linear receiver. The model put forth in Chapter 4 was a cascade of a linear transmitter and a nonlinear receiver. These models were valid because of the particularly common interference scenarios

encountered in modern RFICs. However, these are not the only scenarios possible. There can be a situation where a nonlinear transmitter is generating spurious emission that passes through the linear system of duplexer and goes inside a nonlinearly operating compressed receiver. This situation would be akin to having a cascade of nonlinear, linear and nonlinear systems. The modeling of such a system can be hugely complex and difference simplifications and adjustments to theory maybe needed before we can come with effective models for such front-ends.

Similar to the problem of different nonlinear-linear cascades possible in RF front-ends is the associated problem of complexity. When nonlinear emissions pass through the stop band of the duplexer, our assumption has been that it encounters a relatively flat frequency response in the bandwidth of interest. This assumption allows us to determine the order of adaptive filter apriori and tune coefficients on the fly to get best performance. However, with the availability of relaxed / agile duplexers, this assumption will no longer be valid. We will not be able to use memory-less volterra polynomials for the modeling of RF front-end. Improved information theoretic models will be needed to determine the model order on the fly, and also adapt the model parameters. Some of the methods to accomplish this have been alluded to in Chapter 3 in the discussion on generalized interference cancellation. These ideas will need to be expanded and further explored to come up with effective strategies for model order determination and subsequent model order pruning. This can be a rich and fertile area of investigation.

Author's publications and patents

Published work

[1] **Omer, M**.; Rimini, R.; Heidmann, P.; Kenney, J.S.; , "A PA-noise cancellation technique for next generation highly integrated RF front-ends," *Radio Frequency Integrated Circuits Symposium (RFIC), 2012 IEEE* , vol., no., pp.471-474, 17-19 June 2012

[2] **Omer, M**.; Rimini, R.; Heidmann, P.; Kenney, J. S.; , "All digital compensation scheme for spur induced transmit self-jamming in multi-receiver RF frond-ends," *Microwave Symposium Digest (MTT), 2012 IEEE MTT-S International* , vol., no., pp.1-3, 17-22 June 2012

[3] **Omer, M**.; Rimini, R.; Heidmann, P.; Kenney, J. S.; , "A compensation scheme to allow full duplex operation in the presence of highly nonlinear microwave components for 4 G systems," *Microwave Symposium Digest (MTT), 2011 IEEE MTT-S International* , vol., no., pp.1-4, 5-10 June 2011

[4] **Omer, M**.; Sajadieh, M.; Kenney, J.S.; , "A Fast Converging Adaptive Pre-Distorter for Multi-Carrier Transmitters," *Communications, 2009. ICC '09. IEEE International Conference on* , vol., no., pp.1-6, 14-18 June 2009

[5] **M. Omer** ; Farasat Munir Masoud Sajadieh; J Stevenson Kenney. A Predistortion Architecture for Fast Polynomial Estimation in Multi-carrier Transmitters, *Communications, 2009. ICC '2010. IEEE International Conference.* Published but not archived on Xplore. Copy available from authors.

[6] **M. Omer** ; J Stevenson Kenney. "A Spectrum Clearing System for Radio Coexistence with High Power Jamming. " *IEEE Milcom 2011*.

[7] Waseem, M.; **Omer, M**.; "A Model-checking Approach for HDL Descriptions Using Data Dependency Analysis ," *Infotech @ Aerospace 2012 AIAA*, 19 June 2012 - 21

[8] Munir, F.; **Omer, M**.; Masood, M.; Kenney, J.S.; , "Joint circuit and system evaluation of nonlinear compensation in RF/Microwave front-ends," *Wireless and Microwave Technology Conference (WAMICON), 2011 IEEE 12th Annual* , vol., no., pp.1-4, 18-19 April 2011

[9] Mukherjee, T.S.; **Omer, M**.; Jihwan Kim; Kornegay, K.T.; , "Design and optimization of a 71 Gb/s injection-locked CDR," *Circuits and Systems, 2009. ISCAS 2009. IEEE International Symposium on* , vol., no., pp.177-180, 24-27 May 2009

[10] Masood, M.; Gray, B.; Melville, R.; **Omer, M**.; Chen, J.H.; Kenney, J.S.; , "Modeling and linearization of a parametric power upconverting amplifier," *Microwave Conference (EuMC), 2010 European* , vol., no., pp.1026-1029, 28-30 Sept. 2010

Manuscripts submitted / under review

1. Interference cancellation for odd harmonics of envelope tracking power amplifier systems ; Submitted to International Microwave Symposium 2013
2. A transceiver architecture to enable saw-less Tx/Rx co-existence in FDMA systems ; Submitted to IEEE Transactions on Microwave Theory and Techniques
3. Digitally assisted compensation for Tx interference in multi-receiver RFICs ; Submitted to IEEE Transactions on Microwave Theory and Techniques

Non provisional US Patents

Filed with the US patent office, IDF # 102389

Non Linear Digital Adaptive Scheme for Tx Out Of Band (OOB) Emission Cancellation.

Pub. No.:	WO/2012/075332	**International Application No.:**	PCT/US2011/062952
Publication Date:	07.06.2012	**International Filing Date:**	01.12.2011

Provisional US patents

1. Hybrid filter bank architecture for high efficiency envelope reconstruction in polar RF power amplifiers. Application serial # : 61/597,396
2. High Efficient Digital Doherty Transmitter for Handset Applications with Dual Lookup Table Digital Pre-distorter. Application serial # : 61/652,928
3. High Efficiency, High Dynamic Range PWM Modulation using Feed-Forward Spur Cancellation. Application serial # : 61/665,034
4. Adaptive Tuning of Hybrid Filter Banks for Efficient Operation of Envelope Modulator in Polar Transmitters. Application serial # : 61/667,694

References

[1] Chia, S.; Gill, T.; Ibbetson, L.; Lister, D.; Pollard, A.; Irmer, R.; Almodovar, D.; Holmes, N.; Pike, S.; , "3G evolution," *Microwave Magazine, IEEE* , vol.9, no.4, pp.52-63, Aug. 2008

[2] Adiseno; Ismail, M.; Olsson, H.; , "A wide-band RF front-end for multiband multistandard high-linearity low-IF wireless receivers," *Solid-State Circuits, IEEE Journal of* , vol.37, no.9, pp. 1162- 1168, Sep 2002

[3] B. Razavi, RF Microelectronics. Englewood Cliffs, NJ: Prentice-Hall, 1998

[4] De Luis, J.R.; Morris, A.S.; Qizheng Gu; De Flaviis, F.; , "A tunable asymmetric notch filter using RFMEMS," *Microwave Symposium Digest (MTT), 2010 IEEE MTT-S International* , vol., no., pp.1146-1149, 23-28 May 2010

[5] LTE & 3G evolution http://www.freescale.com/files/wireless_comm/doc/white_paper/3GPPEVOLUTIONWP.pdf

[6] Lelandais-Perrault, C.; Petrescu, T.; Poulton, D.; Duhamel, P.; Oksman, J.; , "Wideband, Bandpass, and Versatile Hybrid Filter Bank A/D Conversion for Software Radio," *Circuits and Systems I: Regular Papers, IEEE Transactions on* , vol.56, no.8, pp.1772-1782, Aug. 2009

[7] J. Mitola, “Software radios—survey, critical evaluation and future directions,” in Proc. Nat. Telesystems Conf.,May 1992, pp. 13/15–13/23

[8] A. Abidi, “The path to the software-defined radio receiver,” *IEEE J.Solid-State Circuits*, vol. 42, no. 5, pp. 954–966, May 2007

[9] Sevic, J.F.; Steer, M.B.; , "On the significance of envelope peak-to-average ratio for estimating the spectral regrowth of an RF/microwave power amplifier," *Microwave Theory and Techniques, IEEE Transactions on* , vol.48, no.6, pp.1068-1071, Jun 2000

[10] Zhou, Y.; Palanki, R.; Montojo, J.; Gaal, P.; , "Peak-to-average ratio reduction scheme for multi-carrier systems with block-based channel estimation," *Electronics Letters* , vol.45, no.5, pp.275-276, February 26 2009

[11] Harris, F.J.; Dick, C.; Rice, M.; , "Digital receivers and transmitters using polyphase filter banks for wireless communications," *Microwave Theory and Techniques, IEEE Transactions on* , vol.51, no.4, pp. 1395- 1412, Apr 2003

[12] C. Eder, G. Fischerauer, P. Hagn, and G. Riha, "SAW filters for 3G systems: a quantum leap in size and passive integration is ahead," in *Proc. IEEE Ultrasonics Symposium*, pp. 338–339, 2001

[13] M. Brandolini, P. Rossi, D. Manstretta, and F. Svelto, "Toward multi-standard mobile terminals:fully integrated receivers requirements and architectures," *IEEE Trans. Microwave Theory Tech.*, vol. 53, no. 3, pp. 1026–1038, Mar. 2005

[14] Ru, Z.; Moseley, N.A.; Klumperink, E.; Nauta, B.; , "Digitally Enhanced Software-Defined Radio Receiver Robust to Out-of-Band Interference," *Solid-State Circuits, IEEE Journal of* , vol.44, no.12, pp.3359-3375, Dec. 2009

[15] H. Kang, Y. Cho, and D. Youn, "On compensating nonlinear distortions of an OFDM system using an efficient adaptive predistorter," IEEE Trans.Commun., vol. 47, no. 4, pp. 522–526, Apr. 1999

[16] S. Cripps, Advanced Techniques in RF Power Amplifiers Design. Norwood, MA: Artech House, 2002

[17] Zhou, G.T.; Kenney, J.S.; , "Predicting spectral regrowth of nonlinear power amplifiers," *Communications, IEEE Transactions on* , vol.50, no.5, pp.718-722, May 2002

[18] Koeppl, H.; Singerl, P.; , "An Efficient Scheme for Nonlinear Modeling and Predistortion in Mixed-Signal Systems," *Circuits and Systems II: Express Briefs, IEEE Transactions on* , vol.53, no.12, pp.1368-1372, Dec. 2006

[19] Chuanzhao Yu; Yuan, J.S.; , "Electrical and Temperature Stress Effects on Class-AB Power Amplifier Performances," *Electron Devices, IEEE Transactions on* , vol.54, no.6, pp.1346-1350, June 2007

[20] P. B. Kenington, High-Linearity RF Amplifier Design. Norwood, MA: Artech House, 2000.

[21] Lavrador, P.M.; Cunha, T.R.; Cabral, P.M.; Pedro, J.C.; , "The Linearity-Efficiency Compromise," *Microwave Magazine, IEEE* , vol.11, no.5, pp.44-58, Aug. 2010

[22] J. C. Pedro and S. A. Maas, “A comparative overview of microwave and wireless power amplifier behavioral modelling approaches,” *IEEE Trans.Microw. Theory Tech.*, vol. 53, no. 4, pp. 1150–1163, Apr. 2005

[23] Ghorbani, A. and M. Sheikhan, "The Effect of Solid State Power Amplifiers (SSPAs) Nonlinearities on MPSK and M-QAM Signal Transmission," *Sixth Int'l Conference on Digital Processing of Signals in Comm.*, 1991, pp. 193-197

[24] Rapp, C., "Effects of HPA-Nonlinearity on a 4-DPSK/OFDM-Signal for a Digital Sound Broadcasting System," in *Proceedings of the Second European Conference on Satellite Communications*, Liege, Belgium, Oct. 22-24, 1991, pp. 179-184.

[25] Saleh, A.A.M., "Frequency-independent and frequency-dependent nonlinear models of TWT amplifiers," *IEEE Trans. Communications*, vol. COM-29, pp.1715-1720, November 1981

[26] Tao Jiang; Yiyan Wu; , "An Overview: Peak-to-Average Power Ratio Reduction Techniques for OFDM Signals," *Broadcasting, IEEE Transactions on* , vol.54, no.2, pp.257-268, June 2008

[27] Xiaoyun Wei; Guofu Niu; Ying Li; Ming-Ta Yang; Taylor, S.S.; , "Modeling and Characterization of Intermodulation Linearity on a 90-nm RF CMOS Technology," *Microwave Theory and Techniques, IEEE Transactions on* , vol.57, no.4, pp.965-971, April 2009

[28] Kang, D.; Kim, D.; Cho, Y.; Kim, J.; Park, B.; Zhao, C.; Kim, B.; , "1.6–2.1 GHz broadband Doherty power amplifiers for LTE handset applications," *Microwave Symposium Digest (MTT), 2011 IEEE MTT-S International* , vol., no., pp.1, 5-10 June 2011

[29] Ai Bo; Yang Zhi-xing; Pan Chang-yong; Zhang Tao-tao; Ge Jian-hua; , "Effects of PAPR reduction on HPA predistortion," *Consumer Electronics, IEEE Transactions on* , vol.51, no.4, pp. 1143- 1147, Nov. 2005.

[30] Hammi, O.; Carichner, S.; Vassilakis, B.; Ghannouchi, F.M.; , "Synergetic Crest Factor Reduction and Baseband Digital Predistortion for Adaptive 3G Doherty

Power Amplifier Linearizer Design," *Microwave Theory and Techniques, IEEE Transactions on* , vol.56, no.11, pp.2602-2608, Nov. 2008.

[31] Gard, K.G.; Larson, L.E.; Steer, M.B.; , "The impact of RF front-end characteristics on the spectral regrowth of communications signals," *Microwave Theory and Techniques, IEEE Transactions on* , vol.53, no.6, pp. 2179- 2186, June 2005.

[33] Farazian, M.; Asuri, B.; Larson, L.E.; , "A Dual-Band CMOS CDMA Transmitter Without External SAW Filtering," *Microwave Theory and Techniques, IEEE Transactions on* , vol.58, no.5, pp.1349-1358, May 2010.

[34] Jyh-Wen Sheen; , "LTCC-MLC duplexer for DCS-1800," *Microwave Theory and Techniques, IEEE Transactions on* , vol.47, no.9, pp.1883-1890, Sep 1999.

[35] O'Sullivan, T.; York, R.A.; Noren, B.; Asbeck, P.M.; , "Adaptive duplexer implemented using single-path and multipath feedforward techniques with BST phase shifters," *Microwave Theory and Techniques, IEEE Transactions on* , vol.53, no.1, pp. 106- 114, Jan. 2005.

[36] Mirzaei, A.; Darabi, H.; Murphy, D.; , "Architectural Evolution of Integrated M-Phase High-Q Bandpass Filters," *Circuits and Systems I: Regular Papers, IEEE Transactions on* , vol.59, no.1, pp.52-65, Jan. 2012.

[37] Darabi, H.; Mirzaei, A.; Mikhemar, M.; , "Highly Integrated and Tunable RF Front Ends for Reconfigurable Multiband Transceivers: A Tutorial," *Circuits and Systems I: Regular Papers, IEEE Transactions on* , vol.58, no.9, pp.2038-2050, Sept. 2011

[38] Mirzaei, A.; Darabi, H.; , "A Low-Power WCDMA Transmitter with an Integrated Notch Filter," *Solid-State Circuits Conference, 2008. ISSCC 2008. Digest of Technical Papers. IEEE International* , vol., no., pp.212-608, 3-7 Feb. 2008.

[39] Mirzaei, A.; Darabi, H.; Murphy, D.; , "A low-power process-scalable superheterodyne receiver with integrated high-Q filters," *Solid-State Circuits Conference Digest of Technical Papers (ISSCC), 2011 IEEE International* , vol., no., pp.60-62, 20-24 Feb. 2011.

[40] Aparin, V.; Ballantyne, G.J.; Persico, C.J.; Cicalini, A.; , "An integrated LMS adaptive filter of TX leakage for CDMA receiver front ends," *Solid-State Circuits, IEEE Journal of* , vol.41, no.5, pp. 1171- 1182, May 2006.

[41] Namsoo Kim; Larson, L.E.; Aparin, V.; , "A Highly Linear SAW-Less CMOS Receiver Using a Mixer With Embedded Tx Filtering for CDMA," Solid-State Circuits, IEEE Journal of , vol.44, no.8, pp.2126-2137, Aug. 2009.

[42] Aparin, V.; , "A new method of TX leakage cancelation in W/CDMA and GPS receivers," *Radio Frequency Integrated Circuits Symposium, 2008. RFIC 2008. IEEE* , vol., no., pp.87-90, June 17 2008-April 17 2008.

[43] Cassia, M.; Hadjichristos, A.; Hong Sun Kim; Jin-Su Ko; Jeongsik Yang; Sang-Oh Lee; Sahota, G.; , "A Low-Power CMOS SAW-Less Quad Band WCDMA/HSPA/HSPA+/1X/EGPRS Transmitter," Solid-State Circuits, IEEE Journal of , vol.44, no.7, pp.1897-1906, July 2009.

[44] Wang Riyan; Li Zhengping; Huang Jiwei; Fang Min; Zhang Weifeng; Zeng Longyue; , "A 1.2-V CMOS front-end for LTE direct conversion SAW-less

receiver," Radio-Frequency Integration Technology (RFIT), 2011 IEEE International Symposium on , vol., no., pp.85-88, Nov. 30 2011-Dec. 2 2011.

[45] Weifeng Liu; Pokharel, P.P.; Principe, J.C.; , "The Kernel Least-Mean-Square Algorithm," *Signal Processing, IEEE Transactions on* , vol.56, no.2, pp.543-554, Feb. 2008

[46] Temporiti, E.; Weltin-Wu, C.; Baldi, D.; Tonietto, R.; Svelto, F.; , "A 3 GHz Fractional All-Digital PLL With a 1.8 MHz Bandwidth Implementing Spur Reduction Techniques," *Solid-State Circuits, IEEE Journal of* , vol.44, no.3, pp.824-834, March 2009

[47] Che-Fu Liang; Hsin-Hua Chen; Shen-Iuan Liu; , "Spur-Suppression Techniques for Frequency Synthesizers," *Circuits and Systems II: Express Briefs, IEEE Transactions on* , vol.54, no.8, pp.653-657, Aug. 2007

[48] Giannini, V.; Ingels, M.; Sano, T.; Debaillie, B.; Borremans, J.; Craninckx, J.; , "A multiband LTE SAW-less modulator with −160dBc/Hz RX-band noise in 40nm LP CMOS," *Solid-State Circuits Conference Digest of Technical Papers (ISSCC),* 2011

[49] Kimball, D.F.; Jinho Jeong; Chin Hsia; Draxler, P.; Lanfranco, S.; Nagy, W.; Linthicum, K.; Larson, L.E.; Asbeck, P.M.; , "High-Efficiency Envelope-Tracking W-CDMA Base-Station Amplifier Using GaN HFETs," *Microwave Theory and Techniques, IEEE Transactions on* , vol.54, no.11, pp.3848-3856, Nov. 2006

VITA

Mohammad Omer earned his masters in EE from Georgia Tech in 2008. He was the awardee of Fulbright fellowship for the years 2006-2008. He worked for Intel research labs before starting his PhD with CST lab in 2009. For some time he worked with Qualcomm corporate research and development center, where his work won him Roberto Padovani's fellowship for the most outstanding intern work of the year 2010. Mr. Omer also taught/assisted different courses at Georgia Tech, which won him 'ECE GTA Excellence award' for the year 2011. He was a finalist for the most outstanding graduate student instructor of the institute (Georgia Tech) in 2012. His areas of interest include nonlinear RF front-ends, adaptive signal processing, and digitally assisted methods for RF circuits and systems.